Modelling of bake hardening sequences in novel interstitial free bake hardening steels for automotive applications.

Gater, Alexander John Piers

MODELLING OF BAKE HARDENING SEQUENCES IN NOVEL INTERSTITIAL FREE BAKE HARDENING STEELS FOR AUTOMOTIVE APPLICATIONS

Alexander John Piers Gater

Thesis Submitted for the degree of Doctor of Engineering

At the University of Wales Swansea

ABSTRACT

With increasingly stringent demands regarding vehicle weight and coating compositions, there is obvious merit in the modelling of strain aging processes for the development of novel Bake Hardening grades. Additionally, there is indication from literature sources that the development of novel titanium-vanadium stabilised bake hardening products may provide benefits over more traditional titanium-niobium Ultra Low Carbon strip steel grades.

An experimental programme is developed exploring the effects of combined titanium and vanadium additions, regarding room temperature aging and bake hardening phenomena in specifically designed experimental ultra low carbon strip steel grades with controlled composition. This experimental programme is linked to the development of a novel variation of the Kinetic Monte Carlo technique presented for the purposes of modelling the formation of Cottrell atmospheres.

It is found that in the experimental Ultra Low Carbon Strip steels studies vanadium additions have a retarding effect on the rates of strain aging, without sacrificing bake hardening response, and that this effect may be tied to the formation of fine nanoscale coherent vanadium carbide precipitates in the steel matrix during annealing. The Kinetic Monte Carlo model presented is shown to predict rates of aging with a high level of accuracy within the limits of the experimental programme, and to have run times relevant to the requirements of a desktop pool when run using a modern personal computer.

It is anticipated that the results produced in this thesis could lead to the development of novel titanium-vanadium ultra low carbon bake hardenable grades, thus offering complementary bake hardenable products with longer shelf life and lower annealing temperature regimes to the traditional titanium-niobium existing grades.

This work has not been accepted in substance for any degree and is not being currently submitted in candidature for any degree.

Signed:

Date: 30/11/09

This thesis is the result of my own investigations, except where otherwise stated. Where correction services have been used the extent and nature of the correction is clearly marked in a footnote. Other sources are acknowledged by footnotes giving explicit references. A bibliography is appended.

Signed:

Date: 30/11/09

I hereby give consent for my thesis, if accepted, to be available for photocopying and for inter library loan, and for the title and summary to be made available to outside organisations.

Signed:

Date: 30/11/09

Acknowledgements

I wish to take this opportunity to thank Doctor George Fourlaris, Professor Steve Brown, and Doctor Laura Baker for their support and encouragement during my last four years of study. I would also like to extend my gratitude to the Engineering and Physical Sciences Research Council and Corus Strip Products UK without whose sponsorship none of this work would have been possible.

Many thanks to all members of the Physical Metallurgy and Phase Transformations research group at Swansea University, and those employees of Corus with whom I have had frequent contact over the last four years, for providing a warm working environment and being supportive of my research, and the research of my colleagues within the department.

Finally I would like to thank my beloved wife for supporting me throughout all of my endeavours.

Table Of Contents

Table Of Figures

CHAPTER ONE

INTRODUCTION

1. INTRODUCTION

Legislation passed within the EU requires a reduction of emissions and an improvement in fuel efficiency from future motor vehicles, along with an increased potential for recycling – simultaneously a desire among consumers for improved passenger safety and comfort, and larger, more powerful engines, is driving up average vehicle weights [1]. This is causing large changes in the face of automobile manufacture; vehicle manufacturers are looking for new materials that can give higher strengths and improved impact properties, at lower weights, and without sacrificing formability.

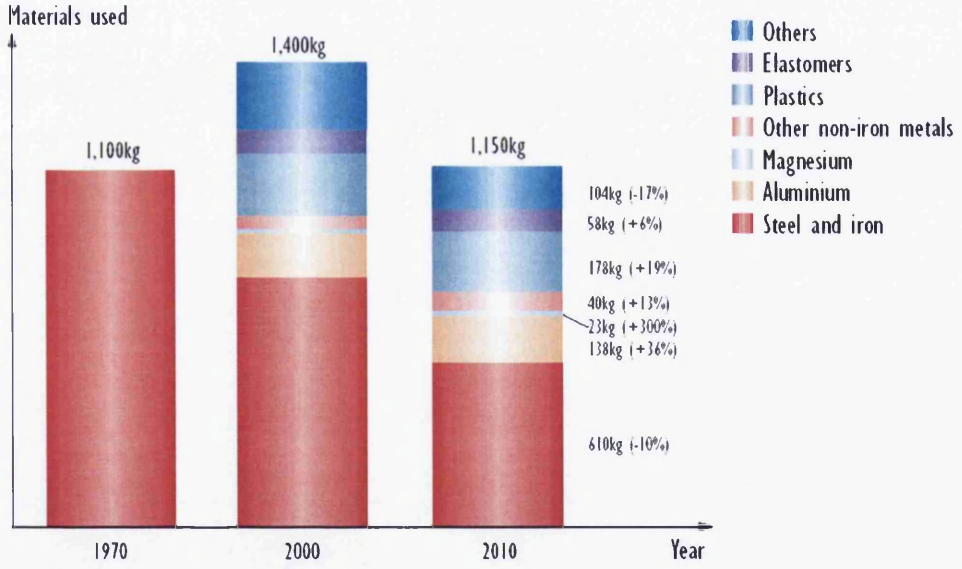

Figure 1.1 The Historical Development of materials used in the construction of a mid-sized car [2]

Some of these materials are non-ferrous, with vehicle components being made from aluminium and magnesium alloys (figure 1.1) [1-4] with ongoing research into the use of reinforced composites for body panels (a technology already used in some high performance race cars, but uncommon in commercial vehicle manufacture [2, 5, 6]). While the large scale usage of aluminium alloys and composites is so far reserved largely for high end or niche vehicles, the technology is well advanced; the body of the Jaguar XJ is comprised entirely of aluminium, the Audi A8 and Audi A2 are both built using panels of aluminium-alloy over an aluminium-alloy space frame, providing weight savings of around 150kg compared to other vehicles in its class, and the new 5 series BMW uses an aluminium front section and suspension.

To combat competition, the steels industry has responded with programmes to develop and promote the use of High Strength Steels (HSS) (210MPa < Yield Stress (YS) < 550MPa), Ultra High Strength Steels (UHHS) (550MPa < YS) and advanced high strength steels such as Dual Phase, TRIP and complex phase grades in the automotive sector. Two notable projects are the Ultra Light Steel Auto Body program (ULSAB) in which British Steel played a part, and the more recent Advanced Vehicle Concept program (ULSAB-AVC), completed in 2001, in which Corus Plc. played an active roll.

The ULSAB-AVC [7] vehicle offered weight savings of around 25% over a traditional vehicle in its class, and was comprised entirely of high strength steels, with 80% being composed of advanced high strength varieties. While the majority of this usage was in varieties of dual phase grades, 10% of the body was still comprised of Bake

Hardenable (BH) steel, much of this being in the door skins and body outer panels (Figure 1.2)

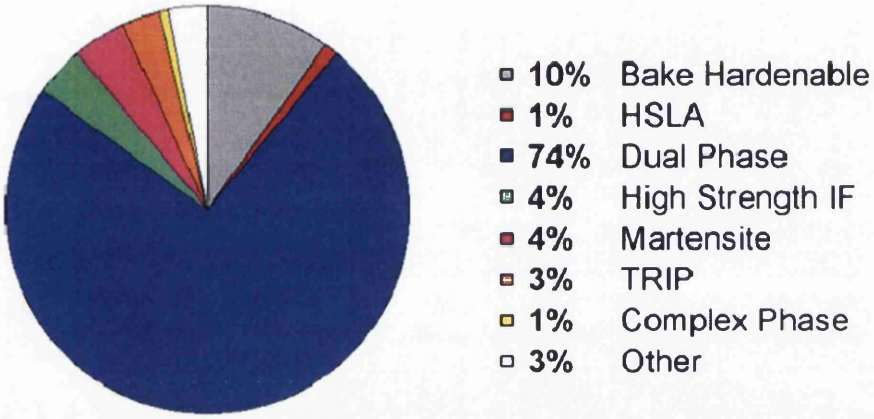

Figure 1.2 - Proportions of High Stength steels used in ULSAB-AVC vehicle by mass [7]

BH grades are attractive for such applications, as they offer a high level of formability, with $\bar{r}$ values of around 1.6 and elongation to failure of 30-40% [8] combined with a yield stress than can be improved following forming by 30MPA-60MPa (Figure 1.3) during a high temperature aging process (typically 170°C for 20 minutes)

A range of BH grades currently exist within the market – Corus produce a BH180 and BH220 grade. Nippon steel already produces commercial BH270 and BH340 grades [9] and POSCO produce a BH grade with a 185MPa yield and 340MPa tensile strength [10].

The challenge with BH grades is to increase the bake hardening response that can be achieved on aging. The strengthening effect occurs in two stages – firstly through the formation of solute atmospheres on dislocations, then through the nucleation and growth of nano-scale precipitates on the saturated atmospheres. The total strengthening effect achieved increases with increasing carbon content, but so does the propensity for room temperature aging and yield elongation effects. Commercially these must be kept below 0.2% yield point elongation following one hour at 100°C – equivalent to six weeks storage at room temperature (Figure 1.3). If this is not possible there is a risk of the formation of unsightly stretcher strains at the material surface during forming rendering the material unusable in external applications where appearance is important.

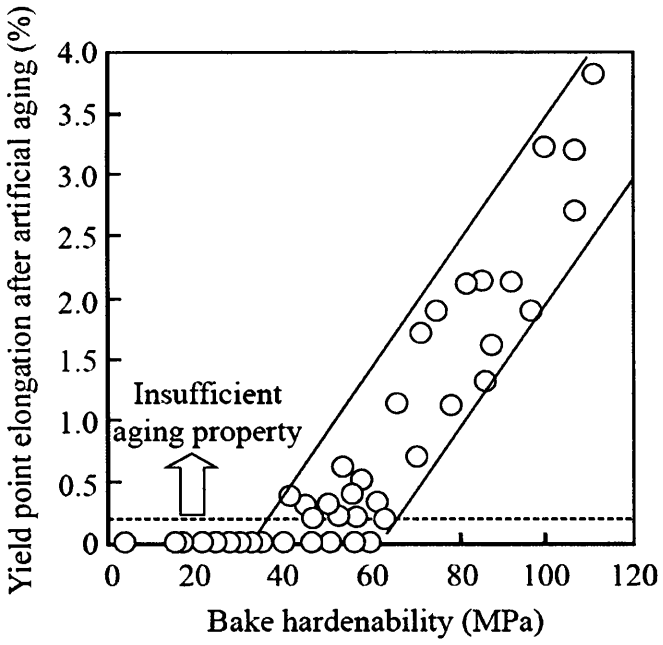

Figure 1.3 Evolution of yield point elongation as a function of maximum achievable bake hardening response, compared to the typical commercial guarantee of less than 0.2% return of YPE [9]

Computer models play an increasingly important part in the competitive position of modern metals based companies. Whether the focus of the commercial operation is in production of materials, such as within Corus, component forming, or joining of formed parts into a finished product, a high level of capital expenditure is required to launch a new product or process.

Within the automotive sector crash and corrosion performance are of paramount importance, and must be tested extensively prior to the release of a vehicle; time spent at the design stage, using Finite Element Models to predict deformation patterns [11] and finite difference code to predict corrosion performance [12], has the potential to reduce the number of revisions required through the testing process and thus speed up development and cut costs. Similarly the modelling of press forming or drawing operations, incorporating material properties, can be used to generate blanks of appropriate dimension and mechanical specification to ensure successful pressings, reducing the risk of damage to the dies, and lost productivity due to downtime.

Within primary steel manufacture computer models are no less important. Commercial software packages such as MT-DATA already exist, allowing the prediction of factors such as variation in the Ar3 (the line denoting the upper bound of the ferrite-austenite region in the metastable iron-cementite phase diagram) and Ar1 (the line denoting the lower bound of the ferrite-austenite region in the metastable iron-carbon phase diagram) temperatures with composition, as well as the sequential formation and relative stabilities of precipitates. Recrystallization, grain growth, and transformation models exist, and can be coupled with these,

providing information that is vital in the development of new grades, to give guidelines on processing temperatures and routes that will give optimum properties for a given application. Neural Networks have been derived to predict material properties as a product of chemistry and processing history [13], and finite difference models are commonly used to predict the solidification of castings and alloy segregation.

The aim of this body of work is to generate a novel model capable of predicting the strain aging behaviour of microalloyed steels as a function of their composition, improving understanding of the strain aging process, and allowing informed guarantees to be provided on the aging resistance and bake hardening response of strip steels.

A range of commercial Bake Hardening products already exist, so the challenge is to increase the bake hardening response that can be achieved through strain aging, while preventing room temperature aging for as long as possible. A body of evidence exists showing that vanadium has a retarding effect on strain aging [14-18]. One drive for this project is to determine to what extent novel BH grades, designed around vanadium additions, can offer an improved response in terms of bake hardenability and resistance to room temperature aging. The second is to produce a computer model capable of predicting the temperature dependent aging of Bake Hardening grades as a function of aspects of their compositions.

An aging model, as a desktop tool, could be used in the development of future grades providing savings both in terms of both time and money. Once the interaction

effects between free interstitial carbon atoms and substitutional alloying elements have been accounted for, chemistries could be tested rapidly to give a ballpark aging response before investing in the production of experimental casts. Models already exist describing recrystallization and precipitation phenomena, and, with the potential of models for modularisation using common outputs and variables, the addition of aging effects is a further step toward the through process modelling of a variety of steel compositions.

This project also serves to highlight the value of strong links between metallurgical knowledge and computational competency in the development of new models, in terms of generating relevant validation data over a range of scenarios and tailoring the model to the actual requirements of the end user.

1.1. Structure of the thesis

Chapter two contains a review of related work in the field of strain aging, covering the phenomenological processes occurring during aging, previous attempts to model the process, and fundamental aspects of common alloy chemistries. A lack of exploitation of vanadium-based bake hardening chemistries is noted.

Chapter three provides the detail of the experimental techniques used in the production of validation data for the strain aging-model, covering laboratory annealing, the measurement of free interstitial carbon, tensile testing and the bake hardening test, and optical and transmission electron microscopy.

Chapter four presents the background to the experimental program to produce validation data. The determination of the chemical compositions for the experimental steels, and development of annealing conditions using MT-DATA coupled with recrystallization considerations and the measurement of free carbon levels.

Chapter Five describes the experimental programme undertaken, covering the production of accelerated aging curves over the temperature range 50°C to 100°C with a range of carbon contents, both in the presence of, and without, a vanadium addition. Isochronal aging plots are developed to highlight the interaction of vanadium in retarding strain aging, and the Arrhenius aging kinetics are calculated.

Chapter Six presents a discussion of the experimental data, highlighting the retarding effect of vanadium additions beyond any expected grain size effects, and presenting TEM evidence of the existence of small, coherent precipitates in the annealed material, likely to be vanadium carbide.

Chapter Seven describes the authors work in reproducing an existing Kinetic Monte Carlo (KMC) model and adapting this model to use a different algorithm and framework, allowing the inclusion of features like secondary interacting species.

Chapter eight provides a discussion of the limitations and value of the computer models presented in this thesis.

Chapter nine summarizes the findings of this programme of work in a brief collection of conclusions.

CHAPTER TWO

REVIEW OF RELATED LITERATURE

2. REVIEW OF RELATED LITERATURE

Bake hardening (BH) steels are currently used widely in the automotive sector, for example in formed body panels such as outer door skins and bonnets. For drawing applications it is desirable for the r-bar value to be as high as possible, this value describing the average ratio of the true strain in the width direction to the through thickness strain during forming. With r-bar values of typically 1.8, and low yield strengths, in the region of 200MPa prior to forming, bake hardening steels are cheap to process into components. Heat treatment then improves the component strength and dent resistance [19-22].

Modern bake hardening products can be produced on continuous annealing lines, either through the use of higher levels of free carbon with an overage section to promote the nucleation and growth of intragranular carbides, or as fully stabilised IF chemistries in which precipitate dissolution can be used to liberate a controlled population of free interstitial carbon atoms. Bake hardening steels can represent more than 20% by mass of the body in white of a modern automobile [23] and this value could increased with the development of stronger bake hardening products, pushing up to 300MPa yield stress, or improved aging indexes or bake hardening responses, approaching the theoretical maximum of 90MPa [24].

In modern microalloyed bake hardenable sheet steels a yield stress increase is achieved through vacuum degassing and careful control of micro alloying additions (typically titanium and niobium) to leave 5-15wt.ppm of carbon in solution [25]; this level of carbon is not sufficient to be greatly detrimental to formability. During paint

curing, in which an auto body is heated at 170°C for around twenty minutes to cause the paint layer to set, free interstitial carbon can diffuse to the cores of dislocations under a 'drift velocity' caused by an interaction of the strain fields around the dislocation and misfitting solute atoms. This carbon then ties up the dislocations, locking them in place, and increasing the applied stress that is required to initiate dislocation glide. Following this treatment the material will be fully aged, the finished part displaying a yield stress increase in the range 34-70MPa [26]. Bake hardening is considered to have occurred. As the yield strength increase is achieved after the components have been formed, the forces required for pressing and drawing are kept low, and thus costs are reduced.

It is necessary to model strain aging and bake hardening effects for two major reasons. Firstly, component manufacturers require guarantees with regard to the aging characteristic of bake hardening steels at ambient temperatures. At higher carbon levels the aging process can progress at ambient temperatures to some extent, resulting in localised discontinuous yielding in the strip during forming operations, and the formation of unsightly stretcher strains [27] that render the product unsuitable for external body applications. Secondly, with the drive to reduce solvent levels in paints [28] there may be a move toward dry powder or water based coating solutions. It is necessary to determine how bake hardening grades will respond to a range of heat treatments should the current regime of twenty minutes at 170°C prove unsuitable.

2.1. The Processes of Strain Aging

In order to accurately model any process it is necessary to have a complete understanding of those factors or phenomena that are likely to impact upon it. Only with a full understanding of these effects can reasonable decisions be made in terms of which modelling techniques are applicable to the problem, and what level of detail the model requires to produce a sufficiently accurate solution.

A thorough representation of the aging process was presented by Wilson and Russell, who cited the typical changes in tensile properties over the aging cycle as determined experimentally for a high quality rimming steel [29]. Four separate stages in the aging process were identified (Figure 2.1):

i) In all samples an initial increase in yield stress occurred within two to four seconds at room temperature, related to the local ordering of interstitial atoms within dislocation stress fields, or Snöek rearrangement [30].

ii) Aged at 60^0C, over 35 minutes, the samples then showed a simultaneous increase in their lower yield stress and Lüders strain, with no significant change in other tensile properties. This is attributed to the formation of solute atmospheres around dislocations

iii) Further aging, 35 to 100 minutes at 60^oC, caused an increase in lower yield stress at a decreased rate, with little or no increase in Lüders strain; a change in the strengthening mechanism had occurred, moving to a precipitation or solute clustering event around the saturated dislocation atmospheres.

iv) Longer aging times gave a further increase in lower yield, accompanied by an increase in ultimate tensile strength and work hardening coefficient, with a reduced elongation to fracture. Eventually, after 10,000 minutes, this gave way to a reduction in tensile properties due to 'overaging'. Observations of this nature are typical of traditional precipitation hardening, which suggests that pre-precipitate clusters coarsen to produce incoherent precipitates.

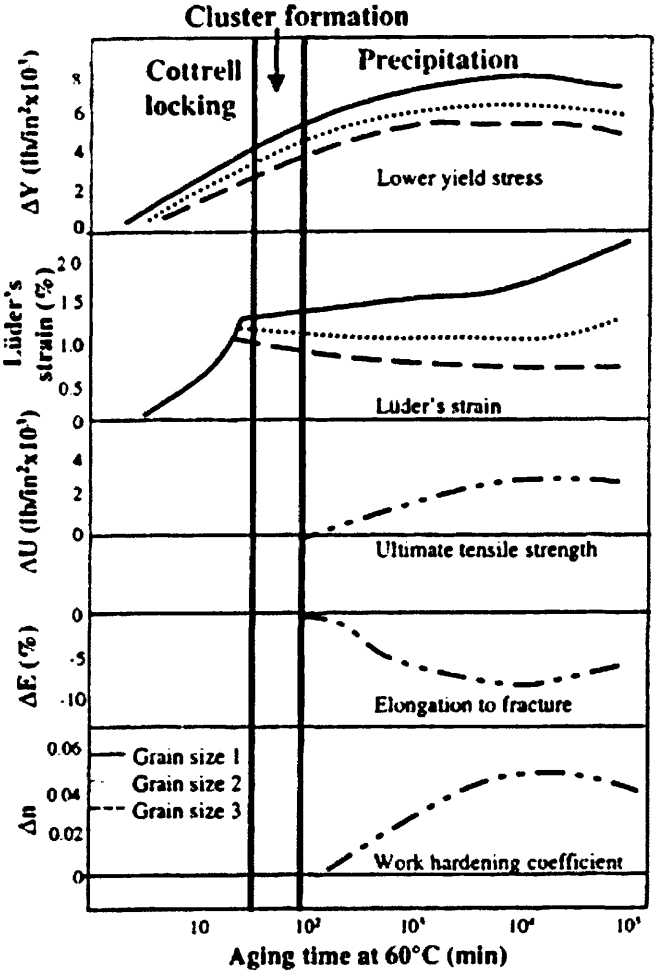

Figure 2.1 Effect of grain size on changes in mechanical Properties due to strain aging. Grain size in grain per mm squared: 1) 50; 2)195; 3) 1850 [29]

2.1.1. Snöek ordering

In body centered cubic (BCC) ferritic iron interstitial carbon and nitrogen atoms occupy the octahedral sites of the BCC unit cell. In an unstressed material the atoms are evenly distributed about these sites, and diffuse freely between them. In a stressed region of crystal some interstitial sites become enlarged, and as such it will be more energetically favourable for carbon atoms to occupy these due to the reduced level of lattice misfit. This causes a reordering of interstitial atoms to reduce strain energy [31]. Following this rearrangement the interstitial atoms are in energetically favourable positions, and slip will result in a small increase in the strain energy of the system, of the order of 1-2MPa [32].

Wilson and Russell observed this phenomenon as producing an instantaneous increase in yield stress at room temperature in a low carbon steel (0.038wt% C), and were able to confirm that the time scale was that for a single atomic jump of interstitial carbon [32]. This time scale was related to the relaxation times in elastic after-effect due to the ordering of carbon in iron. Similarly, Nakada and Keh [33] have studied this phenomenon in decarburised steels containing 0.0014wt.% carbon and between 0.013 and 0.023wt.% nitrogen, with similar results, supporting the theory that this initial strength increase results from Snöek ordering.

2.1.2. Atmosphere formation

In its currently accepted form, the theory of dislocation atmosphere formation was developed by Cottrell and Bilby in 1949 [34]. Due to their lattice misfit solid solution atoms can act to relieve the stress around a dislocation by forming solute

atmospheres, with large atoms gathering in the dilated portion of the dislocation field and small atoms in the compressed region. Application of a sufficiently large force will tear pinned dislocations free, allowing glide to occur at a lower applied stress. This produces the characteristic yield point phenomenon in strain-aged steels, which display an elevated yield stress, followed by a significant yield drop and the accumulation of Lüders strain.[35]

Cottrell and Bilby predicted that interstitial carbon atoms would segregate to a dislocation until a saturation point was reached, at which the addition of further atoms to the solute atmosphere would cease to reduce the dislocation energy. The final atmosphere was predicted to take the form of a central row of carbon atoms running parallel to the dislocation line, and just below its centre, surrounded by a dilute Maxwell-Boltzman distribution of solute in the lower half of the crystal. [34]

2.1.3. Precipitate formation

Where sufficient carbon is present, bake hardening results in a two stage aging process. This has been observed in steel containing 5wt.ppm of carbon aged between 50°C and 180°C by Elsen and Hougardy [25]. While the first stage is due to atmosphere formation, the second stage was attributed to the formation of coherent carbides. Aging had little effect on the strain-hardening rate of the specimens investigated, where the formation of incoherent precipitates would be expected to cause an increase in the strain-hardening rate. Additionally, the maximum increase in yield stress on aging decreased with increasing prestrain. A higher prestrain would result in a larger number of nucleation sites, and hence smaller particles forming. The stress required to cut coherent precipitates increases with the square root of

particle size; this was consistent with their observations [25]. No TEM lattice imaging was provided to support this theory in the paper.

An Ultra Low Carbon steel was studied by De et al., containing 21ppm of carbon in solution [36], measured by internal friction methods using a torsional pendulum operating at a frequency of 1Hz. The kinetics were described using an Avrami transformation equation:

$$W = 1 - \exp\left[-\left(\frac{t}{\tau}\right)^n\right] = 1 - \exp\left[-(kt)^n\right] \qquad 2\text{-}1$$

In which n and τ are constants, and W is the fraction of carbon precipitated. This allowed the precipitation process to be studied through the change in the exponent, n, during aging, determined using a *ln*[-*ln*(1-W)] *vs* *ln*t plot (Figure 2.2) [36].

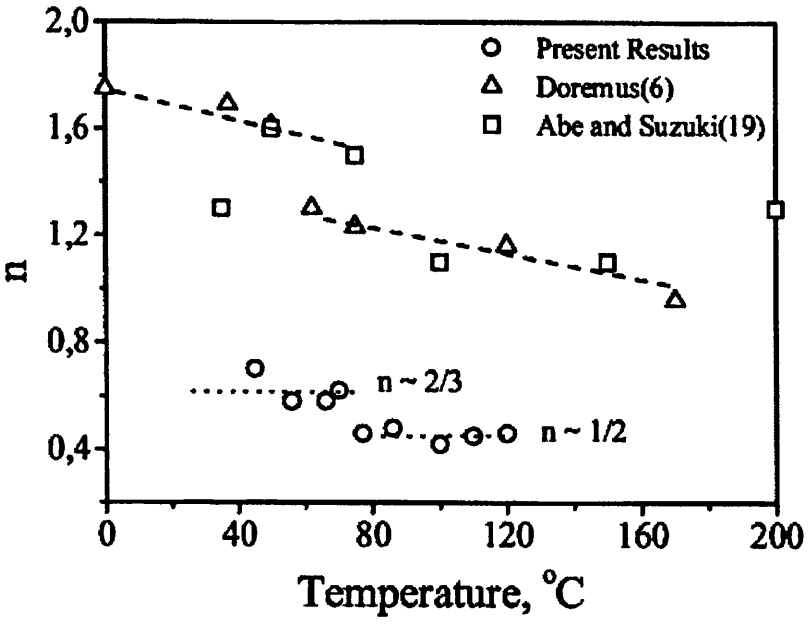

Figure 2.2 Variation of the JMAK kinetic exponent, n, with aging temperature during accelerated aging experiments [36]

Below 77°C a kinetic exponent of 0.58 to 0.70 was observed, in line with the value of 2/3 expected for dislocation interactions following traditional theories [34]. In accordance with traditional theories, carbon atoms are drawn to dislocations forming solute atmospheres, which, upon saturation, can form clusters that subsequently grow via rapid transport of carbon atoms along the dislocation line [29].

Above 77°C, the kinetic exponent was found to be between 0.42 and 0.48, suggesting a growth controlled process as clusters rapidly attain a critical size resulting in epsilon-carbide formation. The activation energies for these processes were found to be in reasonable agreement with reported energies from Sherman et al. for carbon cluster formation prior to Martensite formation [37] and for the precipitation of ε-carbide in low carbon steels. Sherman et al had performed their investigations on a range of Iron-Nickel-Carbon alloys, containing between 0.003 and 0.6wt.% carbon, with a greater emphasis on higher carbon concentrations. It was concluded by De et al. that, in the case of ultra low carbon steels, precipitation occurs initially by the formation of carbon clusters on dislocations, which may then transform to ε-carbide precipitates at sufficiently high temperatures, for which De et al. placed the lower temperature bound in the range 70-77°C.

Given sufficient time, and a high enough carbon content, the precipitates forming in the third stage of aging will further coarsen, increasing in size and reducing in number. At this point their efficiency in pinning dislocations will reduce and the softening or 'overaging' observed by Wilson and Russell will occur [30].

2.2. Numerical Modelling of Strain Aging

Historically many attempts have been made to model strain aging phenomena numerically. The majority of these describe the formation of carbon clusters on dislocations, without coupling this effect to a model of precipitate nucleation and growth. The value of such models is limited as, while they may reasonably describe the shape of the aging curve, they cannot be used to produce representative microstructures, nor confirm our understanding of the strain aging process as it occurs. Nonetheless they are included within this document for completeness, and as a source of data for a model; their derivations containing a number of interaction parameters that would otherwise be difficult to calculate.

The earliest numerical model of aging was produced by Cottrell and Bilby [34], taking the form of a rate law describing the degree of atmosphere formation after a time, t, assuming preferential drift of solute atoms under thermal agitation toward a stationary dislocation, as a result of the interaction energy between the two.

$$\frac{N(t)}{N_s} = n_0 \lambda 3 \left(\frac{\pi}{2}\right)^{\frac{1}{3}} \left(\frac{AD}{kT}\right)^{\frac{2}{3}} \qquad 2\text{-}2$$

In which N_s is the number of carbon atoms required per unit length of dislocation to form an atmosphere, N(t) the number of carbon atoms diffusing to a dislocation in time t (s), n_0 the average concentration of carbon atoms per unit volume of material (m^{-3}), A is a parameter describing the magnitude of the interaction between the

dislocation and carbon atoms ($3x10^{-20}$dyne.cm^2, or $3x10^{-19}$ Nm^2), D is the coefficient of diffusion for carbon (m^2s^{-1}), k is the Boltzman constant ($m^2\,kg\,s^{-1}\,K^{-1}$), and T is the absolute temperature (K) [34].

This equation was found to be reasonable for up to 30% completion of aging [34]. However, the model neglects the effects of solute depletion, atmosphere saturation and the reduced effect of later solute atoms, with regard to reducing the stress field around the dislocation; it also only accounts for the first stage of dislocation locking.

A modification was proposed by Harper to account for the reduction of solute remaining in the matrix over time [38]:

$$W = 1 - \exp\left[-3L\left(\frac{\pi}{2}\right)^{\frac{1}{3}}\left(\frac{AD}{kT}\right)^{\frac{2}{3}}\right] \qquad 2\text{-}3$$

In which W is the fraction solute that has segregated to dislocations and L the total length of dislocations per unit volume (m^{-1}). All other terms are as described for the Cottrell-Bilby equation above.

This assumed that the rate of precipitation would vary in proportion with the fraction of solute precipitated, due to solute depletion in the lattice. This equation still ignored back diffusion and saturation of the dislocation atmosphere, and as such could only be applied in the initial stages of atmosphere formation. It has since been superseded by other models that more accurately describe the physical processes that occur.

A subsequent numerical treatment by Bullough and Newman [39] accounted for dislocation saturation and back diffusion down the concentration gradient arising around the dislocation and, as with Cottrell and Bilby's original work [34], was compared with the results of Davenport and Bain. This model found $t^{2/3}$ kinetics to be reasonable to between 30 and 40% dislocation locking.

Elsen and Hougardy [25] have developed a relationship describing the increase in yield stress during aging as a function of the maximum strength increase obtained, which is purported to also account for the reduced effect of later solute atoms in reducing the dislocation stress field, and covers both the locking and precipitation aspects of strain aging

$$\Delta\sigma_{BH(t)} = \Delta\sigma_{MAX-I}\frac{\left(\frac{t}{k_c}\right)^{n_c}}{1+\left(\frac{t}{k_c}\right)^{n_c}} + \Delta\sigma_{MAX-II}\frac{\left(\frac{t}{k_p}\right)^{n_p}}{1+\left(\frac{t}{k_p}\right)^{n_p}} \qquad 2\text{-}4$$

In the above k_c and k_p are temperature dependant parameters following an Arrhenius type relationship, $\Delta\sigma_{MAX-I}$ is the maximum strength that can be achieved through Cottrell locking and n_c a constant (roughly 0.9); both of these parameters are independent of both temperature and prestrain. $\Delta\sigma_{MAX-II}$ is the maximum yield strength increase attributable to the precipitation event for the steel composition in question, and is independent of aging temperature, but varies with prestrain, and n_p is a constant that varies with temperature. It is stated [25] that relationships have been developed to determine these parameters from the temperature and prestrain used, but these relationships were not included in the published work.

More recently a predictive kinetic model specific to ultra low carbon steels has been presented, based on Cottrell's theory, taking into account remaining carbon in solution, atmosphere saturation and segregation of carbon atoms to grain boundaries [40]. The final rate equation reached was:

$$\frac{N(t)}{N_s} = \frac{1 - e^{3(L_0 - n_{0\lambda})V_{dis}t^{2/3}/2}}{1 - \frac{N_s}{n_0}e^{3(L_0 - n_{0\lambda})V_{dis}t^{2/3}/2}} \qquad 2\text{-}5$$

Here N(t) is the number of carbon atoms having arrived at a dislocation after time t (s), N_s the number of atoms required to lock that dislocation, N_0 the dislocation density (m^{-1}), n_0 the initial concentration of solute carbon atoms, λ is the dislocation slip distance, L_0 the dislocation distance per unit volume (m), t the time that has elapsed (s) and V_{dis} is a parameter describing the magnitude and range of interaction of a dislocation. This model was tested against experimental data for steels containing 6.4wt.ppm carbon, post-processing, as determined by internal friction methods. The samples were aged under a range of temperature regimes and the results, displayed in Figure 2.3, show a good agreement between the model and empirical data.

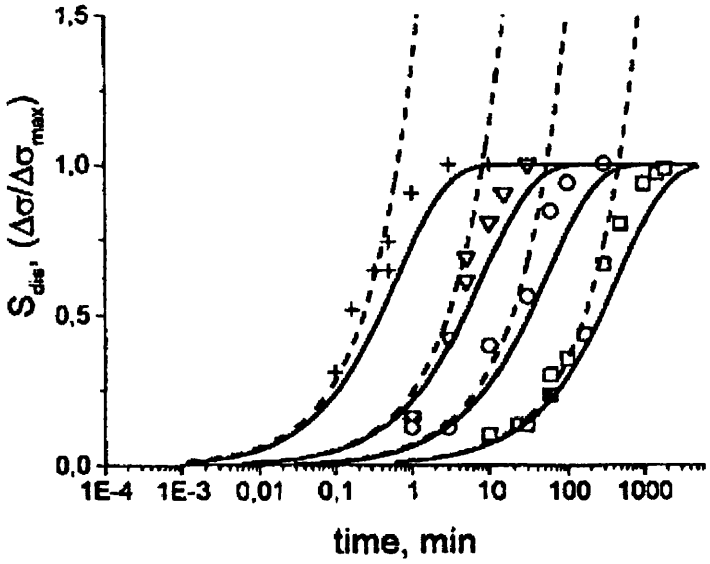

Figure 2.3 Fraction increase in yield stress and theoretical predications of the dislocation saturation level for 2% prestrain specimens aged at 140 (crosses), 100 (triangles) 75 (circles) and 50°C (squares). The dashed lines are predicted with Cottrell's formula, the solid lines predicted using the model presented.[40]

A different approach to the modelling of bake hardening effects has been taken by Berbenni et al [41], who have produced mathematical treatment of the aging process from first principles, based upon micro-mechanical considerations accounting for the hardening effects resulting from dislocation atmospheres forming, and from the subsequent formation of carbon rich clusters and nano-scale precipitates (these latter considered to be rod like in nature). This model has been used to simulate both the yield stress increase on bake hardening, and strain hardening curves following accelerated aging at 2% and 5% prestrain. The modelled curves after aging were around 50MPa above the experimental values, above 0.05 strain, but the modelled curve shape displayed the same trends as the experimental data.

2.2.1. **Analytical Treatment on Precipitation**

Attempts have been made to model the nucleation and growth of precipitates on dislocations following atmosphere formation. Cahn considered the nucleation of a roughly cylindrical incoherent precipitate on a dislocation [42], the precipitate having a circular radius, and this radius changing with position along the dislocation line. From the free energy per unit volume the critical radius was determined as:

$$r = \frac{\upsilon^{\beta}\gamma_{\alpha\beta}}{2\left(g^{\alpha} - g^{\beta}\right)}\left[1 \pm \left\{\frac{\left(g^{\alpha} - g^{\beta}\right)Bb}{\pi\upsilon^{\beta}\gamma_{\alpha\beta}^{\ 2}}\right\}\right] \qquad 2\text{-}6$$

In the above r is the radius of the precipitate (m), g^{β} and g^{α} the bulk free energy of the respective nucleating and parent phases (Jm^{-3}), υ^{β} the atomic volume of β (m^3), B a constant describing the extent to which the dislocation is mixed (varying from B_e to B_s for pure edge and pure screw dislocations respectively), b the burgers vector of the dislocation and $\gamma_{\alpha\beta}$ energy per unit length of the α–β interface (Jm^{-1}). [42]. If the release of bulk free energy and the dislocation energy terms are sufficiently large there will be no free energy barrier to nucleation (eg. If $\frac{\left(g^{\alpha} - g^{b}\right)Bb}{\pi\upsilon^{\beta}\gamma_{\alpha\beta}^{\ 2}} > 1$). If $\frac{\left(g^{\alpha} - g^{b}\right)Bb}{\pi\upsilon^{\beta}\gamma_{\alpha\beta}^{\ 2}} < 1$ there will be an energy barrier, with a magnitude equal to the difference between the positive and negative solutions to the equation. According to [43] the formation of Cottrell atmospheres by segregation corresponds to the latter scenario, with the saturated atmosphere corresponding to the metastable local

minimum energy configuration. Significant nucleation occurring where $0.4<\frac{(g^{\alpha}-g^{b})Bb}{\pi\upsilon^{\beta}\gamma_{\alpha\beta}^{2}}<0.7$.

Cahn went on to show that for an incoherent cylindrical precipitate forming on a dislocation the nucleation rate per unit volume on dislocations could be expressed as:

$$I^{D}=N^{D}\frac{kT}{h}\exp\left\{-\frac{(\Delta G_{c}^{D}+\Delta G_{a}^{D})}{kT}\right\} \qquad 2\text{-}7$$

Where I^D is the nucleation rate per volume, N^D the total number of atoms on dislocations k the Boltzman constant (m^2 kg s^{-1} K^{-1}), h Planck's constant, ΔG_c^D the free energy barrier to nucleation on a dislocation ($Jmol^{-1}$) and ΔG_a^D the free energy of activation ($Jmol^{-1}$).

There is evidence to suggest that the forming precipitates may be coherent in nature [25], and it has been proposed that these precipitates are cylindrical, lying along the dislocation line. The nucleation of coherent precipitates on edge dislocations has been considered by Dollins [44] for a spherical or disk like precipitate, which derivation and results were subsequently examined by Barnett [45] in light of the work of Eshelby.

These works determined the free energy change caused by such nucleation occurring, this being (for a spherical nucleus):

$$\Delta F = \frac{4}{3}\pi a^3\left(\Delta F_V^T + \Delta F_V^S\right) + 4\pi a^2\gamma_{coh} + W_1 + W_2 \qquad 2\text{-}8$$

In which ΔF is the free energy change on nucleation, α is the radius of the forming precipitate, ΔF_V^T is the chemical free energy change per unit volume of precipitate (Jm^{-3}), ΔF_V^S is the total strain energy per unit volume of precipitate caused by the precipitate(Jm^{-3}), γ_{coh} is the surface free energy of the coherent boundary(Jm^{-1}), W_1 is the interaction energy resulting from displacement at the precipitate surface and W_2 is the modulus interaction energy caused by the precipitate increasing the strain energy of the dislocation interaction field. [44]

The nucleation of a coherent spherical precipitate on a dislocation, including the chemical driving force resultant from local changes in solute content, was more recently examined for a nickel aluminium system by Xiao and Haasen [46]. Xiao and Haasen show that the free energy change on forming a small coherent precipitate near a dislocation can be expressed as [46]:

$$\Delta F^d = \frac{4\pi}{3}r^3(\Delta g_v^d + \Delta g_p^d + \Delta g_{p-d}^d) + 4\pi r^2\sigma^d \qquad 2\text{-}9$$

in which ΔF^d is the free energy change on formation of a nucleus of radius r in the strain field of a dislocation(J), Δg_V^d the chemical driving force within a dislocation strain field, Δg_p^d the misfit strain energy per unit volume of precipitate, $\Delta g_{p\text{-}d}^d$ the interaction energy per unit volume due to solute redistribution within the strain field of an edge dislocation and σ^d the the interfacial energy precipitate per unit length.

The constants above were derived in terms of species concentrations in the vicinity of a dislocation at which a Cottrell atmosphere has formed and the critical radius for successful nucleation calculated. It was shown that, in that region in which the misfit strain serves to minimise the strain energy of the dislocation, the critical radius for nucleation is decreased, while in that region where misfit strain is increased, the critical radius increases and nucleation will be heavily retarded. [46]

2.2.2. **Diffusion controlled growth**

One of the earliest models of diffusion controlled growth is the 'Zener model', which describes the radial growth of a plate like or cylindrical precipitate in a single linear direction [47].

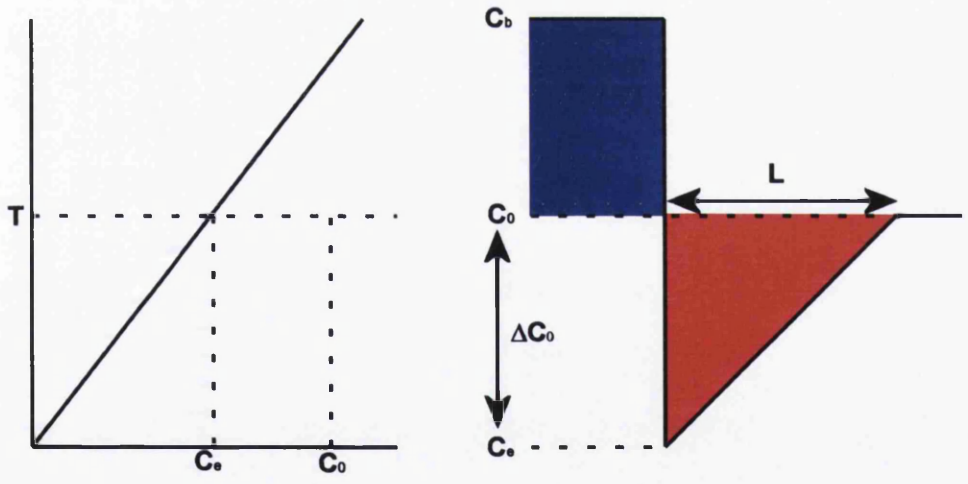

Figure 2.4 - Diagram accompanying Zener diffusion controlled growth derivation. Left: Phase diagram portion. Right: schematic of concentration field at advancing interface.

From Figure 2.4, assume an alloy of composition C_0 has been cooled to the temperature T sufficiently rapidly to prevent formation of the β phase. As particles of β form, the composition of α at the interface must be C_e.

For the interface to advance by a distance δx, $(C_b - C_e)\delta x$ mols of solute are required to diffuse down the concentration gradient e.g.

$$(C_b - C_e)\delta x = D\left(\frac{\delta C}{\delta x}\right)\delta t \quad \rightarrow \quad \frac{\delta x}{\delta t} = \frac{D}{(C_b - C_e)}\frac{\delta C}{\delta x} \qquad 2\text{-}10$$

The solute uptake in the forming precipitate must be equal to the solute depletion in the matrix adjacent to the interface. The change in composition over distance (assumed to be linear) is also easily calculated:

$$(C_b - C_e)x = \tfrac{1}{2}\Delta C_0 L \qquad 2\text{-}11$$

$$\frac{\delta c}{\delta x} = \frac{\Delta C_0}{L} \qquad 2\text{-}12$$

Substituting into equation (2-10)

$$\frac{\delta x}{\delta t} = \frac{D\Delta C_0^{\,2}}{2(C_b - C_e)(C_b - C_0)x} \qquad 213$$

Assuming the undercooling is low e.g. $(C_b - C_0) \approx (C_b - C_e)$,

$$\frac{\delta x}{\delta t} = \frac{D\Delta C_0^{\,2}}{2(C_b - C_e)(C_b - C_0)x} \approx \frac{D\Delta C_0^{\,2}}{2(C_b - C_e)^2 x} \qquad 2\text{-}14$$

$$t = \int \frac{2(C_b - C_e)^2 x}{D\Delta C_0^{\,2}} dx \qquad 2\text{-}15$$

$$t = \frac{(C_b - C_e)^2 x^2}{D\Delta C_0^{\,2}} \qquad 2\text{-}16$$

$$x = \frac{\Delta C_0}{(C_b - C_e)} \sqrt{Dt} \qquad 2\text{-}17$$

$$x = \frac{\Delta C_0}{(C_b - C_e)} \sqrt{Dt} \qquad 2\text{-}18$$

Therefore precipitate growth will be parabolic with respect to time where growth is diffusion controlled, the growth rate decreasing as the solute depleted region becomes longer and solute must diffuse further to supply the interface.

For diffusion controlled growth the kinetic exponent would thus be expected as 0.5; however, the Zener model cannot reasonably be expected to accurately describe the growth of precipitates nucleated on dislocations as it ignores capillarity effects and as such is unsuitable for situations where the radius of curvature is small, or where the precipitate radius is similar to the critical radius for nucleation. [43]

If a particle is sufficiently small the work done to increase the interface area during growth is not negligible and capillarity effects must be taken into account; the assumption of an equilibrium matrix composition as described by the phase diagram at the precipitate interface is not valid due to the influence of surface energy.

Additionally, in the case of epsilon carbide growth on dislocations during aging, expected to occur in ULC strip steels, there is a possibility of carbon being supplied to the growing precipitate by rapid transport along the dislocation. Love [48] presents a model of dislocation pipe diffusion in which self-interstitial atoms and vacancies are produced in pairs as a single atom moves across the dislocation core, and pipe diffusion occurs where a tracer atom diffuses to a vacancy along the core other than that which was created with it [48].

Miller et al [49]. have shown by atomistic computer simulation that the presence of edge dislocations serves to decrease the energy required for vacancy formation in BCC metals, giving a lower potential barrier to vacancy diffusion in spite of a higher migration energy. The energy barrier to vacancy formation can be as low as 60 to 80% of that in the bulk material; it is expected that this will be qualitatively true for solutes where the controlling mechanism for movement through the bulk material is vacancy diffusion [49]. This work also states that, with regard to interstitials, as these solute atoms are bound to the tension side of the dislocation where both formation energy of an interstitial and the migration energy are likely to be lower, pipe diffusion will be especially favoured.

2.3. Modelling Techniques

2.3.1. Introduction to modelling techniques

The realm of materials includes phenomena that cover a wide range of time and length scales; while at one extreme it is necessary to understand the stress strain characteristics and gross deformation response of large structures and components, at the other extreme atomic interactions affect the formation and behaviour of dislocations and nano-scale precipitates. Over the years models have been derived to describe and predict the way in which materials will behave, and while some of these may be solved analytically for simple cases, numerical solution using computers is common for large or complex problems. A range of modelling techniques now exists, each of which is applicable to a characteristic time and length scale. As such they can rapidly be assessed regarding their suitability for the problem at hand – the modelling of dislocation locking phenomena, and subsequent formation of nano precipitates.

Strain aging occurs over a number of processes, and across varying time and length scales. Dislocation locking, as considered by Cottrell and Bilby [34] occurs through the diffusion of interstitial atoms to dislocation sites as a result of a 'drift force' due to strain field interactions, with a time scale ranging from 10^3 to 10^5 seconds. This is followed by the formation of rod-like 'nanoprecipitates', that are likely to consist of ε-carbide ($Fe_{2.4\text{-}3.0}C$), and form along the dislocation network [25, 50].

Numerical models of the processes that occur during aging have been developed over the years [25, 34, 38, 51], these being able to predict the extent to which aging

will have progressed as a function of time and temperature; similarly, the maximum yield stress that can be achieved as a function of carbon content, and the propensity for room temperature aging have been investigated for a range of grades. It is hoped that, through the production of a kinetic computer simulation, other factors such as the kinetic influence of solid solution alloying elements [16], can be incorporated to give a more complete picture of bake hardening.

2.3.2. Monte Carlo

The range of techniques that fall under the purlieu of Monte Carlo Modelling are all related by the attempt to mimic stochastic processes by breaking them down into isolated events and performing a statistical analysis using an uncorrelated chain of pseudo-random numbers [52]. This involves either 'naive sampling', in which values are drawn with equal probability from the entire available phase space, or 'importance sampling', in which values are drawn with varying probability over a discrete region of phase space, which maps to a function roughly describing the process being considered. Importance sampling can be more efficient, and give a result that is more 'true' to the process being modelled; in atmosphere formation atoms are diffusing under a 'drift force', and, as such, diffusive jumps in the direction of the vector are statistically more likely. However, this is only the case if the chosen function is correct, and it is necessary to qualify any results produced in terms of the assumptions that have been made.

Among the earliest recorded uses of computational Monte Carlo techniques is Ulam and Von Neumann's 'random walk' simulation of Neutron diffusion in a fissile material, in which a diffusing neutron was assumed to be deflected in a random

direction on each successive collision as it passed through the material. Other uses have involved the solution of high dimensional integrals, using a 'hit-or-miss' technique', and solving Hamiltonian energy expressions [52]. The Hamiltonian describes the kinetic and potential energy of every atom considered in a system, and thus can be used to predict molecular interactions at the atomic level The original algorithm for use with such models was developed by Metropolis et al [53] to solve the state equation for a many body problem.

In this model every atom in the ensemble was assigned an initial position, and the energy of the system determined through solution of the Hamiltonian; the position of a single atom was then randomly altered, and the energy recalculated. Any move that resulted in a decrease in energy was accepted unconditionally. If the energy increased, a move might be accepted subject to the Boltzman Factor, which describes 'the non-normalised statistical weight with which the canonical phase space configuration occurs in thermal equilibrium' [52]; essentially the probability of a move occurring that would produce a configuration resulting in a quantifiable increase in net energy. Over a number of iterations such a model should eventually converge on the condition of minimum energy, but the moves taken in producing this state will not represent the kinetic evolution of a true system.

The problem of dislocation pinning represents a combination of the above applications of Monte Carlo processes. A modified 'random walk' would need to be produced for migrating interstitial atoms, accounting for changes in energy due to chemical interactions with other solutes and the change in elastic strain energy. A kinetic operator describing jump frequency would also be required, scaling with time,

to allow the study of microstructural evolution; traditional Monte Carlo techniques are frequently used for static studies, and may not give the actual configurations by which an equilibrium state is achieved. In dynamic studies the configurations generated are meant to simulate the temporal evolution of the system [54] and it is necessary to be able to convert t_s (the simulation time) to t_r (real time), and ensure that these two scale linearly.

Cao [55] reviewed two methods for incorporating real time into Monte Carlo simulations and presented a new algorithm of his own devising, supported by a computational experiment, through which this can be achieved. [55] For the first of these the real time is determined as

$$t_r = \frac{1}{N}\sum \frac{1}{w_e(C_i, C_f)} \qquad 2\text{-}19$$

Where w_e is the transition rate from a site C_i to a site C_f,(s^{-1}) and N is the number of particle that are diffusing. The factor 1/N arises because the diffusing particles (which each serve as a clock) are all counting time in parallel. Alternatively a Monte Carlo Time Step (MCTS) can be used to define the length of time required for an isolated particle to make a single jump; within each MCTS every particle under consideration is given the opportunity to make a single jump, allowing evolution of the microstructure over time.

Cao then considered a number of particles (N), able to make a number (M) of possible transitions, each having a defined transition rate w_i. It is shown that

$$\Delta t_r = \sum \frac{\tau_i^0}{M} \qquad 2\text{-}20$$

where τ_i^0 is the average waiting time between transitions occurring(s). Through the computational solution of a surface diffusion problem this new algorithm was found to be equally valid to the pre-existing forms.

It has been suggested that processor use can be optimised in Lattice Kinetic Monte Carlo by only simulating the 'defect' atoms, and adopting an event driven time step that constantly adjusts to suit the fastest process that is occurring [56]. These methods have already been used to model point defect diffusion and ion implantation in silicon-based semiconductors for microelectronic applications using the commercial software DADOS (Diffusion of Atomistic Defects, Object-oriented Simulator), developed at the University of Valladolid.

The Locally Activated Kinetic Monte Carlo algorithm proceeds by always adjusting the feature that is lagging the most in terms of time, and calculating a time step based on the frequencies with which that feature will change it's state, and is demonstrated in [57]. By comparison the Bortz-Kalos-Lebowitz (BKL) algorithm chooses a single state change from all the changes that are possible within the simulation, and generates a time step based on the cumulative frequency with which all events can occur. Both algorithms are discussed in more depth later in this thesis.

2.3.3. **Computer simulation**

A Kinetic Monte Carlo simulation of strain aging has been published by Soenen et al, accounting for both diffusion of carbon atoms to dislocations during aging, and grain boundary segregation during the annealing process, and the results of this group have shown a strong correlation with their experimental data (Figure 2.5) [57].

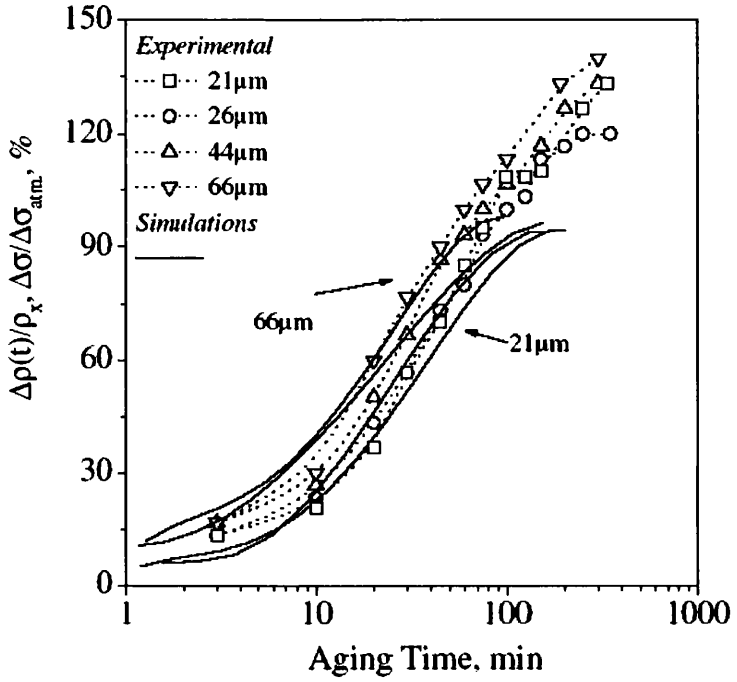

Figure 2.5 Comparison of calculated and experimental dislocation saturation evolutions with aging time (Steel containing 11wt.ppm carbon in solution, aged at 50°C, prestrain of 5%) as a function of grain size. [57]

The kinetics are controlled by a set of Arrhenius type equations controlling jump frequency, relating to; jumps between positions of equivalent energy within the bulk material; jumps to sites of higher or lower energy, within a critical radius around dislocations; jumps from the bulk material into the grain boundary sites, and vice versa.

Following each atom jump, the cumulative jump time of every atom is determined, the atoms are sorted, and the one that lags behind the most in time is selected for the next occurring move. The total simulation time can be taken as the cumulative jump time of the leading atom. [57]

Finally, A phase field model of solute segregation and coherent nucleation has been developed by Hu and Chen [58], and has been successful in reproducing solute segregation in the presence of a dislocation strain field, and coherent nucleation and growth of precipitates near to a dislocation, including barrierless coherent nucleation resulting from strain field interactions.

2.4. Metallurgical considerations in strain aging

Various strip steels have been found to exhibit strain aging phenomena over the years, but modern grades designed to show a favourable bake hardening response and high level of formability often have ultra low carbon levels (to the order of 30wt.ppm total carbon), with microalloyed chemistries based on titanium and niobium additions. As the focus of this project is the development of novel grades based around vanadium additions, it is these microalloyed chemistries that will form the focus of the initial stages of this review.

2.4.1. Titanium based chemistries

Assuming Mn levels are sufficiently low to suppress MnS formation, titanium microalloyed ultra low carbon steels can be considered to follow a precipitation sequence resulting in carbon being stabilised through the formation of TiC [59] i.e.

$$Ti + N \rightarrow TiN \qquad 2\text{-}21$$

$$Ti + S \rightarrow TiS \qquad 2\text{-}22$$

$$Ti + C \rightarrow TiC \qquad 2\text{-}23$$

This results in full stabilisation of carbon occurring with the stoichiometry:

$$Ti = 4\,C + 3.42\,N + 1.5\,S \qquad 2\text{-}24$$

An alternative scheme has been suggested [59-61] on the grounds of the differing C:N:S ratios between IF and HSLA steel grades, and experimental evidence. It is argued that for current commercial IF grades having higher sulphur contents, carbon is principally removed from solid solution through the formation of $Ti_4C_2S_2$, and that the role of free carbide precipitates have previously been overestimated.

During processing TiN nucleates while the steel is still liquid [62]; the titanium nitride acts as a nucleation site for epitaxial growth of TiS or $Ti_4C_2S_2$ during solidification. At temperatures above 1260^0C (eg. slab reheating) the carbosulphide is dissolved leaving a range of Ti_xS polytypes [61]. On cooling, the carbosulphide reforms in the temperature range $1260^0C > T > 950^0C$, although it has been shown that formation is strongly suppressed by rapid cooling and in situations where complete dissolution has previously occurred, resulting in preferential formation of TiC in spite of the higher thermodynamic stability of the carbosulphide phase [63] In the range $930^0C > T > 800^0C$ TiC was found to form through epitaxial growth.

Given sufficient titanium to tie up all the nitrogen and sulphur in solution, and low enough manganese levels to suppress the formation of MnS over TiS the titanium levels required for full stabilisation of an IF steel should be:

$$Ti = 3.42\ N + 2\ (1.5\ S) \qquad 2\text{-}25$$

2.4.2. Niobium based BH grades

In niobium based bake hardenable grades nitrogen and sulphur are removed by the formation of AlN and MnS, while carbon is scavenged by niobium to form NbC, [64]

$$Al + N \rightarrow AlN \qquad 2\text{-}26$$

$$Mn + S \rightarrow MnS \qquad 2\text{-}27$$

$$Nb + C \rightarrow NbC \qquad 2\text{-}28$$

Complete stabilisation of carbon to form an IF grade requires the addition of Nb in a 1:1 atomic ratio (a weight ratio of 7.74:1). Where a Bake Hardening response is desired this can be achieved through a high temperature continuous annealing sequence (>800^{0}C) resulting in partial dissolution of the NbC precipitates that have formed, followed by sufficiently rapid cooling to prevent re-precipitation of NbC (>20Ks^{-1} [35]), leaving a controlled level of carbon in solution.

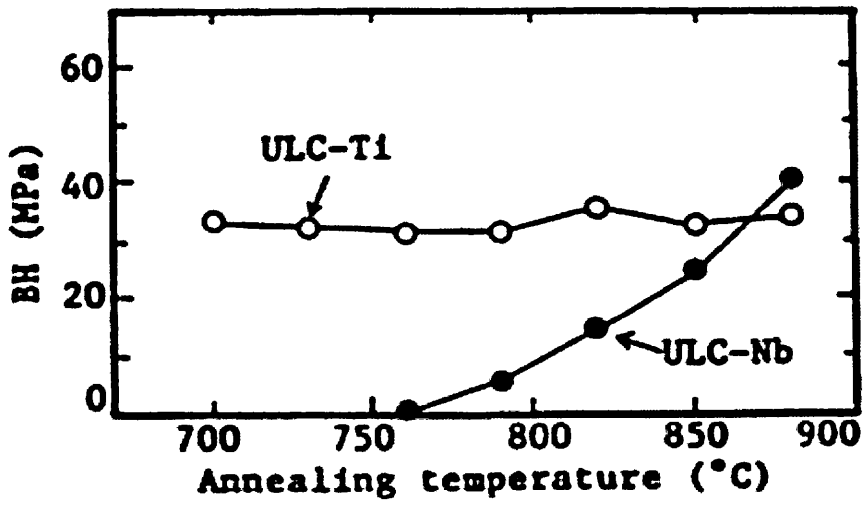

Figure 2.6 – The effect of annealing temperature on the bake-hardenability of Ultra low carbon titanium and or niobium added steels [65]

This has the disadvantage that the BH response achieved is dependant on the soak temperature used (Figure 2.6), and the use of exceptionally high temperatures can result in heat buckling during continuous annealing of sheet [65]. However, technique limits the level of free carbon in solution during recrystallization, which can improve the mean r vale of the steel produced. Free carbon will tend to delay the nucleation of the preferred 'cube on corner' texture during annealing, reducing the strength of this texture component and thus reducing the deep drawing quality of the steel.

Alternatively, a steel with bake hardening properties can be produced by under stabilising the carbon content, and the BH response has been found to improve using a substoichiometric Nb:C ratio [66]

2.4.3. Titanium – Niobium dual stabilised BH grades

Where dual stabilised grades contain low levels of manganese and sufficient titanium to stabilise the carbon content of the alloy (eg. Ti >3.42 N + 2 (1.5 S)) the mechanism of stabilisation can be considered to be that present in Ti only grades, with sequential precipitation of AlN/TiN, TiS, and $Ti_4C_2S_2$. It has been shown [59] that the formation of TiC and NbC occur epitaxially on $Ti_4C_2S_2$, and represent a small proportion of the carbon bearing precipitates. The majority of the niobium content remains in solid solution; if Niobium is retained in solid solution at concentrations above 0.025wt.% it can have a beneficial effect on texture development, increasing the strength of the {112} <110> component in hot rolled and annealed strip, and developing a stronger <110> partial fibre texture in the end cold rolled product, when

compared to a traditional aluminium killed steel. This serves to improve the r_m value of the steel [67]

Dual stabilised grades with a favourable aging response can be achieved in one of two ways.

1) It is possible to fully stabilise the nitrogen and sulphur content using titanium, then add a substoichiometric level of niobium, to leave the desired carbon level in solution.

2) A Bake Hardening response can be evolved during a high temperature anneal, which serves to partially dissolve the NbC precipitates. The annealing temperatures required for this process (800-850°C) can make production impractical using many galvannealing lines [35]

2.4.4. Vanadium based BH grades

As with Ti-Nb steels, Ti-V ULC grades can be expected to follow a similar precipitation scheme to those steels that are based solely on Ti additions. The precipitation effects in an experimental Ti-V ULC (Table 2-1) grade were recently examined by Ooi and Fourlaris [68].

Table 2-1- Grade composition used by Ooi and Fourlaris[68]

C	N	S	Al	Mn	Si	P	Ti	Nb	V	Fe
0.0033	0.0029	0.0030	0.0360	0.1700	0.0140	0.0120	0.0200	0.0040	0.0810	Balance

Analysis using SEM revealed the expected precipitates of TiN (formed during solidification or slab reheating), TiS and MnS, with a size distribution from 0.5μm to 2μm. Further analysis, performed using TEM, revealed several other features, in the 20-100nm size range. In combination with Energy Dispersive X-Ray spectroscopy (EDX) results it was shown that VC/$V_{0.88}$C precipitates formed on existing TiN particles in the matrix; this is a favourable precipitation event due to the incoherent interface between the FCC TiN and BCC low temperature ferrite, and the semi-coherent/coherent interface between the two FCC species TiN and VC.

This work found better properties for the Ti-V grade, in terms of formability, when compared to a grade of similar composition, but based solely on titanium stabilisation, at annealing conditions from 780°C to 820°C. The Ti-V grade displayed higher *r* and *n* values, with total elongation in the range of 45%. The elongation of the Ti-V steel was found to drop off with increasing annealing temperature in spite of increasing grain size, and it was suggested this occurred due to a dissolution of VC precipitates (expected to be dissolved under equilibrium conditions at 655°C) releasing carbon into solution.[68]

Interphase precipitation of TiC particles with diameters in the region of 20nm was identified in both steels, and further fine precipitates (<10nm) were discovered on dislocations. It was surmised that these were also likely to be TiC. Precipitation hardening as a result of TiC was found to be lower in the Ti-V dual stabilised steel; it was stated that lower Ti levels resulted in a reduced mobility of Ti atoms in the formation of TiC, retarding the precipitation and coarsening rates. As TiC precipitates hinder the formation of grain structures with a desirable texture during

recrystallization the reduced level of TiC in the dual stabilised grade was deemed to be favourable.[68]

The demonstrable ability to dissolve VC precipitates at temperatures typical for continuous annealing supports the concept of a vanadium based bake hardening product, utilising a controlled dissolution event. However, for this to be practicable slow cooling rates are required during coiling due to the low formation temperature of VC precipitates.

At present little data exists on the production of vanadium based BH grades, and there is some disagreement between authors in the field. In 1976 Rashid [14, 15] investigated the effect of titanium and vanadium on aging response using two commercially available HSLA grades, to determine the cause of reduced rates of strain aging, previously identified in comparison with plain carbon grades

The formation of Cottrell atmospheres was described using an Arrhenious relationship, and the activation energy for atmosphere formation was determined for each of the alloy chemistries, giving values in the range 33.6 to 35kcal/mole. These values were significantly in excess of those required for the diffusion of interstitial carbon and nitrogen. Rashid proposed a kinetic barrier to diffusion existed within HSLA steels, either in the form of an interaction between interstitial and substitutional solutes, or as an elastic effect resulting from the presence of coherent carbides in the steel lattice. This in turn resulted in aging proceeding at a reduced rate.

The aging response of dual stabilised Ti-V ULC grades was later assessed by Taylor and Speer, focussing primarily on continuously annealed products, annealed in the temperature range 788-871^{0}C. It was proposed that suitable levels of solute carbon may be evolved in vanadium stabilised grades through continuous annealing at a significantly lower temperature than is the case with Titanium or Niobium [16]. The temperatures required to produce 20ppm of free carbon in equilibrium are of the order 750^{0}C, 850^{0}C and 950^{0}C respectively for these. (Figure 2.7)

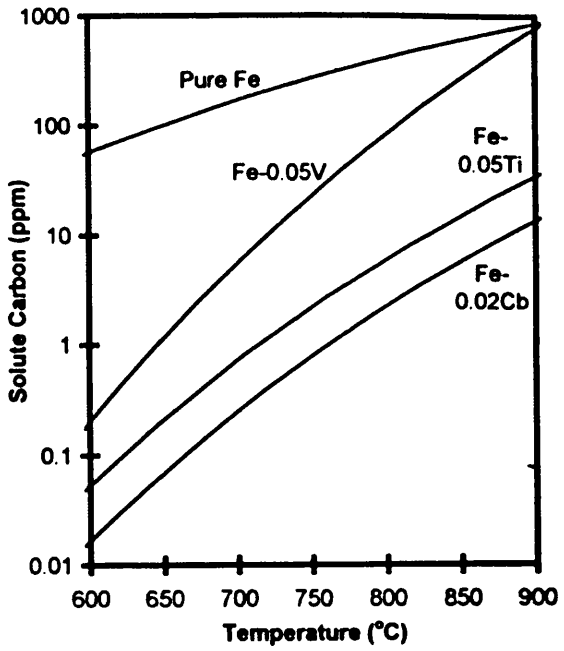

Figure 2.7 - Equilibrium carbon solubility in pure iron ferrite, as well as Fe-0.05V, Fe-0.05Ti, and Fe-0.02Nb [16]

The steels were 1%, temper rolled then prestrained by 2% prior to aging in an oil bath for 30 minutes at 176^{0}C. In theory full stabilisation should be possible at a V/C = 4.2, but it is stated that higher levels of vanadium may be required, as vanadium is only a moderate carbide former.

The Ti-V dual stabilised steel showed an increasing Bake Hardening Index with increasing carbon content, exceeding 40MPa above 0.002wt.%C. Under accelerated aging experimental results suggested a reduced susceptibility to yield point elongation in the dual stabilised steel, with acceptable resistance at carbon levels as high as 0.005%C (Figure 2.8), this corresponding to a BHI of around 70MPa. By comparison Ti stabilised steels show unacceptable yield point elongation above 0.003%C, with a yield point elongation greater than 0.2% following accelerated aging.

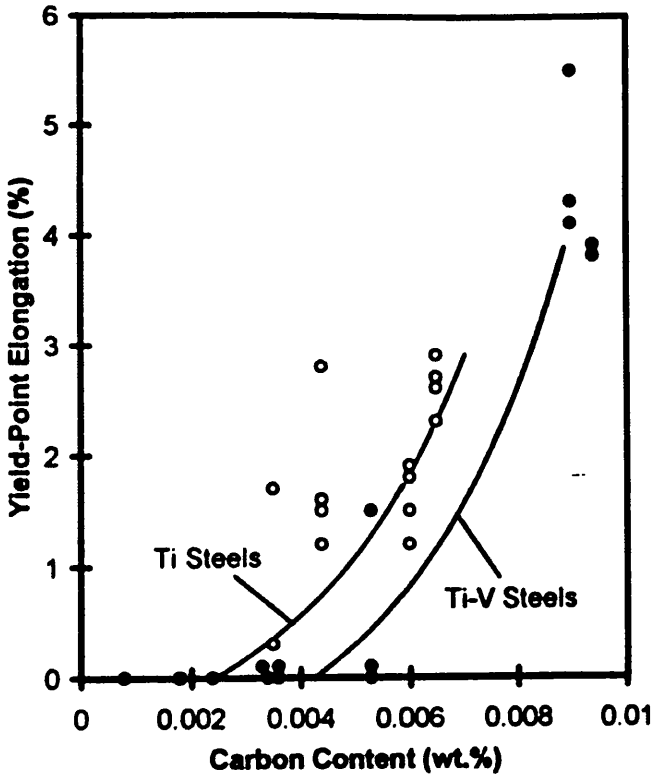

Figure 2.8 - Accelerated aging response of Ti and Ti-V bake hardenable steels [16]

It is suggested that, due to its high carbon affinity, vanadium may exert a kinetic influence on carbon in solution, reducing solute mobility; the role of the V/C ratio is also discussed, and it is shown, within the limits of their investigation, that as the V/C ratio increases from 0 to 41 the yield point elongation subsequent to accelerated aging drops from 0.8% to 0%. This effect is related to the affect of the V/C ratio on the equilibrium solubility of VC. While the relationship is not fully developed, it is demonstrated that the level of carbon existing in equilibrium with a known level of vanadium should be lower for increasingly higher V/C ratios.

While this appears to be in line with Rashid's earlier results, a subsequent study [69] found that during coiling VC did not form due to kinetic factors, and found no evidence of vanadium or the V/C ratio affecting yield strength, tensile strength or bake hardening index. However, the work of Taylor and Speer relied on controlled dissolution of VC precipitates during continuous annealing, while Girina and Bhattacharya[69] did not observe any precipitation to occur without hot band annealing, which is likely to account for the discrepancy. The absence of VC precipitates in the hot band is surprising, however, as in the manufacture of HSLA steels it is necessary to reduce the temperature on the run out table to around 600^0C to prevent the precipitation of coarse carbides. While a lack of carbide formation was observed in both hot-band and continuously annealed product, it is noted that hot band annealing served to tie up the existent free carbon, showing that VC will form given suitable kinetic parameters. [69]

A review on strain aging literature by Baird [18] has reported vanadium contents of 0.03 to 0.05wt.% as being sufficient to totally suppress low temperature strain aging

in rimming steels, and a reduced aging rate at elevated temperatures with increasing vanadium composition.

While the potential of bake hardening grades using titanium and niobium additions has long been exploited [35, 70], less work has been performed with regard to bake hardening products using combined additions of titanium and vanadium [16, 69, 71]. Historically vanadium has been found to have a retarding affect on strain aging as noted by Baird with reference to rimming steels and Rashid working with HSLA grades [14, 15, 18]. More recent attempts to prove this effect conclusively with reference to BH steels have disagreed [16, 69], but there is an existing patent held with regard to a non aging batch annealed grade using vanadium additions for this purpose [17]. Further work is clearly necessary to assess the retarding effect of vanadium additions with regard to the strain aging of ultra low carbon strip steel.

2.5. Factors effecting bake hardening response

2.5.1. The effect of varying carbon content

The increase in yield stress, commercially, occurs in two steps during paint curing; an initial strength increase due to dislocation locking, and a subsequent increase resulting from the formation of non-equilibrium carbides.

The increase in yield stress produced in bake hardenable steels is attributable to free interstitial carbon alone, as, to reduce the risk of room temperature aging, nitrogen is removed through the addition of strong nitride formers such as titanium. It has been shown that dislocation pinning requires approximately one atom of carbon per atomic plane threaded by a dislocation [30]. This corresponds to a carbon concentration of only 0.25 to 1.2ppm of free carbon in solution, for a tensile specimen pre-strained by 10% [72]. Accepting this, within the range over which aging is limited to atmosphere formation alone, additional carbon does not appear to increase the maximum tensile stress achieved during atmosphere formation, but rather decreases the time taken for saturation to occur.

Recent studies performed on ultra low carbon steels have placed the maximum strength increase attributable to dislocation locking alone in the region of 30MPa [36, 72, 73]. This is in agreement with the work of previous investigators [25, 30, 74].

The carbon level required in solution for nano scale precipitation to occur, giving a further increase in yield strength, has found less agreement between authors; De et al. found no evidence of a second stage strength increase when using a grade

containing 6wt.ppm of carbon in solution, but a mild rise in yield stress increase, to 35MPa, was obtained on increasing this level to 9wt.ppm [73]. By comparison Elsen and Hougardy, using a grade containing 5wt.ppm of carbon in solution, found clear two-stage aging to occur, with an initial rise in yield stress of 20MPa due to dislocation locking, and a further increase of up to 40MPa, depending on the degree of prestrain [25]. Rubianes and Zimmer similarly identified three aging regimes, in the range 0-12wt.ppm of carbon, with 5-6wt.ppm of carbon in solution giving a total increase in yield stress of around 60MPa, and adequate resistance to aging at room temperature [75].

The effect of free carbon concentration on aging response was investigated by Van Snick et al. [76], covering a range up to 114wt.ppm (Figure 2.9). The increase in yield stress on aging was seen to rise rapidly over the range 5-15wt.ppm of free carbon, beyond which the rate of increase dropped off, attaining a maximum value of about 72MPa beyond 40wt.ppm.

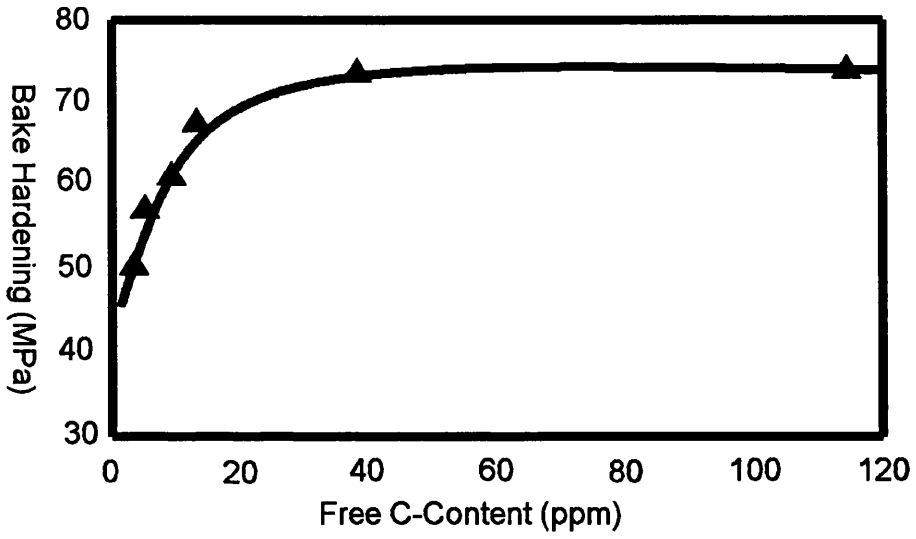

Figure 2.9 – The influence of free carbon content on bake hardening response (grain size 17um) [76]

In a study on bake hardening performed using Thermo Electric Power measurements (TEP) (Table 2-2) Massadier et al [24] reported a rapid rise in yield stress increase of 70MPa in the range 0-30wt.ppm of carbon, again levelling off at 40wt.ppm. The maximum yield stress increase obtained in their experiments was between 80 and 90MPa. [24]

Table 2-2 - Steel compositions used by Massadier at al in TEP study

	C 10^{-3} wt.% (ppm)	N 10^{-3} wt.% (ppm)	Mn wt.%	Al wt.%
Pure iron	0.5 or 1.5 (5 or 15)	0.2 (20)	$\sum$ Al, Si... $\leqslant$ 0.050	
Steel ULC_1	6.0 (60)	4.0 (40)	0.125	0.015
Steel ULC_2	7.0 (70)	5.0 (50)	0.250	0.016
Steel LC_1	23.0 (230)	5.3 (53)	0.200	0.050
Steel LC_2	59.0 (590)	4.8 (48)	0.400	0.048

While it is difficult to draw any definitive conclusions from the above, it is clear that bake hardening response is very sensitive to carbon content in the range 0-30 wt.ppm. A lower threshold appears to exist, below which nano-precipitation does not occur, limiting BH response to 20-30MPa. Similarly there is an upper threshold, above which aging is primarily controlled by the matrix precipitation event, and maximum bake hardening responses appear to be in the region of 80MPa. There is also evidence to suggest that bake hardening response increases with decreasing grain size [30, 76-79]. Elsen and Hougardy [25] state the ideal carbon range for BH grades as between 5 and 15wt.ppm to ensure a significant increase in yield stress, without too high a propensity for room temperature aging. Based on the investigations of R. Pradhan [80], carbon content should be controlled below 10wt.ppm to avoid room temperature aging.

2.5.2. **The effect of varying Grain size on bake hardening response**

A positive effect on bake hardenability with decreasing grain size has been reported by a number of sources,([77], [78], [79] [76],). Hanai et al. found that that the increase in yield stress was increasingly dependant on grain size where carbon and nitrogen in solution were above 10ppm, and cluster and precipitate formation could occur. For a given grain size there was a maximum yield stress that could be achieved by increasing solute carbon. Conversely, they reported grain size to have little effect where combined solute levels were below 5ppm, and Cottrell locking was the dominant mechanism of dislocation pinning.

Possible explanations were discussed by Van Snick et al., citing work by Obara and Yamazaki [76, 78, 81]. Obara et al. suggested that in larger grains there is an increased tendency for intragranular cementite precipitation. This is due to a higher degree of carbon supersaturation on cooling, as the diffusion path to grain boundary precipitation sites is longer. Where intragranular cementite is present during aging carbon will diffuse both to pre-existing precipitates and to dislocations, reducing the extent of dislocation pinning. Yamazaki et al. suggested the influence of grain size resulted from the location of dissolved carbon, as free carbon lying at grain boundaries cannot be observed using internal friction methods. During paint curing free carbon in the grain boundaries could diffuse into the grains and contribute to dislocation pinning. Van Snick et al. measured no change in measured free carbon with grain size, which tends to support the former of the two theories. In either case the Yield strength increase is typically related to $d^{-0.5}$ where d is the grain diameter.

2.6. Accelerated aging and room temperature aging resistance

The room temperature aging characteristics of bake hardenable grades are of vital importance, as these determine the length of time for which steel sheet may be stored prior to pressing operations, without necessitating an additional temper roll to avoid the formation of stretcher strains. While at elevated temperatures the onset of aging, and the return of yield point phenomena, occurs within minutes, at room temperature these processes are far more gradual. For the sake of experimentation it is useful to have a known correlation between the rate of room temperature aging, and aging at some higher temperature; without such a relationship the time scales involved in any kind of comparative study would be prohibitive.

Based on the theories of Cottrell and Bilby [34] Hundy derived equations, relating rates of aging to one another over a range of temperatures [82]. In the following carbon and nitrogen are considered to be the primary agents of aging in the former and latter respectively:

$$\log_{10}\frac{t_r}{t} = 4400\left(\frac{1}{T_r} - \frac{1}{T}\right) - \log_{10}\frac{T}{T_r} \qquad 2\text{-}29$$

$$\log_{10}\frac{t_r}{t} = 4000\left(\frac{1}{T_r} - \frac{1}{T}\right) - \log_{10}\frac{T}{T_r} \qquad 2\text{-}30$$

These equations are based on the assumption that the rate of aging can be considered in terms of the rate of diffusion of the interstitial species, and the

activation energy values used in their derivation are very similar to those for diffusion of carbon and nitrogen [83]. In the above t_r (s) is the strain aging time at room temperature, T_r (K). t (s) is the corresponding aging time at an elevated temperature T(K) . All temperatures are expressed in Kelvin.

These equations were shown to be reasonable using experimental data produced by Hundy, and by comparison with the results of other investigators, subject to the limitation that the amount of solute in solution does not vary as a function of temperature. This assumption should hold well in dealing with stabilised IF grades, due to the high stability of the carbides that could form. Typical paint baking cycles are of the order of 170°C, while the annealing temperatures required to dissolve carbon into solution are around 800°C. [82].

Accelerated aging tests tend to be performed at 100°C, in specimens that have undergone an artificially high temper roll. This over-rolling is performed to delay the onset of aging, and thus make for easier comparison of results. As shown in table 2, the temperature of 100°C is sufficient to give three months of room temperature aging over the course of one hour, and it has been stated that, if the Lüders strain remains absent after such a test, the steel should be stable in storage for as long as six weeks [26]. For comparative studies it has been suggested that lower temperatures should be used, to better highlight any differences that might arise in aging rate. Accelerated aging tends to be performed in either a hot oil or hot mineral bath, depending on the temperatures required. Tests at 100°C may also be performed in boiling water.

CHAPTER THREE

EXPERIMENTAL PROCEDURES

3. EXPERIMENTAL PROCEDURES

The purpose of the experimental work performed herein is to generate validation data for a novel Kinetic Monte Carlo model of strain aging that has been developed through the course of this research. The model has the capacity to recreate changes in the level of prestrain test coupons are subjected to, free interstitial carbon content, and aging temperature. The potential has also been included for expansion of the model to cover a range of secondary interaction effects, such as the known retarding effect of vanadium additions on rates of ambient temperature strain aging phenomena, and the addition of vanadium has been included as a test case for this capability.

3.1. Laboratory Annealling

Simulated annealing has been performed using the RHESCA Hot Dip Simulator owned by Corus RD&T Figure 3.1 [84]. This is an infrared furnace capable of heating rates of 35°C/s using 0.7mm sheet. The HDS is capable of annealing samples 200mm x 110mm in size with gauges from 0.6mm to 3mm, allowing each test piece to generate three 30mmx180mm blanks for 50mm tensile specimens, as per BSEN10002-2001 annex B [85]. Tensile coupons having a 50mm parallel gauge length were adopted for this body of work to cover the maximum possible number of conditions using a limited quantity of laboratory cast and processed material.

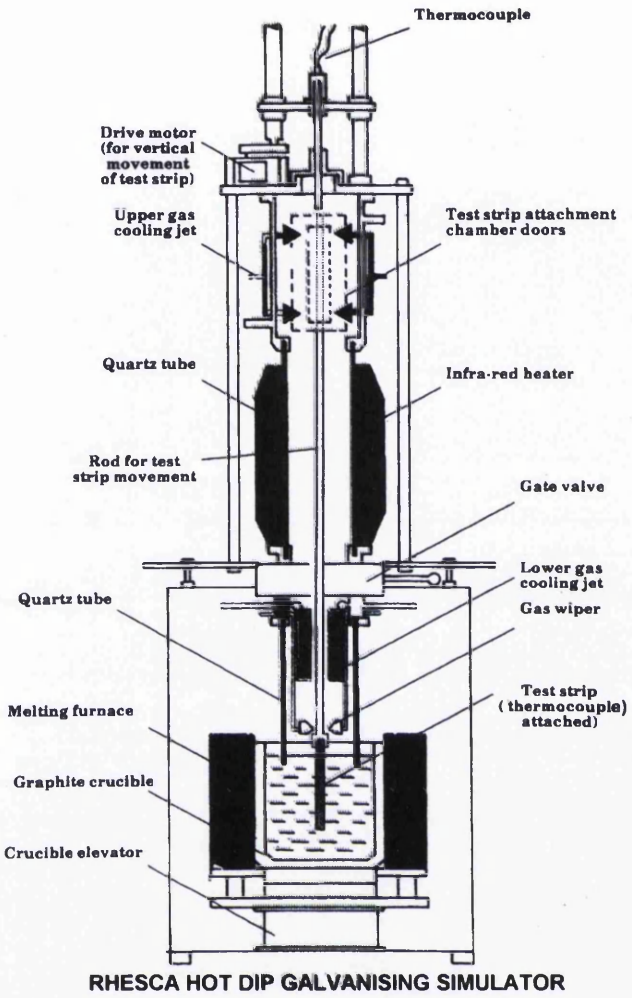

Figure 3.1 – A Schematic of the Rhesca Hot Dip Simulator at ECM^2, Port Talbot Steel Works, used for simulated annealing studies in this programmed of work. [84]

The infrared furnace elements are positioned within the furnace box alongside a quartz tube that contains the test strip, parallel to the width of the strip; there are 9 furnace elements on either side of the tube, these extending both above and below the limits of the sample. Prior to use the furnace was sealed and evacuated to a pressure of 0.2 Tor. The system was then flooded with nitrogen to atmospheric pressure. The use of a nitrogen atmosphere removes any risk of surface

decarburisation of the sheet – a critical factor when working with such low carbon compositions.

Temperature of the samples was computer controlled using a spot welded k-type thermocouple, positioned at the centre of the strip adjacent to the region that corresponds to the tensile test gauge, using a PID controller. Temperature control is possible to within +/-5°C at operational temperatures of up to 1000°C. The annealing cycle was controlled using a notepad based scripting language in which heating rates, cooling rates, temperatures and soak times were explicitly stated.

Under normal operating conditions cooling rates of 30°C/s can be achieved from a soak temperature of 800°C on 0.7mm sheet, using a flow of nitrogen gas over the sample at 400l/min to remove heat. The maximum achievable cooling rate is ~80°C/sec using a manually operated gas flow of 300l/min. with a 0.7mm panel, this rate decreasing as steel gauge increases. This cooling methodology was adopted in this programme of the work, the nominal steel gauge of 1mm giving initial cooling rates in excess of 60°C/s

3.2. Interstitial Carbon Measurement

Internal friction analysis has been carried out using a Vibran forced torsional pendulum operating in the frequency range 0.001-10Hz (Figure 3.2).

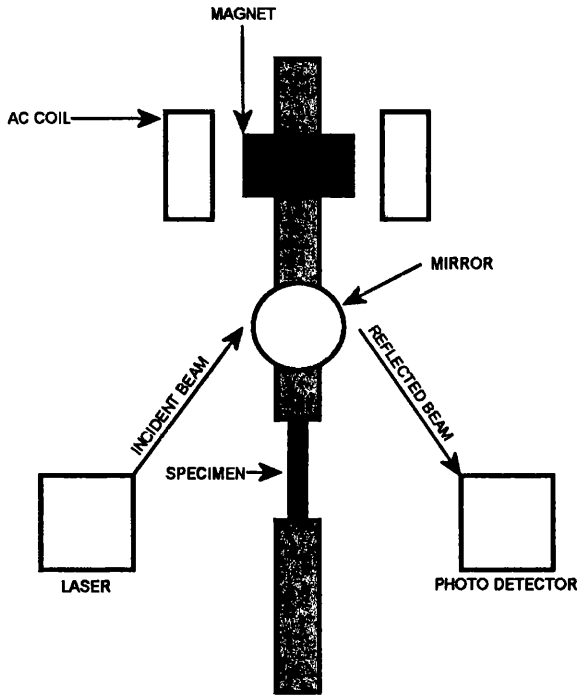

Figure 3.2 Schematic of the Vibran torsional pendulum used for interstitial carbon measurement via internal friction.

In the function of the torsional pendulum the test piece is held in tension between two vertical rods, the upper of which is free to rotate while the lower is fixed in place. An alternating current is applied through a coil surrounding a magnet attached to the upper rod, producing a deflection that in turn produces a torque in the test piece. Damping is measured by way of a laser and photocell; a laser beam is transmitted to

the photocell via a mirror attached to the upper rod, and the displacement of the beam can be measured. Torque-displacement pairs are then used to calculate the level of damping, and a plot of damping against frequency is produced [35]. A previous investigation [35] reports this set-up as being capable of resolving to 1wt.ppm, and having a high level of repeatability (ten successive tests on a single sample showed a variation of less than 1wt.ppm in carbon content)

Specimens were machined by spark erosion from 110mmx20mm blanks to a 'dog bone' shaped test piece with a parallel gauge length of 40mm and parallel gauge width of 4mm (Figure 3.3).

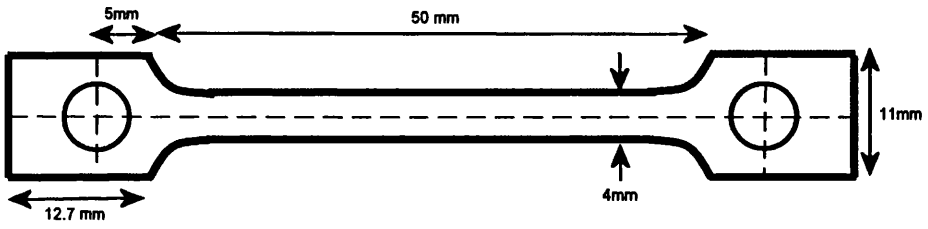

Figure 3.3 - A Schematic of 'dog bone' type internal friction test piece used with the Vibran Torsional pendulum for free interstitial carbon measurement.

Spark erosion was used to minimise deformation and avoid any risk of carbon pickup; following machining test pieces were kept in a freezer below -20°C to prevent ambient aging.

Following testing the damping vs. frequency data was de-convoluted using the solver feature of Microsoft Excel, assuming the data to take the form of the sum of multiple Debye type curves [86]

$$\frac{1}{Q} = 2\,x\,B_1 \frac{\left(Freq./F_1\right)}{\left(1+\left(Freq./F_1\right)^2\right)} + 2\,x\,B_2 \frac{\left(Freq./F_2\right)}{\left(1+\left(Freq./F_2\right)^2\right)} + Q_0 + S_0 \log(Freq.) \qquad 3\text{-}1$$

In the above 1/Q is the instantaneous measurement of damping, Freq. the instantaneous frequency, B_1 and B_2 the heights of the observed peaks, F_1 and F_2 their positions, Q_0 the background damping at 1Hz and S_0 the slope of the background damping (assumed to be linear). A two peak curve fit was used, allowing for the existence of a peak for carbon (expected at 0.1Hz) and a potential peak for nitrogen (expected at 1Hz).

Curve fitting to the data was achieved via a minimisation of the root mean squared error. A linear background was removed across the data set, subject to the condition that the minimum adjusted point was greater than or equal to zero. The raw data was then subtracted from the fitted data, and the sum of the squared error calculated. This value was then minimised using solver, with the peak heights and positions, and the gradient and intercept for the linear background used as variables.

3.3. Tensile Testing

Tensile testing has been performed in accordance with BSEN 10002 [87] using a calibrated Zwick 1474 tensile testing machine containing a 100kN load cell. Type 2 samples having a 50mm parallel gauge length, as described in BSEN 10002, annex B, were taken parallel to the rolling direction of the strip and mechanical properties determined in accordance with BSEN 10002 part one.

The test consists of straining a test piece in tension to fracture for the determination of mechanical properties; for a controlled test under ambient conditions the temperature must be within the range $18^{o}C<T<28^{o}C$. Over the course of the test load extension data is collected; this data is then converted to stresses and strains, given that:

$$\sigma = \frac{F}{a} \qquad 3\text{-}2$$

$$\varepsilon = \frac{L - L_0}{L_0} \qquad 3\text{-}3$$

Where σ is the instantaneous stress (Pa), F the instantaneous force (N), a the initial cross sectional area (m^2), ε the strain, L the instantaneous gauge length of the test piece and L_0 the initial gauge length of the test piece. The determination of the original cross section must be accurate to within 2%, with the error in the width being measured to an accuracy of 0.2%. As such width and thickness measurements are taken as an average of three micrometer readings taken along the length of the test gauge [21].

Specimens were loaded against a backstop to ensure that they were strained parallel to the gauge length, and changes in width and length measured using built in extensometers. Data from the tests was logged automatically by an attached personal computer, and subsequent data analysis performed in Microsoft Excel. Tensile prestrains were performed with a constant strain rate of 25mm/min. Tensile tests were performed with an initial strain rate of 10mm/min up to the end of any yield point elongation, increasing then to 25mm/min. The end of yield point elongation was identified by the nominal stress varying by more than 2% from the 0.2% proof stress for a given specimen. Young's Modulus was calculated between one third of the nominal proof stress, to a minimum of 110MPa, and two thirds of the nominal proof stress.

3.4. Determination of aging response

Bake hardening and aging responses have been determined by performing an interrupted tensile test on a given specimen. The specimen cross section was determined by taking an average of three micrometer readings of the sample thickness and width along the 50mm parallel gauge section. A 5% tensile prestrain was then performed, ensuring the sample had been pulled fully through any yield point elongation. A note of the maximum flow stress attained during the 5% prestrain was made.

The sample was then subjected to a furnace heat treatment in a calibrated fan assisted Carbolite Oven, controlled by an internal platinum-rhodium k type thermocouple, having temperature control within 1°C excepting the recovery time required after opening the door to introduce samples To mitigate this problem the oven was heated to the desired temperature a minimum of an hour before any aging treatments were under taken to increase the amount of heat stored in the furnace body and reduce the recovery times as far as possible.

For bake hardening response this treatment was twenty minutes at 170°C to simulate industrial paint curing operations in the automotive sector. Where an accelerated aging response was required the time and temperature of the heat treatment varied with the requirements of the experiment, in the temperature range 50°C to 100°C and time scales from 2 minutes to 1000 minutes.

Following heat treatment the sample was then strained, to failure, and the lower yield point following aging compared to the maximum flow stress achieved during the prestrain:

$$\Delta BH = LYP_{(baked)} - R_{px\%(unbaked)} \qquad 3\text{-}4$$

Where ΔBH is the yield strength increase resulting from aging treatment (MPa), $LYP_{(baked)}$ (MPa) is the observed lower yield point following the baking treatment and $R_{px\%(unbaked)}$ is the flow stress observed at x% strain during a tensile prestrain prior to baking. The adopted measure of ΔBH was the BH5 value, in which the 5% flow stress is used; while less common than the BH2% value, this was necessary due to the high level of yield point elongation in the

3.5. Metallographic preparation and grain size determination

Metallographic samples were cleaned using isopropanol to ensure the sample surface was free of grease or other contaminants, and provide the closest surface adhesion possible with the mounting resin.

Samples were then hot compression mounted in Type E Vynylec, using a Struers Predopress. The samples are placed in a cylindrical chamber within the Predopress and the mounting compound introduced as a powder. The chamber is then sealed, and the compound heated to 190°C for four minutes to ensure that it is fully liquefied. A pneumatic ram then applies a pressure of 20kN to the sample for 15 minutes, prior to a ten minute water cool.

Following mounting samples were subjected to mechanical preparation, in which the surface was abraded using progressively finer grits to produce a polished surface suitable for analysis using optical microscopy. Firstly a pre-grind was performed using a 120 grit SiC and 300 grit SiC papers on a manual wheel to flatten the specimen and remove excess material which may have been deformed during the cutting operation. Fine grinding was then performed using a 500 and 1000 grit SiC paper with a Rotopol automatic grinder, to remove the deep scratches produced during coarse grinding and leave a surface suitable for polishing.

The surface was then automatically polished using polishing wheels, with 6μm and 1 μm diamond paste and water based lubricant.

Mounted samples were examined using a Polyvar microscope at 500x magnification. For each specimen three randomly spaced micrographs were taken using a digital camera with image resolution 1.8 Megapixels to give a representative image of the microstructure. These were then used for grain size determination using the Heyn's Linear Intercept technique as described in ASTM E112 –96 (2004).[88]

On each sample eight straight lines of length 150μm were drawn, with two lines each at 0°, 45°, 90° and 135° to vertical respectively (Figure 3.4). In excess of 100 total intercepts were measured on each sample, the average grain diameter being determined as the length of the line, divided by the number of intercepts with grain boundaries.

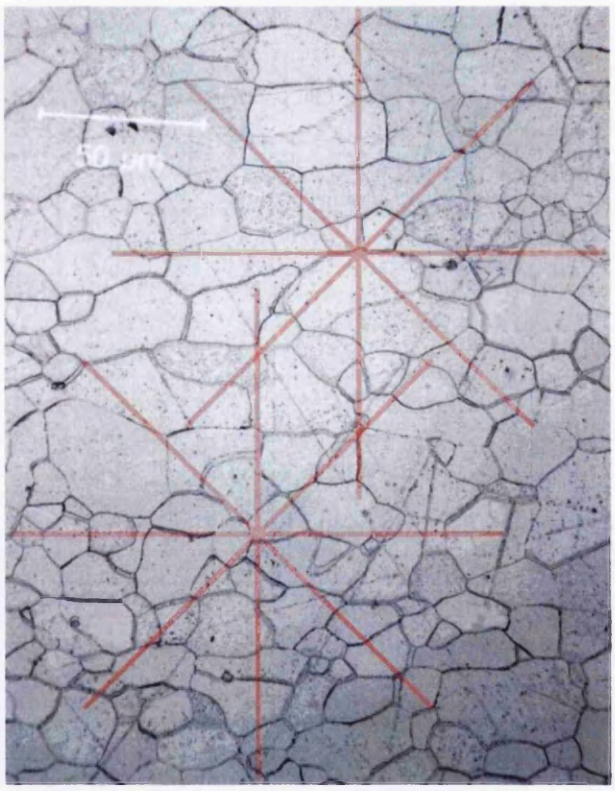

Figure 3.4 –A graphical representation of the Heyn's Linear Intercept Technique. Red lines are 150μm in length, and taken at 0°, 45°, 90° and 135° to the rolling direction of the strip.

Transmission Electron Microscopy

Transmission Electron Microscopy has been carried out by an expert operator at the Swinden Technology Centre, run by Corus RD&T at Rotherham. Images were taken using a calibrated Phillips EM400T TEM with a magnifying factor of up to 170,000 times (the calibrated factor being 173,300 times). Precipitates were viewed using bright field imaging, allowing the presence of small coherent precipitates to be inferred using strain field contrast. Precipitate compositions were determined using Energy Dispersive X-Ray Spectrometry, and precipitate sizes determined using the free UTHSCSA ImageTool program [89]

The TEM technique is used to examine the internal structure of thin (<200nm) samples of an investigated material. The image is formed by passing a beam of electrons through the sample, this beam being produced via thermionic emission, typically from a heated tungsten filament.

The electrons produced are accelerated toward the sample using an applied potential difference, typically in the range of 50-100kV [90] with higher accelerating voltages used for high resolution work. The image is produced as a result of electron diffraction by the atomic structure of the sample. Strong diffraction will only occur where regular features are spaced with a similar frequency to that of the incident radiation falling upon them. In order for the result of electron diffraction through a crystal to be visible it is necessary that the diffracted rays interfere constructively, for which they must obey Bragg's law

$$n\lambda = 2d\sin\theta \qquad 3\text{-}5$$

Where λ is the wavelength of the incident radiation, d the spacing between atomic planes and θ the angle that the incident beam makes with the sample surface.

If the objective aperture is positioned for those electrons that pass directly through the specimen without being strongly diffracted a 'bright field' image is produced. In such an image defects may be revealed as darker regions on a light background due to 'diffraction contrast' [90], as the local strain field produces variations in the diffraction conditions for the periodic lattice. Precipitates may also be visible due to differences in atomic mass or crystal structure.

If the objective aperture is positioned to collect diffracted electrons then a 'dark field' image is produced. Here defects that are correctly aligned to diffract strongly will be resolved as light areas on a dark background.

3.5.1. Precipitate Imaging

Strain Field Contrast

A coherent precipitate with a differing lattice parameter to the matrix will produce an elastic distortion in the matrix surrounding it; the crystal will have different diffraction properties locally. If the electron beam is angled such that the regular lattice planes are in the Bragg condition, precipitates will appear as darker regions in a bright field image, broken by a central 'line of no contrast' (assuming the particle displays spherical symmetry). [91] Particles near to the sample surface will appear

asymmetric due to local relaxation of the strain field. This asymmetry can be used to determine the nature of the lattice misfit (tensile or compressive).

Matrix Displacement Fringe Contrast

Thin planar precipitates displace the matrix planes adjacent to them on either side producing a phase change in the diffracted beam. This produces an image containing a series of bright and dark fringes, denoting contours of constant depth in the foil and running parallel to the plane containing the precipitate and the foil surface [91].

Orientation Contrast

Where a precipitate has a crystal structure that differs significantly from that of the lattice it will diffract differently. This is the most common form of viewed contrast, and can be used in high resolution dark-field TEM to analyse precipitate size and shape distributions without the added factor of matrix strain effects.[91]

CHAPTER FOUR

EXPERIMENTAL BACKGROUND

4. EXPERIMENTAL BACKGROUND

4.1. Experimental Composition

Given the high solubility of vanadium carbide in ferrite, relative to niobium and titanium carbides [16], steel grades were developed for this project with the intention of producing a controlled population of free interstitial carbon atoms via annealing. The steel compositions were designed by Dr. Fourlaris of the Physical Metallurgy and Phase Transformation group at Swansea University, to contain the lowest possible levels of any elements that might result in a significant interaction with free carbon atoms aside from the titanium and vanadium central to the project (table 4.1).

Table 4-1 Steel compositions used in the experimental program

	C	Si	Mn	S	P	Ti	Nb	V	Al	N
Steel 1	0.0039	<0.005	0.07	0.003	0.006	0.028	<0.001	<0.001	0.004	0.0025
Steel 2	0.004	0.007	0.094	0.004	0.008	0.025	<0.001	0.085	0.009	0.0036

Steel one was designed to be fully stabilised with respect to carbon, via the sequential formation of TiN, TiS and TiC. Accepting this precipitation sequence the weight percentage of titanium required can be calculated as $Ti^* = 4\,C + 3.42\,N + 1.5\,S$ [59]

$$Ti^* = (4 \times 0.0039) + (3.42 \times 0.0025) + (1.5 \times 0.003) \quad 4\text{-}1$$

$$Ti^* = 0.02865 \text{ wt.\%} \quad 4\text{-}2$$

$$Ti^* - Ti = 0.00065 \text{ wt.\%} \quad 4\text{-}3$$

The steel is sub-stoichiometric with respect to titanium by 0.00065 weight percent. Given the 1:1 stoichiometry of titanium and carbon in TiC, and their relative atomic masses, this results in 1.65wt.ppm of free carbon in solution under equilibrium conditions.

Steel two has been designed to be sub-stoichiometric with regard to carbon stabilization via titanium, the remainder of the free carbon being tied up by the large excess of vanadium as VC or $V_{0.88}C$.

$$Ti^* = (4 \times 0.004) + (3.42 \times 0.0036) + (1.5 \times 0.004) \qquad 4\text{-}4$$

$$Ti^* = 0.0343 \text{ wt.\%} \qquad 4\text{-}5$$

$$Ti^* - Ti = 0.0343 - 0.025 = 0.009312 \text{ wt.\%} \qquad 4\text{-}6$$

Under equilibrium conditions steel two should have 23wt.ppm of free carbon remaining to form vanadium carbide following TiC formation, assuming no mixed precipitation.

4.2. Experimental Processing

All experimental grades used have followed the same processing route following casting. Casts were made up as 25Kg ingots and processed under laboratory conditions by the Centre Researche de Mettalurgie (CRM) in Belgium. The casts were then reheated to 1250°C, sufficient to dissolve all sulphides present in the steel [92], and forged down to 50mm flats. The slabs have then been reheated to 1175°C and laboratory hot rolled down to 5mm strip, with a finishing temperature of 920°C to ensure that finishing occurs above the Ar_3 and recrystallization is complete throughout the strip.

Laminar water-cooling has then been performed to rapidly cool the steel to the coiling temperature of 700°C. Titanium steels are robust to variations in coiling temperature due to the high stability of TiC within this temperature range, but rapid cooling and a relatively low coiling temperature suppress grain growth in the hot band, improving formability in the finished product. The strip was then furnace cooled to room temperature at 28°C/hr to simulate industrial coil cooling; this slow cooling rate is vital for the development of the dual stabilized titanium-vanadium steels due to the low formation temperatures of vanadium carbides [68].

Following coiling a multi-pass cold rolling reduction of 80% was applied to the strip, giving a nominal gauge of 1mm. A high level of cold reduction was preferred to increase the level of stored energy in the strip, providing a driving force for recrystallization during subsequent annealing.

4.3. Determination of annealing conditions

MT-DATA has been used to predict the weight fraction of precipitates in the alloy as a function of temperature, and the equilibrium weight percentage of species in solution in ferrite as a function of temperature, as a tool to aid in deriving annealing conditions. Consideration was also given to expected times for full recrystallization predicted using the Larson-Miller parameter.

4.3.1. MT-DATA Studies

The masses of various precipitate species in solution under equilibrium conditions have been predicted using MT-DATA thermodynamic modelling software. Figure 4.1 shows the equilibrium precipitation scheme for steel one based on the actual composition received. Stabilisation would proceed initially by the formation of TiN followed by MnS, and finally the stabilisation of the free carbon population by the formation of TiC. Similarly steel two is initially stabilised via TiN, MnS and TiC (Figure 4.2). Steel two can be seen to follow the same stabilisation, with the remaining carbon being taken up through $VC_{0.88}$.formation.

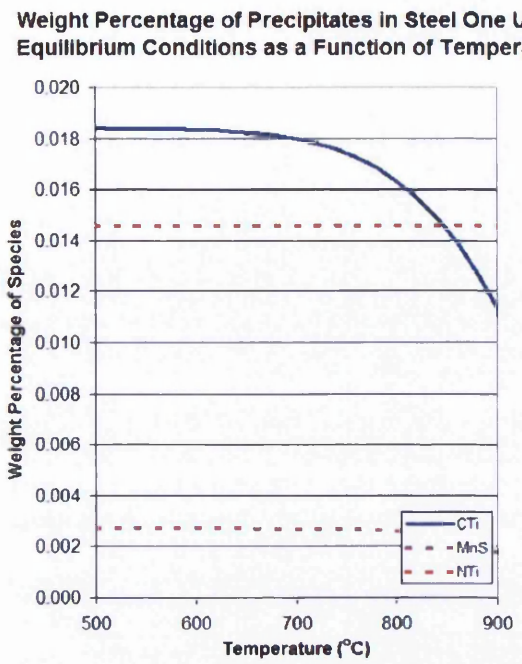

Figure 4.1 An MT-DATA plot of the weight percentage of precipitate species in Steel One (Ti Only) under equilibrium conditions, as a function of varying temperature.

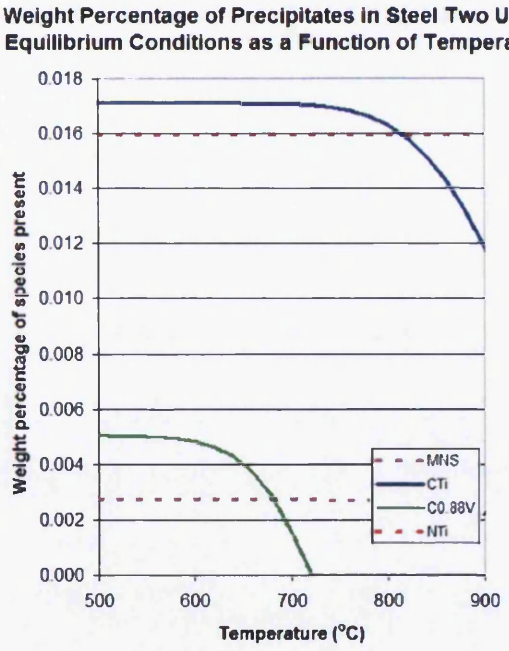

Figure 4.2 An MT-DATA plot of the weight percentage of precipitate species in Steel Two (Ti-V dual stabilised) under equilibrium conditions, as a function of varying temperature

Further plots have been made of the weight percentage of free carbon in solution under equilibrium conditions for the two steels to determine appropriate annealing conditions. The aim of the annealing exercise is to liberate a population of free interstitial carbon atoms in the range of 5-15wt.ppm (0.0005-0.0015wt.%) while ensuring complete recrystallization of the samples and comparable grain sizes. Figure 4.3 shows the level of free carbon in steel one to increase exponentially with increasing temperature as TiC is dissolved. From a fully stabilised condition the free carbon population rises to 14wt.ppm at 900°C.

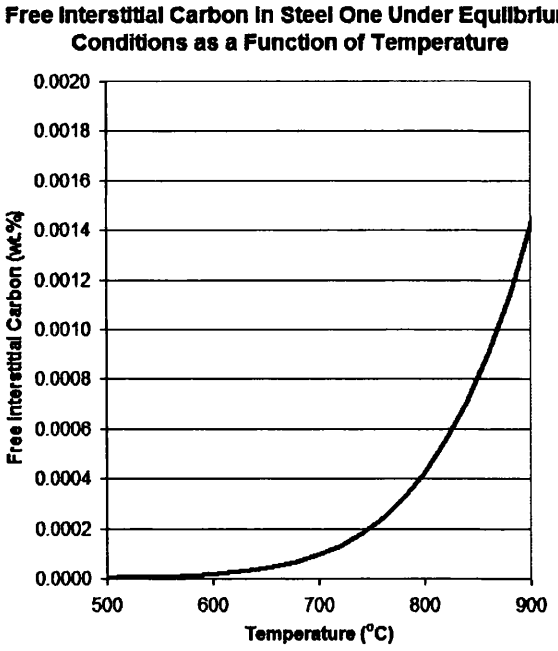

Figure 4.3 An MT-DATA plot of the variation in carbon in solution in ferrite in Steel One (Ti only) under equilibrium conditions as a function of varying temperature.

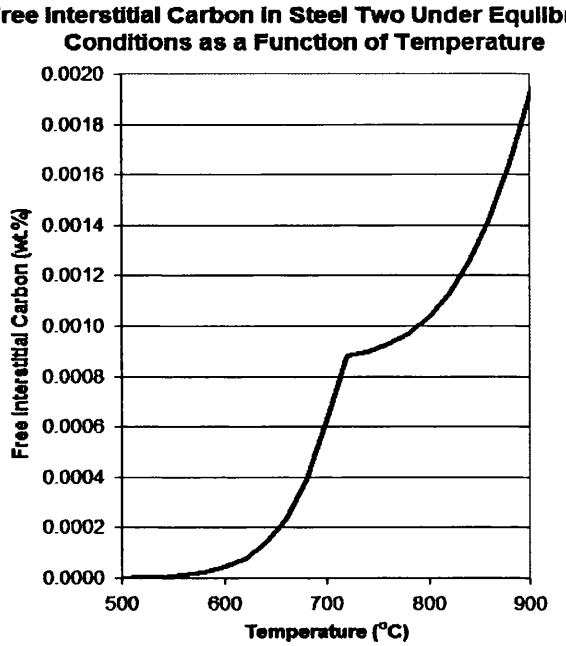

Figure 4.4 An MT-DATA plot of the variation in carbon in solution in ferrite in Steel Two (Ti-V dual stabilised) under equilibrium conditions as a function of varying temperature.

For steel two there is an initial rapid rise in free carbon population at relatively low temperatures due to the high solubility of vanadium carbide in ferrite relative to titanium carbide (Figure 4.4). By 720°C the $VC_{0.88}$ is expected to have fully dissolved, liberating 9wt.ppm of free carbon in solution; this value differs from that calculated numerically in section 4.1.1 as the numerical calculation assumes the preferential formation of TiS over MnS at low manganese levels, while MT-DATA assumes that manganese sulphide will form, resulting in a higher volume fraction of titanium carbide.

These plots have been used alongside the following recrystallization considerations to determine a suitable range of annealing conditions for the processing of the two experimental grades

4.3.2. Recrystallization considerations

The Larson-Miller parameter is usually used to extrapolate creep rupture data beyond the limits of practical laboratory testing, and takes the form:

$$P = T[C + \log t] \qquad 4\text{-}7$$

Where T is the absolute temperature (K) t the time (hrs), and C a constant. Creep is a thermally activated process, and the Larson Miller parameter is used to correlate the time to failure with absolute temperature at a constant engineering stress. As recrystallization is also a thermally activated process it can be treated similarly [93].

Work done by Gladman and Mitchell [93] has identified the Larson-Miller parameter (P) for a range of microalloyed steels, and specifically P*, the Larson Miller parameter at which recrystallization is complete. The alloy compositions used in this work are shown below. P* has also been determined for an ULC Ti-V chemistry in a more recent work by Ooi and Fourlaris [94].

The compositions used by Ooi and Fourlaris [94] and Gladman and Mitchel [93] are compared below with Steel Two (Table 2-1).

Table 4-2 Steel compositions used in experimental work by Ooi [16], Gladman[15] and the titanium vanadium composition to be used in the proposed work.

	C	Si	Mn	S	P	Ti	Nb	V	Al	N	P*
Gladman	0.007	0.01	0.21	0.003	0.005	0.019		0.08	0.028	0.0023	17800
Ooi	0.003			0.003		0.02	0.004	0.08		0.003	18300
Steel Two	0.004	0.007	0.094	0.004	0.008	0.025	0.001	0.085	0.009	0.0036	

The P* value for Mitchell's steel was 17800, and Ooi reported a value of around 18300. Given the strong similarity between Steel Two and the composition used by Ooi and Fourlaris it seems reasonable to assume that the P* value for this chemistry will be in the range 17000 to 19000, over which complete recrystallization is expected in under a minute at all temperatures above 750°C.

4.3.3. Validation of annealing conditions

Combining the results of the MT-DATA study with the recrystallization data a range of annealing conditions from 800°C to 880°C for steel one (Ti only) and 740°C to 860°C for steel two (Ti-V) were selected. For steel one this should give, under equilbrium conditions, a range of free carbon in solution varying from 4-12wt.ppm. For steel two the lower bound gives a higher than ideal free carbon value under equilibrium conditions (around 9wt.ppm). However, the recrystallization study suggests that a temperature of around 750°C is required to guaranteed complete recrystallization of the steel samples within a one minute soak period. This problem may be mitigated as, if there is trace niobium present in the steel (0.001wt.%), MT-DATA predicts a mixed vanadium rich vanadium/niobium carbide may form this having a reduced solubility (Figure 4.5). In this instance the equilibrium carbon in solution following annealing at 740°C would only be 6wt.ppm, the range of annealing conditions from 740°C to 860°C giving a range of free interstitial carbon populations from 6wt.ppm to 12wt.ppm, comparable with both steel one and the target range.

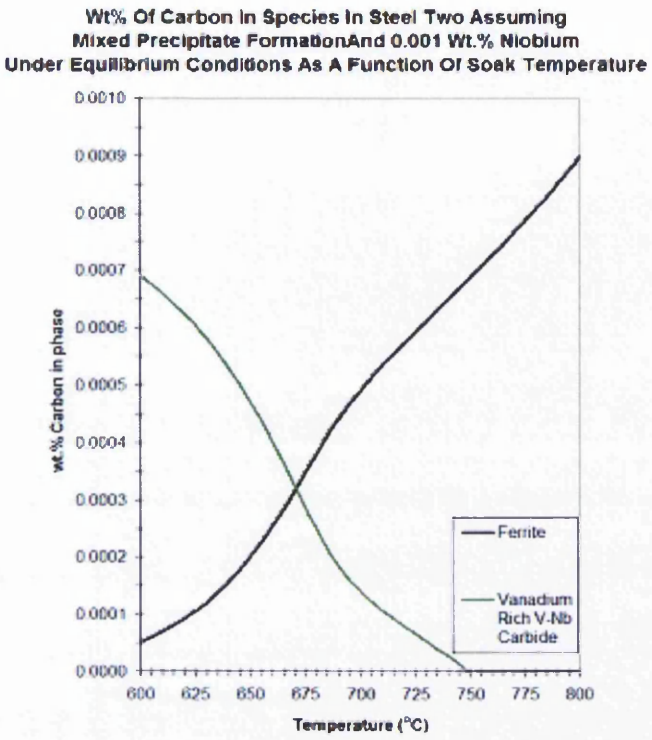

Figure 4.5 An MT-DATA plot of the weight percent of carbon contained in a mixed vanadium-niobium carbide, and in solution in ferrite, under equilibrium conditions as a function of temperature.

The annealing cycle was kept to a constant for both steels under all annealing conditions. The infrared furnace was ramped up to the soak temperature at a constant rate, sufficient to achieve the soak temperature within 30 seconds. The samples were then held at the soak temperature for one minute, and quenched with a 2000 litre/min stream of cold nitrogen gas. This gas quench gives initial cooling rates of 70°C/s, and was chosen to retain, as far as possible, the free carbon population in solution.

Following annealing it was necessary to determine the free interstitial carbon levels in the annealed steels by direct analysis using internal friction techniques as described in section 3.2. Duplicate tests were run on each sample, covering the full frequency spectrum from 0.001Hz through 10Hz.

Annealed samples were then mounted in resin, polished and etched in 2% nital. Grain size analysis was performed on the annealed samples using the Heyn's Linear intercept technique as described in section 3.5. Tensile and bake hardening properties were determined by pulling samples in triplicate.

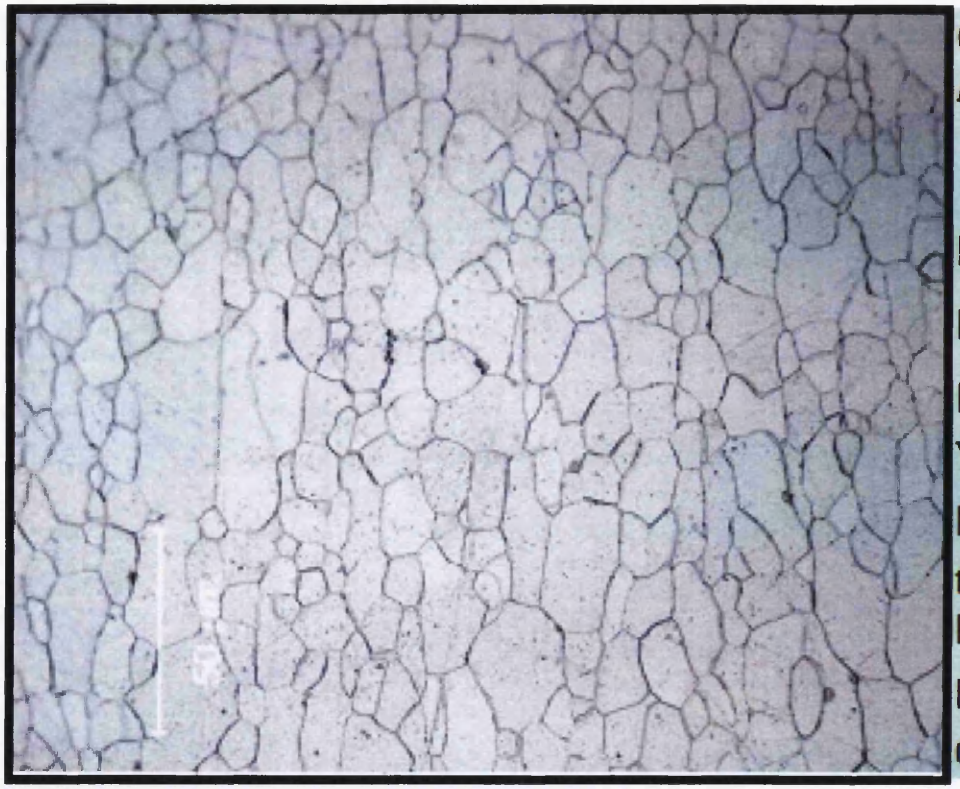

Grade	Ti only	
Annealling	45 second ramp 60 second soak 800 Rapid quench	
R_eH	237	MPa
R_eL	204	MPa
$R_{p0.2}$	211	MPa
YPE	4.4	%
R_m	290	MPa
total elong	26	%
Free Carbon	5.5	ppm
$BH_{5\%}$	29.8	MPa
Grain Size	10.3μm	

Figure 4.6 An optical micrograph of the grain structure of Steel One following annealing at 800°C, and its mechanical properties as established through accelerated aging tests.

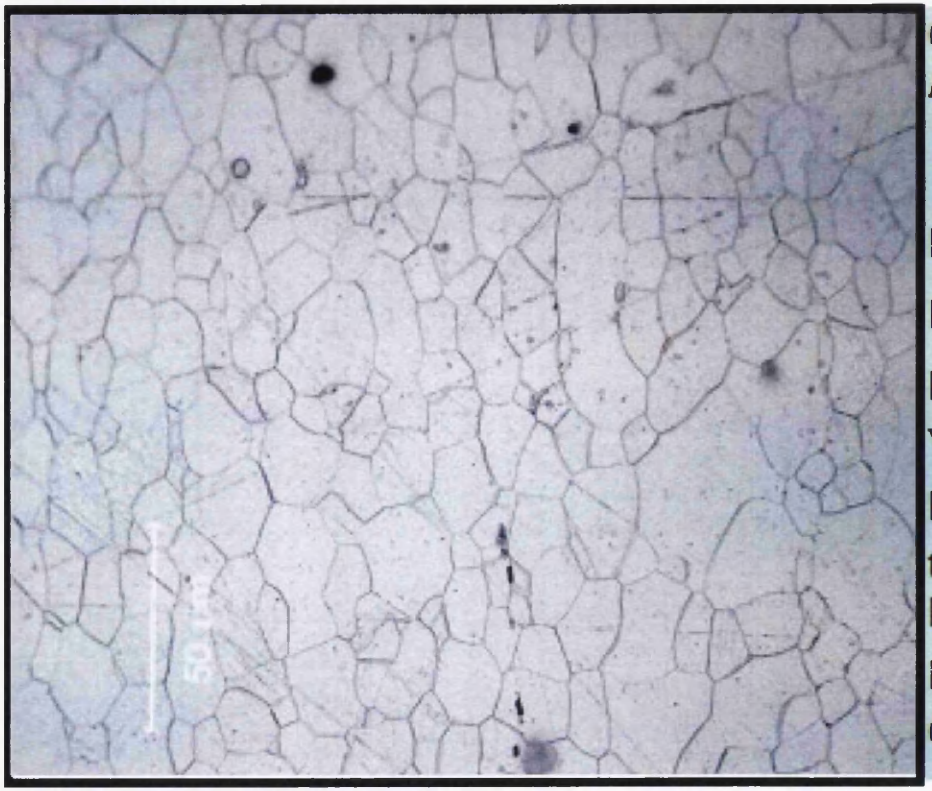

Grade	Ti only
Annealling	45 second ramp 60 second soak 880 Rapid quench
R_eH	212 MPa
R_eL	197 MPa
$R_{p0.2}$	192 MPa
YPE	2.6 %
R_m	285 MPa
total elong	24 %
Free Carbon	9.8 ppm
$BH_{5\%}$	32.5 MPa
Grain Size	11.5μm

Figure 4.7 An optical micrograph of the grain structure of Steel One following annealing at 880°C, and its mechanical properties as established through accelerated aging tests.

Grade	Ti-V	
Annealling	45 second ramp 60 second soak 740 Rapid quench	
R_eH	224	MPa
R_eL	182	MPa
$R_{p0.2}$	187	MPa
YPE	2.8	%
R_m	283	MPa
total elong	17	%
Free Carbon	4.7	ppm
$BH_{5\%}$	22.5MPa	
Grain Size	9.37μm	

Figure 4.8 An optical micrograph of the grain structure of Steel Two following annealing at 740°C, and its mechanical properties as established through accelerated aging tests.

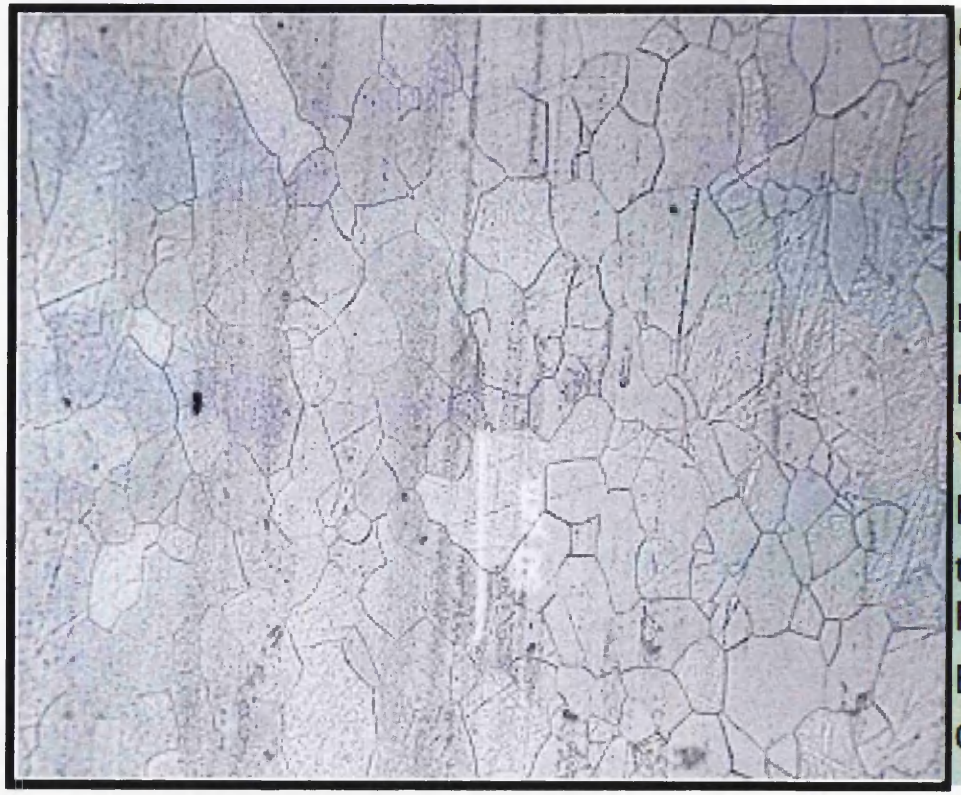

Grade	Ti-V	
Annealling	45 second ramp 60 second soak 860 Rapid quench	
R_eH	204	MPa
R_eL	173	MPa
$R_{p0.2}$	170	MPa
YPE	2.3	%
R_m	279	MPa
total elong	25	%
Free Carbon	8.0	ppm
$BH_{5\%}$	25.5MPa	
Grain Size	13.5μm	

Figure 4.9An optical micrograph of the grain structure of Steel Two following annealing at 860°C, and its mechanical properties as established through accelerated aging test

The titanium only steel shows a decreasing yield stress (204MPa-197MPa) and increasing grain size (10.3μm-11.5μm) as the annealing temperature is increased from 800°C to 880°C. The grain structure was equiaxed, showing full recrystallization to have occurred (Figure 4.6 Figure 4.7).

The dual stabilised steel also shows a decreasing yield stress (182MPa-173MPa) and increasing grain size (9.4μm-13.5μm) as the annealing temperature is increased from 740°C to 860°C. The grain structure is, again, equiaxed, showing full recrystallization to have occurred.(Figure 4.8 Figure 4.9)

Additional calibration of the inverse torsional pendulum was required for the generation of the free carbon results. Figure 4.10 and Figure 4.11 show the deconvolution of the Snöek peak. A linear background damping was removed from the raw data set, passing through the minimum points at the extreme ends of the trace, away from any expected peaks. A double Debye curve was then fitted to the data set using a least squares error formulation and the solver function in Microsoft Excel.

The double peak, described in section 3.1.2, was produced as the summation of two single peaks. The height and frequency of each of these peaks were fitted freely using the solving algorithm and a clear peak can be seen to have occurred in the vicinity of 0.1Hz in Figure 4.11 (the expected jump frequency for free carbon atoms in ferrite at room temperature)

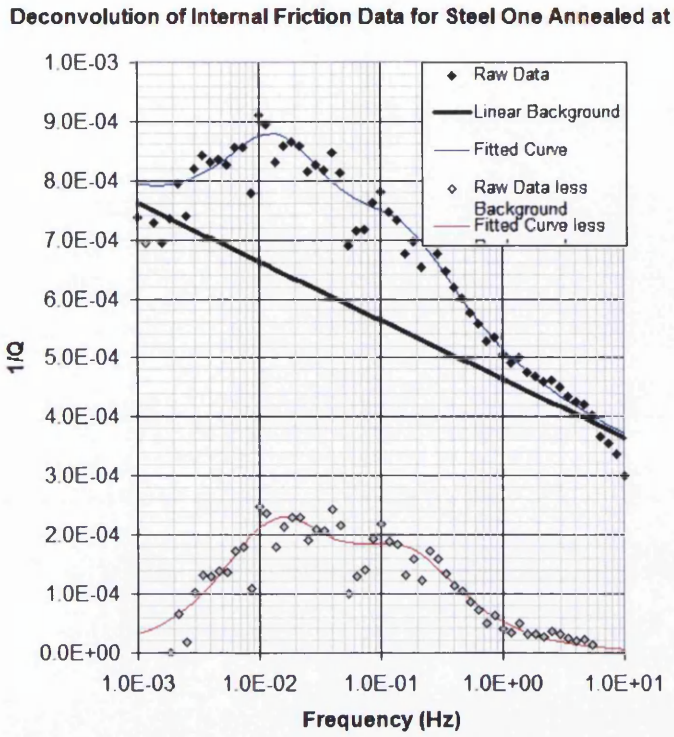

Figure 4.10 The deconvolution of internal friction data for the measurement of free interstitial carbon by fitting a double peak Debye curve and removal of linear background damping.

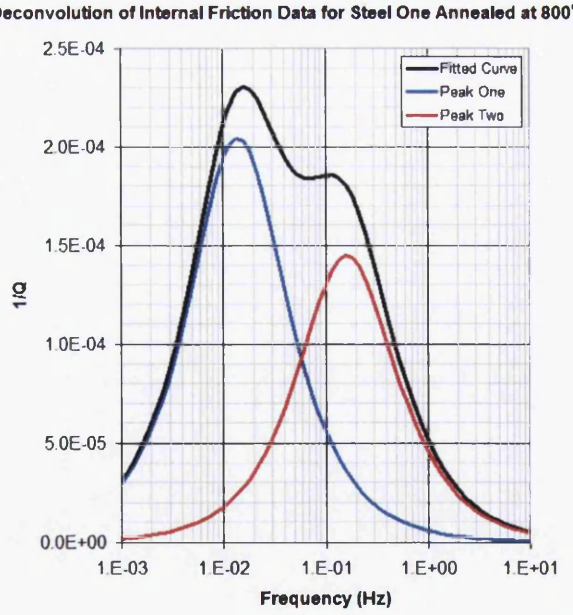

Figure 4.11 An illustration of how the double peak data produced during an internal friction test can be broken down into two discrete peaks to identify their height and frequency.

An additional peak, not found in the literature, was located in the vicinity of 0.02Hz in all samples tested within this programme of work. In order to isolate this peak as either an artefact produced by the torsional pendulum, or a feature of these samples, previous test data generated from ten tests covering a range of commercial Corus steel chemistries were refitted (Figure 4.13). Additionally the samples used in this investigation were sent to the Centre Research de Mettallurgie (CRM) in Belgium for retesting using an equivalent Vibran torsional pendulum under the same testing regime.

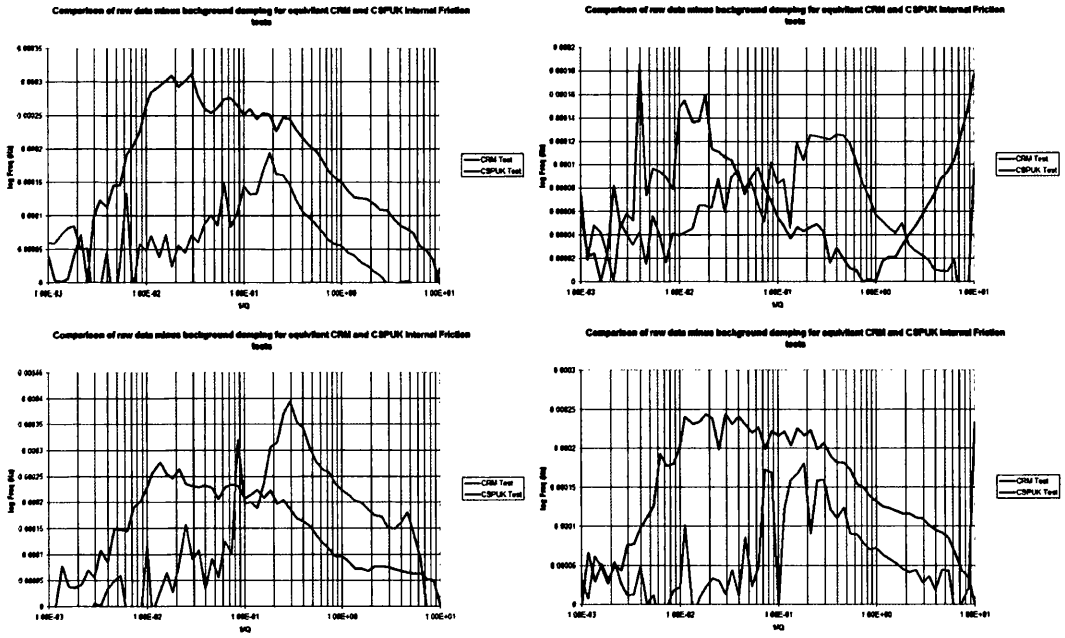

Figure 4.12 A direct comparison of normalised internal friction data produced at CRM in Holland (red) and ECM^2 in South Wales (Green) on equivalent Vibran torsional pendulums, highlighting the presence of a double peak in the ECM^2 data.

The retests at CRM (Figure 4.12) do not show any peak in the region of 0.02Hz. Data from previous Corus tests containing 5-100wt.ppm of free carbon in solution

were refitted using a double Debye type curve, and the location of this secondary peak detected in all instances with a similar frequency and intensity (Table 4-3). It was concluded that a secondary peak, occurring in the vicinity of 0.02Hz with an intensity of approximately $4x10^{-4}$ is an artefact produced by the in house Vibran Torsional pendulum and can safely be ignored.

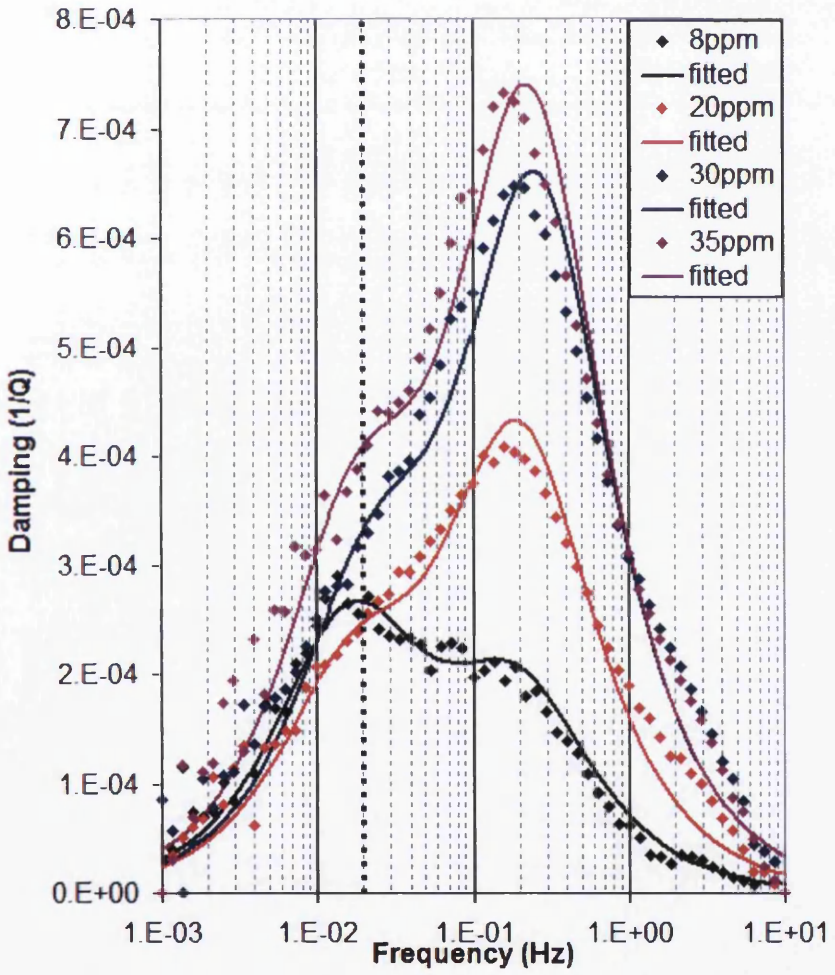

Figure 4.13 Double peak curve fits from Corus commercial steel chemistries showing the presence of the $2x10^{-2}$ Hz peak across a range of compositions and free carbon levels.

Table 4-3 Internal friction results for various steels tested at the ECM² RD&T facility in Port Talbot

Sample Designation	Peak Position (Hz)	Peak Height
6062601	1.67E-02	1.69E-04
6022704	1.78E-02	2.92E-04
6062804	2.19E-02	2.39E-04
6062703	3.38E-02	1.47E-04
6062702	4.40E-02	1.80E-04
6070302	2.11E-02	1.99E-04
6070303	1.95E-02	2.78E-04
6070402	1.62E-02	2.39E-04
6070301	1.75E-02	1.28E-04
6070401	2.00E-02	1.67E-04
6063002	1.75E-02	1.19E-04
Average	**2.24E-02**	**1.96E-04**

The final levels of free interstitial carbon detected via internal friction testing (table) cover a range for the titanium only steel of 5.5wt.ppm to 9.8wt.ppm, and for the titanium vanadium dual stabilised steel 4.7wt.ppm to 8.0wt.ppm. For both steels these ranges are similar to those predicted using MT-DATA thermodynamic modelling software, though the value of 8wt.ppm for the titanium-vanadium dual stabilised steel is somewhat lower than 12wt.ppm predicted. It seems that MT-DATA can be used as a useful tool in developing processing programmes for experimentation, if the processing conditions are designed to approach equilibrium conditions in the test coupons.

CHAPTER FIVE

EXPERIMENTAL PROGRAM

5. GENERATION OF MODEL VALIDATION DATA

For a model to have real value, beyond an academic demonstration of a technique, it is necessary that it be rigorously validated. The initial stages of the modelling work performed within this doctorate have been validated against published data from several other authors' papers [25, 40, 95]. In addition to this a targeted programme of experimentation has been developed to generate validation data covering a range of temperatures, carbon contents, and the effect of secondary alloying species on the rates of strain aging.

This experimental programme also serves to highlight and quantify the retarding effect of vanadium microalloying additions on rates of strain aging in ultra low carbon steels.

Experiment one generates 100°C aging curves for the two experimental steels under investigation, and provides isochronal comparisons of the aging response to show the retarding effect of vanadium. Two annealing conditions are covered for each grade, allowing variations in carbon content to be considered.

Experiment two serves to generate activation energies and aging kinetics for the dislocation locking process in the two steels. In achieving this partial aging curves are developed at temperatures of 50, 60, 70,80 and 90°C allowing the functionality of the computer model to be assessed over a range of aging temperatures thus ensuring its robustness.

5.1. Experiment one: Comparison of accelerated aging profiles

Accepting that vanadium has a retarding effect on rates of strain aging in ultra low carbon strip steels, it would be expected that accelerated aging profiles for two steels with otherwise equivalent compositions would differ given a significant alloy addition of vanadium to one of them.

A direct comparison of accelerated aging profiles would require that the two grades under consideration contain the same amount of free interstitial carbon atoms. Modelling alloy stabilisation in terms of composition is relatively rapid, and easy, using thermodynamic modelling software such as MT-DATA. However, such predictions describe the equilibrium composition and precipitate weight fractions. While these can be used as a guideline in developing annealing cycles, they cannot be used to guarantee quantities of species in solution or precipitates. As such it is necessary to use an indirect method of comparison for the accelerated aging profiles.

By varying the annealing cycle, different levels of free carbon can be released into solution for a given fully stabilised steel composition, through the dissolution of carbides. If the steel samples containing differing carbon levels are then subjected to the same aging treatment (for instance furnace aging at 100°C) they will exhibit different aging responses as a result of the free carbon levels.

By considering the aging response developed over a given time scale it is possible to develop isochronal plots, that show the aging response of a given steel at a set soak

time and temperature as a function of its carbon composition. If two steels exhibit the same aging properties, their isochronal plots would be expected to share a common line; if the aging response of one of the two steels is retarded due to alloying additions or treatment, the isochronal plots for the two would be expected to deviate from one another.

The aim of this experiment was to develop isochronal aging plots for Steel One (Ti only) and Steel Two (Ti-V dual stabilised) over similar levels of free carbon, and highlight any retarding effect that exists.

5.1.1. Derivation of isochronal aging plots

Following annealing and the validation of the selected annealing conditions accelerated aging profiles were developed for the two steels. Annealed samples were prestrained by 5% as described in section 3.3 then aged in a furnace at 100°C for 2,5,10,50,100 and 500 minutes. Triplicate samples were aged and plots made of aging response as a function of time. Three curve fits were applied to the data sets and fitted to minimise the root mean squared error.

5.1.1.1. Johnson-Mehl-Avrami-Kolmogorov

The Johnson-Mehl-Avrami-Kolmogorov (JMAK) equation can be used to model a number of kinetic phenomena, but is traditionally applied to data sets relating to nucleation and recrystallization studies [96-98] It takes the general form:

$$f_t = 1 - \exp(kt^n) \qquad 5\text{-}1$$

Where f_t (%) is the fraction recrystallized/transformed after a time t (s), k a temperature dependant parameter describing the process and n constant, typically in the range 1-4. Considering the formation of Cottrell atmospheres as a nucleation type event, a logarithmic decrease in locking rate would be expected, as with nucleation, as available sites are expended and the bulk of the material is transformed, or the bulk of dislocations have been locked. Normalising the result to the maximum increase in yield stress attributable to dislocation locking (the lesser of 35MPa, and the maximum yield stress increase achieved during an accelerated aging) gives the equation:

$$\sigma = \sigma_m\left(1 - \exp\left(kt^n\right)\right) \qquad 5\text{-}2$$

Where σ is the yield stress increase (Mpa) after a time, t (s), σ_m the maximum yield stress increase achievable (Mpa), k an arrhenius variable and n the kinetic exponent, assumed to be 0.66 in line with locking theory and results produced by De et al for the formation of Cottrell atmospheres [36].

5.1.1.2. Elsen and Hougardy

Aging curves were also modelled using the descriptive equation produced by Elsen and Hougardy [25]

$$\Delta\sigma_{BH(t)} = \Delta\sigma_{MAX-1}\frac{\left(\frac{t}{k_c}\right)^{n_c}}{1+\left(\frac{t}{k_c}\right)^{n_c}} \qquad 5\text{-}3$$

In which k_c is a temperature dependant parameter following an Arrhenius type relationship, $\Delta\sigma_{MAX-I}$ is the maximum strength that can be achieved through Cottrell locking and n_c a constant (roughly 0.9); both of these parameters are independent of both temperature and prestrain.

The maximum aging response for each grade attributable to dislocation locking, rather than precipitate nucleation, was again taken as the lesser of 35MPa and of the aging response following 500 minutes of isothermal aging at 100°C.

5.1.1.3. The Logistic Equation

$$P(t) = a\frac{1 + m\exp^{-t/r}}{1 + n\exp^{-t/r}} \qquad 5\text{-}4$$

The logistic function can be used to model the sigmoidal growth curve of self-limiting populations through special cases such as the Verhulst equation for population dynamics [99]. It was used as a comparative basis for the other functions in this exercise as it makes no assumptions about the meaning or values of the data, and will merely provide a best-fit sigmoid curve through the data presented. Within this fitting exercise a,m,n and r were fitted as dimensionless constants, to produce a value as a function of t, the aging time in seconds.

These characteristics were compared to determine whether any retarding effect from the vanadium addition could be observed.

5.1.2. Experiment one results

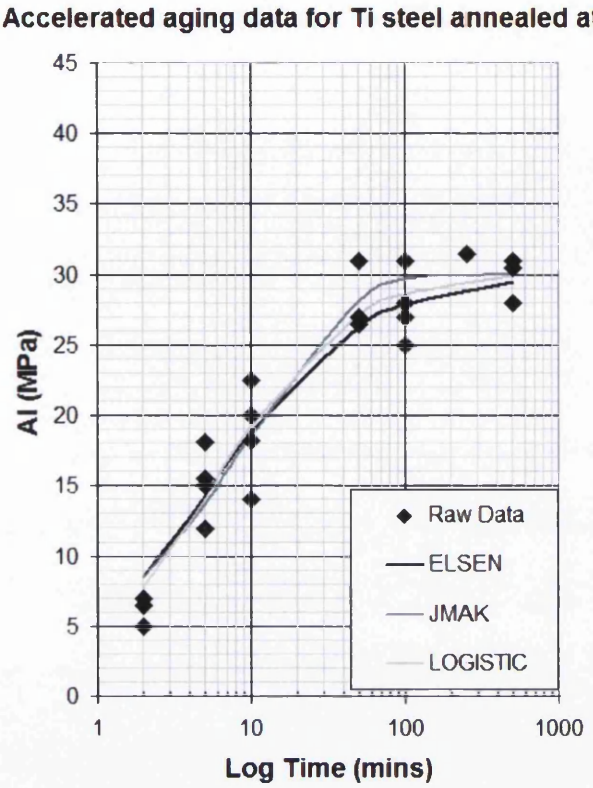

Figure 5.1 Accelerated aging data for steel one (Ti only) aged at 100°C following 800°C annealing to contain 5.5wt.ppm free interstitial carbon. Fitted using Elsen and Hougardy's equations (black), the JMAK equation (Grey) and the logistic equation (light grey)

Figure 5.1 shows fits of the Elsen and Hougardy, Johnson-Mehl-Avrami-Kolmogorov and Logistic equation to raw aging data produced for the titanium only steel following annealing at 800°C, and containing 5.5wt.ppm of free carbon. All three curve fits match the data well in the range 5MPa-20MPa. The JMAK equation begins to plateau after 60 minutes, achieving the maximum value of 30MPa after 100 minutes. The logistic equation and Elsen and Hougardy's equation show a more gradual rise, only achieving the maximum value of 30MPa after 500 minutes and, at this point, having yet to stabilise. The maximum aging response in the raw data is 32MPa

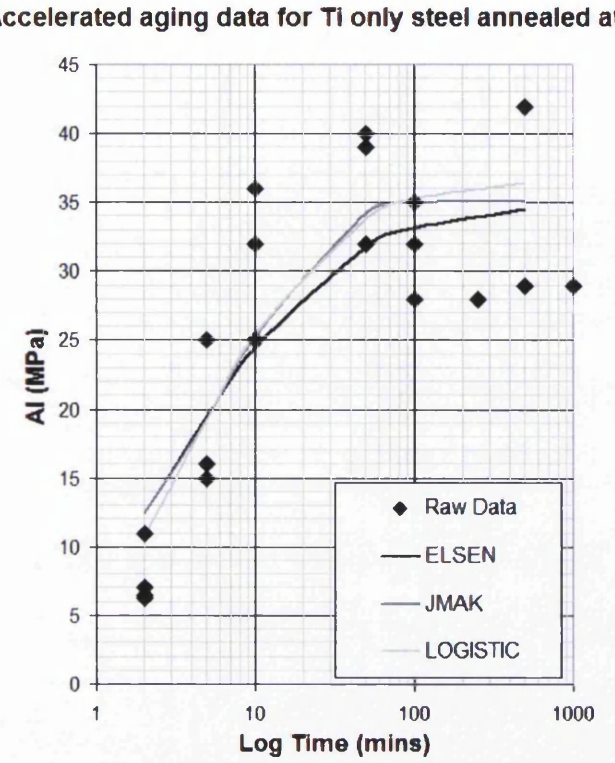

Figure 5.2 Accelerated aging data for steel one (Ti only) aged at 100°C following 880°C annealing to contain 9.8wt.ppm free interstitial carbon. Fitted using Elsen and Hougardy's equations (black), the JMAK equation (Grey) and the logistic equation (light grey)

Figure 5.2 shows fits of the Elsen and Hougardy, JMAK and Logistic equations to raw aging data produced for the titanium only steel following annealing at 880°C, and containing 9.8wt.ppm of free carbon. All three curve fits over predict the data set in the initial minutes of aging and under predict the data set in the range 20MPa-35MPa. The JMAK equation begins to plateau after 60 minutes, achieving a maximum value of 35MPa after 80 minutes. The logistic equation over predicts the final aging, and both the Elsen and Hougardy equation and logistic equation have yet to plateau after 500 minutes. The scatter in the raw data increases with increasing time, maximum aging responses after 500 minutes varying between 28 and 42MPa.

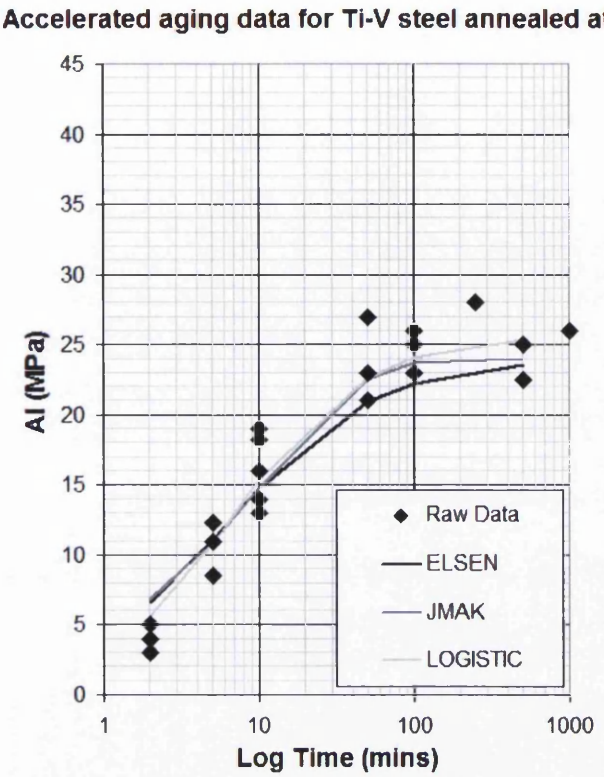

Figure 5.3 Accelerated aging data for steel two (Ti-V dual stabilised) aged at 100°C following 740°C annealing to contain 4wt.ppm free interstitial carbon. Fitted using Elsen and Hougardy's equations (black), the JMAK equation (Grey) and the logistic equation (light grey)

Figure 5.3 shows fits of the Elsen and Hougardy, Johnson-Mehl-Avrami-Kolmogorov and Logistic equation to raw aging data produced for the titanium-vanadium dual stabilised steel following annealing at 740°C, and containing 4.7wt.ppm of free carbon. The Elsen and Hougardy equation appears to under predict the aging toward longer times, following the bottom set of the raw aging data. The JMAK equation begins to plateau after 60 minutes, achieving the maximum value of 24MPa after 100 minutes. The logistic equation over predicts the final aging, and both the Elsen and Hougardy equation and logistic equation have yet to plateau after 500 minutes.

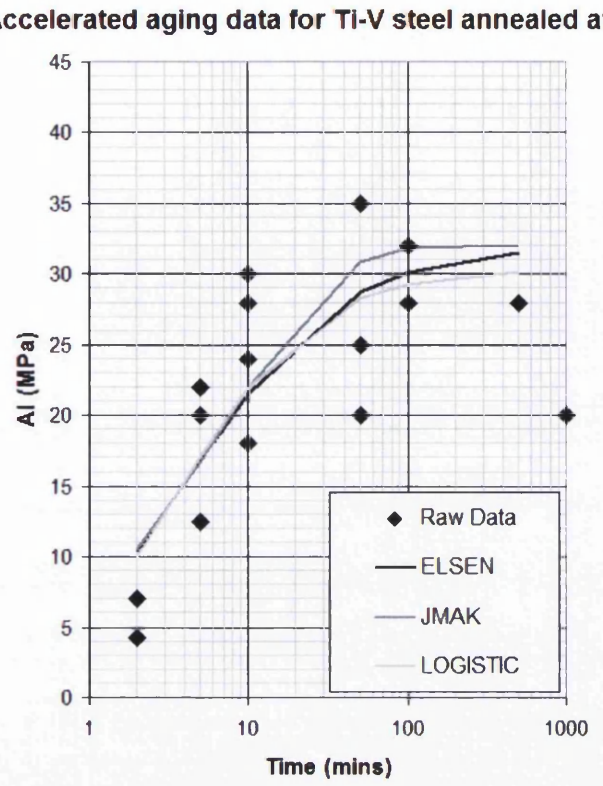

Figure 5.4 Accelerated aging data for steel two (Ti-V dual stabilised) aged at 100°C following 860°C annealing to contain 8wt.ppm free interstitial carbon. Fitted using Elsen and Hougardy's equations (black), the JMAK equation (Grey) and the logistic equation (light grey)

Figure 5.4 shows fits of the Elsen and Hougardy, Johnson-Mehl-Avrami-Kolmogorov and Logistic equation to raw aging data produced for the titanium-vanadium dual stabilised steel following annealing at 860°C, and containing 8wt.ppm of free carbon. The Elsen and Hougardy equation appears to under predict the aging toward longer times, following the bottom set of the raw aging data. The JMAK equation has reached a plateau by 100 minutes achieving the maximum value of 32MPa. The Elsen and Hougardy equation and logistic equation both have yet to plateau after 1000 minutes.

Table 5-1 Root Mean Squared error for the Elsen and Hougardy equation, JMAK equation and logistic equation fitted to experimental aging data

	Ti		Ti-V		Mean RMS Error in
	800	880	740	860	Curve Fits
ELSEN	1.18	3.64	1.88	2.88	2.395
JMAK	1.27	3.21	1.38	3.28	2.285
LOGISTIC	0.82	2.77	1	2.31	1.725

Table 5-1 shows the sum of the root mean square error of the curve fits performed for each of the annealing conditions, when compared to the mean of the raw aging data. In all three instances the RMS error is significantly higher for the titanium only steel annealed at 880°C and the titanium-vanadium dual stabilised steel annealed at 860°C, where the scatter in the raw data was greatest. The logistic equation, used as a control, gives the best-fit to the raw data. The quality of fits produced by the Elsen and Hougardy equation and JMAK equation are numerically comparable, but from Figure 5.1 to Figure 5.4 the JMAK equation produces a more well defined plateau.

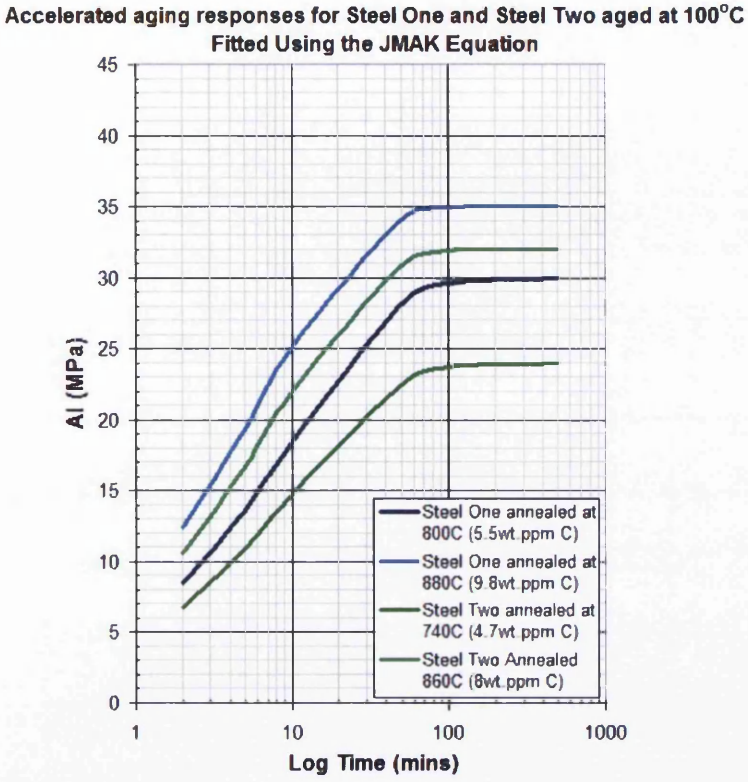

Figure 5.5 Johnson-Mehl-Avrami-Kolmogorov fits of the 100°C aging response of steels one and two across a range of annealing conditions, used in the derivation of isochronal aging plots.

Figure 5.5 shows the construction used for the derivation of the isochronal plots, used in the direct comparison of the two steel grades. The plotted lines are fits of the JMAK equation to the mean aging data presented in Figure 5.1 to Figure 5.4, adjusted for the maximum aging response obtained experimentally.

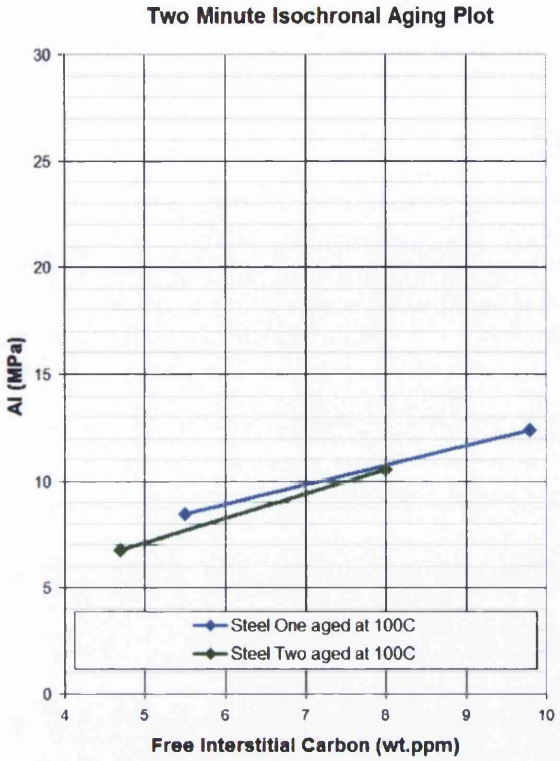

Figure 5.6 A comparison of the isochronal aging response, after two minutes, of Steel One (Ti Only) and Steel Two (Ti-V dual stabilised) as a function of varying carbon content.

Figure 5.6 shows a constructed isochronal plot comparing the aging response of the titanium only steel chemistry with the titanium-vanadium steel chemistry as a function of free interstitial carbon content after an aging treatment of two minutes at 100°C.

The aging response of the Ti only steel, taken from a JMAK fit to the mean aging response, increases from 8.4MPa to 12.2MPa as the carbon FICA content increases from 5.5wt.ppm to 9.8wt.ppm.

The aging response of the Ti-V steel, similarly derived, increases from 6.8MPa to 10.5MPa as the FICA content increases from 4.7wt.ppm to 8wt.ppm. A linear

variation in aging response has been assumed with increasing carbon content for both grades, and the line representing the Ti-V steel is below that for the Ti only steel up to approximately 8wt.ppm free carbon, at which level the lines meet. The difference in aging response is greater at lower carbon levels reaching a maximum value of around 10% at 5.5wt.ppm free carbon; an extrapolation of the two lines would lead to a greater difference at even lower carbon levels.

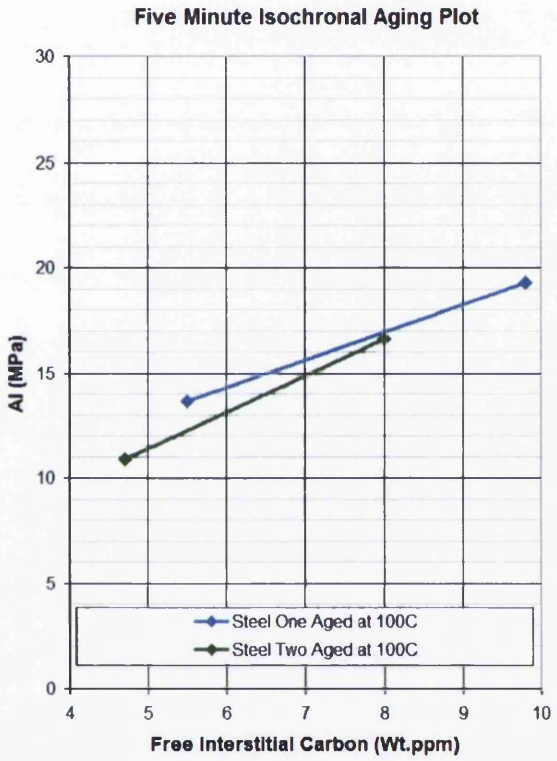

Figure 5.7 A comparison of the isochronal aging response, after five minutes, of Steel One (Ti Only) and Steel Two (Ti-V dual stabilised) as a function of varying carbon content.

Figure 5.7 shows a constructed isochronal plot comparing the aging response of the titanium only steel chemistry with the titanium-vanadium steel chemistry as a function of free interstitial carbon content after an aging treatment of five minutes at 100°C.

The aging response of the Ti only steel, taken from a JMAK fit to the mean aging response, increases from 14.8MPa to 19.2MPa as the carbon FICA content increases from 5.5wt.ppm to 9.8wt.ppm.

The aging response of the Ti-V steel, similarly derived, increases from 10.9MPa to 15.5MPa as the FICA content increases from 4.7wt.ppm to 8wt.ppm. The linear fits predicting aging response with free carbon would be expected to converge at 8.5wt.ppm free carbon. The difference in aging response is again greater at lower carbon levels, reaching a maximum value of around 10% at 5.5wt.ppm free carbon; an extrapolation of the two lines would lead to a greater difference at even lower carbon levels.

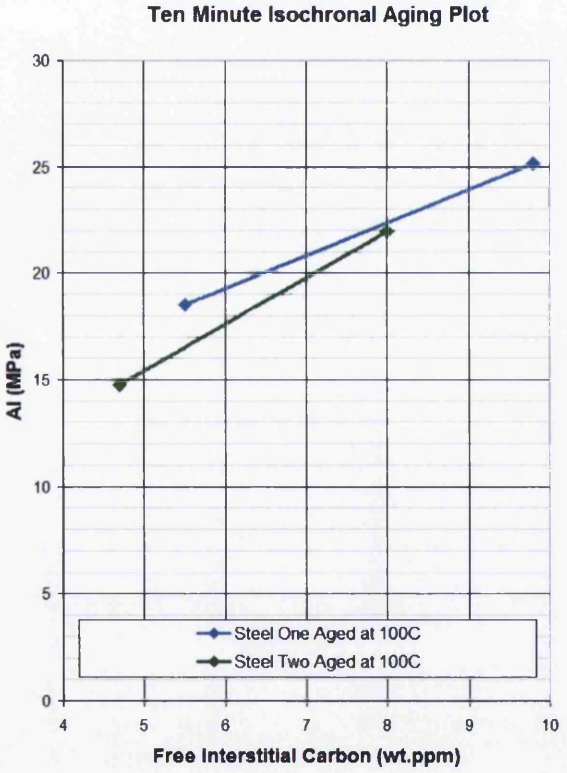

Figure 5.8 A comparison of the isochronal aging response, after ten minutes, of Steel One (Ti Only) and Steel Two (Ti-V dual stabilised) as a function of varying carbon content.

Figure 5.8 shows a constructed isochronal plot comparing the aging response of the titanium only steel chemistry with the titanium-vanadium steel chemistry as a function of free interstitial carbon content after an aging treatment of ten minutes at 100°C.

The aging response of the Ti only steel, taken from a JMAK fit to the mean aging response, increases from 18.5MPa to 25MPa as the carbon FICA content increases from 5.5wt.ppm to 9.8wt.ppm.

The aging response of the Ti-V steel, similarly derived, increases from 14.9MPa to 22MPa as the FICA content increases from 4.7wt.ppm to 8wt.ppm. The linear fits predicting aging response with free carbon would be expected to converge at 8.5wt.ppm free carbon. The difference in aging response is again greater at lower carbon levels, reaching a maximum value of around 10% at 5.5wt.ppm free carbon; an extrapolation of the two lines would lead to a greater difference at even lower carbon levels.

5.2. Experiment two: Determination of activation energies for aging

Following the work of Rashid in 1970s using HSLA steels [14, 15], it is possible to model strain aging using an Arrhenius equation, and thus derive the activation energy for the process. As strain aging is diffusion dependant, it is a thermally activated process, and would be expected to follow an equation of the type:

$$t_{AI} = A\exp\left(\frac{Q}{RT}\right) \qquad 5\text{-}6$$

Where t_{AI} (s) is the time required to attain the aging response AI (MPa) at a temperature T(K), Q is the activation energy of the process ($kJmol^{-1}$), A a constant and R the gas constant ($8.3145JK^{-1}mol^{-1}$) . Equation [5-6] can be rearranged as:

$$\frac{t_{AI}}{A} = \exp\left(\frac{Q}{RT}\right) \qquad 5\text{-}7$$

$$\ln\left(\frac{t_{AI}}{A}\right) = \frac{Q}{RT} \qquad 5\text{-}8$$

$$\ln\left(t_{AI}\right) = \frac{Q}{RT} + \ln(A) \qquad 5\text{-}9$$

It follows that accelerated aging trials can be performed over a range of temperatures, and the time required to achieve an equivalent aging response compared on a plot of $\ln(t_{Al})$ vs 1/RT, for which the result should be a straight line of gradient Q and Y axis intercept ln(A).

Approximate times that could be expected to yield an equivalent aging response were calculated using Hundy's equation for equivalency, with an assumed activation energy of $82kJmol^{-1}$ [57]

The aging data was fitted using both unconstrained fits, with no imposed conditions on the parameters, and constrained fits of the JMAK equation, in which it was assumed that the activation energy values were the same across the process, and all temperature related effects were accounted for in the Arrhenious type parameter.

Samples of the Ti only steel were annealed at 880°C to liberate a controlled free carbon population of 9.8wt.ppm into solution. Samples of the TiV steel were annealed at 860°C to liberate a population of free interstitial carbon atoms of 8wt.ppm. Accelerated aging was then performed at temperatures of 50°C, 60°C, 70°C, 80°C and 90°C for comparison with the existing 100°C data. Tensiles were initially pulled in duplicate, with additional samples added to populate the graph where scatter was high. Curve fitting was attained using a least squares minimisation of error.

5.2.1. Experiment two results

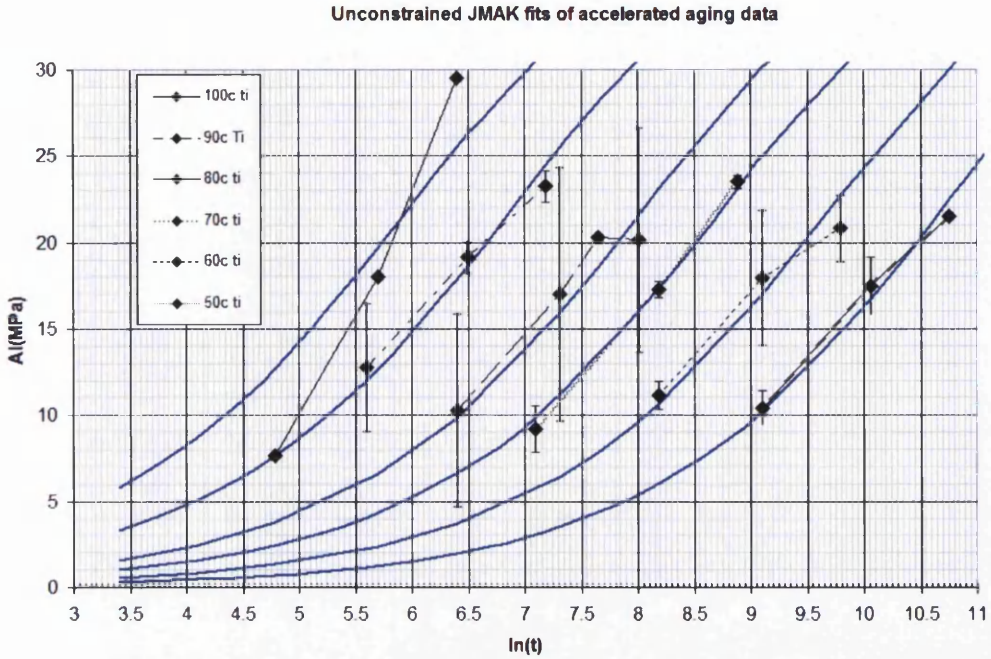

Figure 5.9 Partial aging plots developed for steel one (Ti only) following annealing at 880°C, aged over the temperature range 50°C to 100°C and fitted using the JMAK equation

Figure 5.9 shows a good match between the JMAK plots produced assuming a kinetic exponent of 0.66 with an unconstrained activation energy, and the raw data produced by accelerated aging over the temperature range 50°C to 100°C of the Ti only steel annealed at 880°C, containing 9.8wt.ppm free interstitial carbon. In all instances the fitted curves fall within the level of scatter observed within the actual experimental data. The aging response achieved is greatest at 100°C, reaching a maximum of 30MPa; the aging response is lower at lower temperatures, for times assumed equivalent by Hundy's equation, with aging responses of 23MPa, 20MPa, 23.5MPa, 21MPa and 20.5MPa at 90°C, 80°C, 70°C, 60°C and 50°C respectively.

The fits displaying the largest difference between the measured data and the applied curve fits are achieved at temperatures of 80°C and 100°C, and the greatest degree of scatter is found in the raw data at 80°C, coincident with the poor fit.

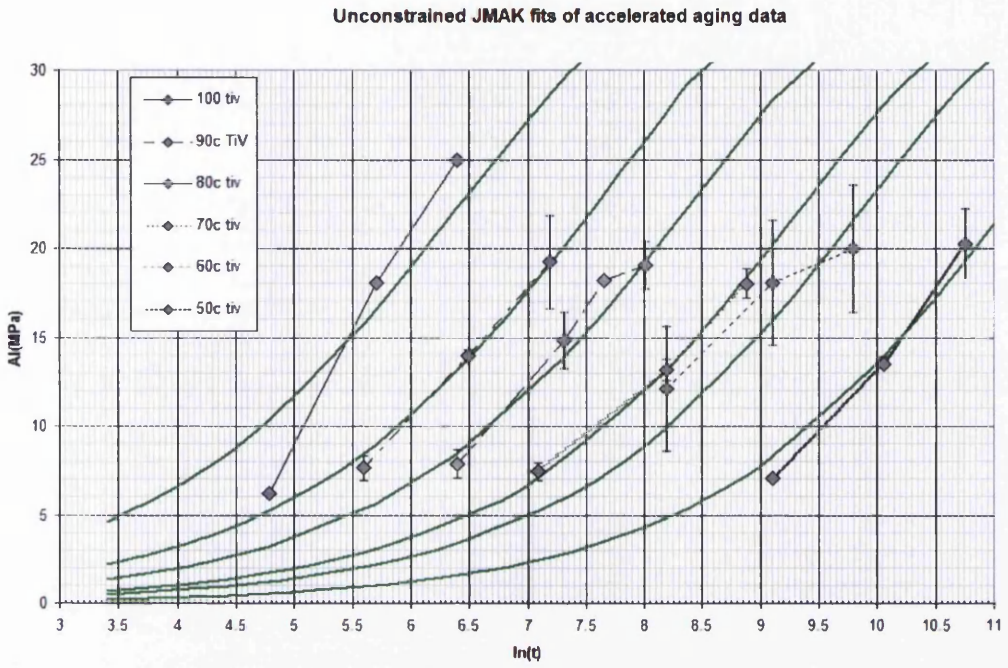

Figure 5.10 Partial aging plots developed for steel two (Ti-V dual stabilised) following annealing at 860°C, aged over the temperature range 50°C to 100°C fitted using the JMAK equation

Figure 5.10 shows a close match between the JMAK plots produced assuming a kinetic exponent of 0.66 with an unconstrained activation energy, and the raw data produced by accelerated aging over the temperature range 50°C to 100°C of the Ti-V steel following annealing at 860°C and containing 8wt.ppm free interstitial carbon. The aging response achieved is greatest at 100°C, reaching a maximum of 25MPa; the aging response is lower at lower temperatures, for times assumed equivalent by

Hundy's equation, with aging responses of 19MPa, 19MPa, 18MPa, 20MPa and 20MPa at 90°C, 80°C, 70°C, 60°C and 50°C respectively.

The worst fits are achieved at temperatures of 60°C and 100°C, and the greatest degree of scatter is found in the raw data at 60°C, coincident with the poor fit.

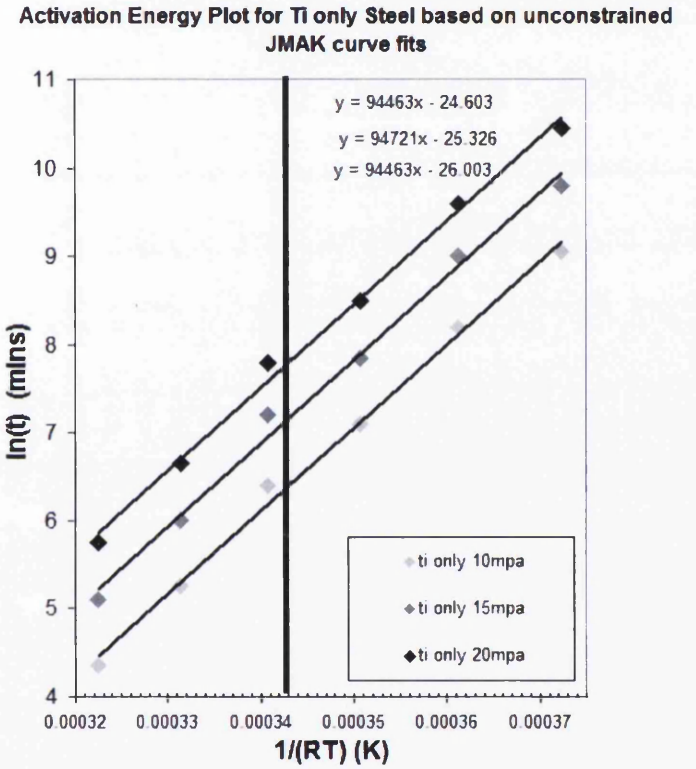

Figure 5.11 Derived Arrhenius activation energy for Steel One (Ti Only). Data taken from Figure 5.9

Figure 5.11 shows the derivation of the Arrhenius constants describing thermally activated strain aging for the Ti only steel, using data from fitted curves in

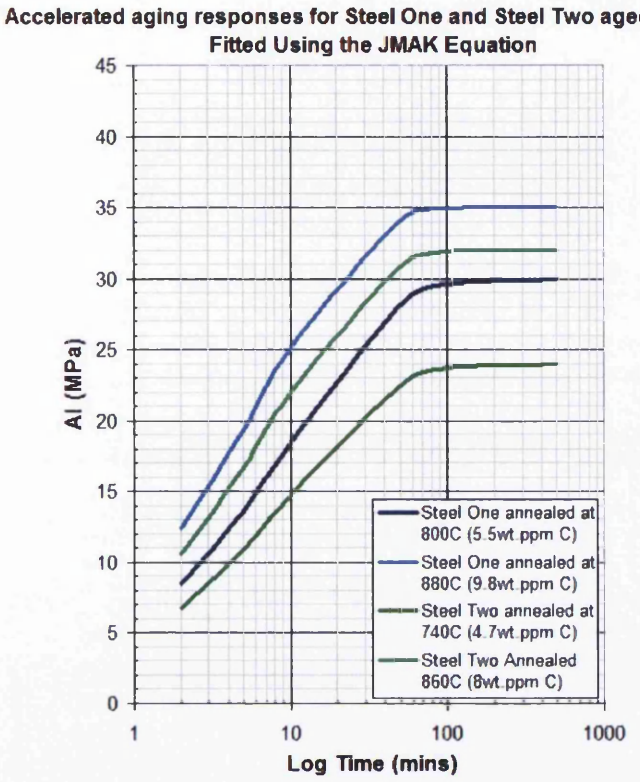

Figure **5.5** Best-fit straight lines show a good match to the experimental results for data taken at 10MPa, 15MPa and 20MPa. The average activation energy for the process is approximately 94.5kJmol^{-1}, with a pre-exponential coefficient of 1e-11. No inflection point is observed at 77°C (1/RT=0.000343)

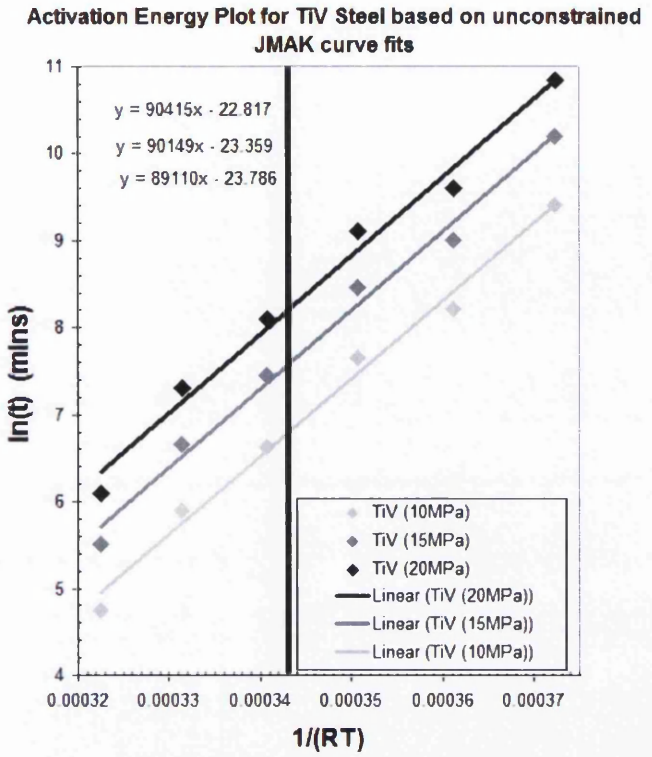

Figure 5.12 Derived Arrhenius activation energy for Steel One (Ti Only).

Figure 5.12 shows the derivation of the Arrhenius constants describing thermally activated strain aging for the Ti-V dual stabilised steel, using data from fitted curves in . Best-fit straight lines show a good match to the experimental results for data taken at 10MPa, 15MPa and 20MPa. The average activation energy for the process is approximately 89.9kJmol^{-1}, with a pre-exponential coefficient of 7.5e-11. No inflection point is observed at 77°C (1/RT=0.000343)

5.2.2. Determination of the JMAK aging kinetics

Following activation energy determination, aging kinetics were calculated from the raw data assuming the JMAK equation gives a representative fit of the raw data. The JMAK equation can be re-arranged as follows:

$$\sigma = \sigma_m\left(1-\exp\left(kt^n\right)\right) \qquad 5\text{-}10$$

$$1-\frac{\sigma}{\sigma_m} = \exp\left(kt^n\right) \qquad 5\text{-}11$$

$$\ln\left(1-\frac{\sigma}{\sigma_m}\right) = kt^n \qquad 5\text{-}12$$

$$-\ln\left(1-\frac{\sigma}{\sigma_m}\right) = -kt^n \qquad 5\text{-}13$$

$$\ln\left(-\ln\left(1-\frac{\sigma}{\sigma_m}\right)\right) = n\ln t - \ln k \qquad 5\text{-}14$$

It follows that a plot of $\ln(-\ln(1-\frac{\sigma}{\sigma_m}))$ vs. ln(time) will give a straight line having a gradient equal to the kinetic exponent of the process.

Figure 5.13shows the aging kinetics for the Ti only steel annealed at 880°C and aged over the temperature range 50°C to 100°C, as determined from the JMAK equation. Discounting the 100°C measurement the average kinetic exponent is 0.614.

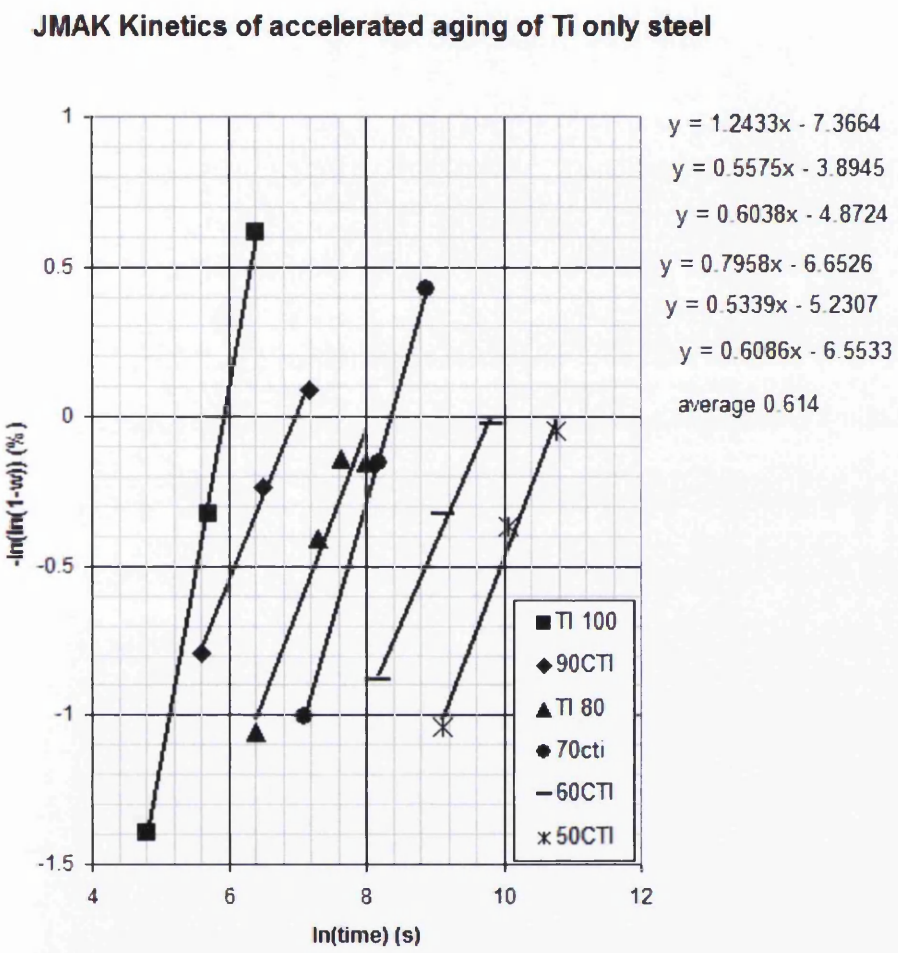

Figure 5.13 Determination of the JMAK kinetic exponent for aging of steel one (Ti-Only) only the temperature range 50°C to 100°C, based on partial aging responses developed in figure 5.9

Figure 5.14 shows the aging kinetics for the TiV only steel annealed at 860°C and aged over the temperature range 50°C to 100°C, as determined from the JMAK equation. Discounting the 100°C measurement the average kinetic exponent is 0.688.

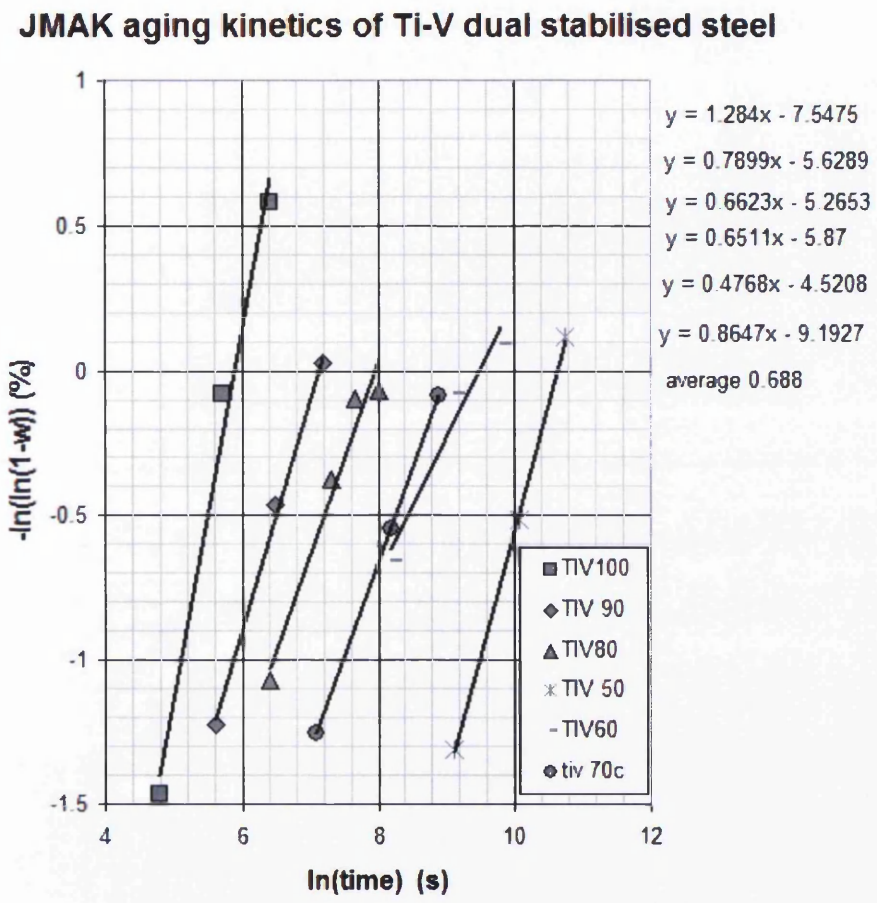

Figure 5.14 Determination of the JMAK kinetic exponent for aging of steel two (Ti-V dual stabilised) only the temperature range 50°C to 100°C, based on partial aging responses developed in figure 5.10

Figure 5.15 shows a plot of the kinetic exponents for aging of the Ti only steel annealed at 880°C and TiV steel annealed at 860°C, aged over the temperature range 50°C to 90°C. The green line shows the average exponent for the TiV steel, the blue the average exponent for the Ti only steel. Three out of five points for the TiV steel lie above the mean, and three for the Ti only lie below the mean, both averages having been altered by outliers at 60°C and 70°C respectively.

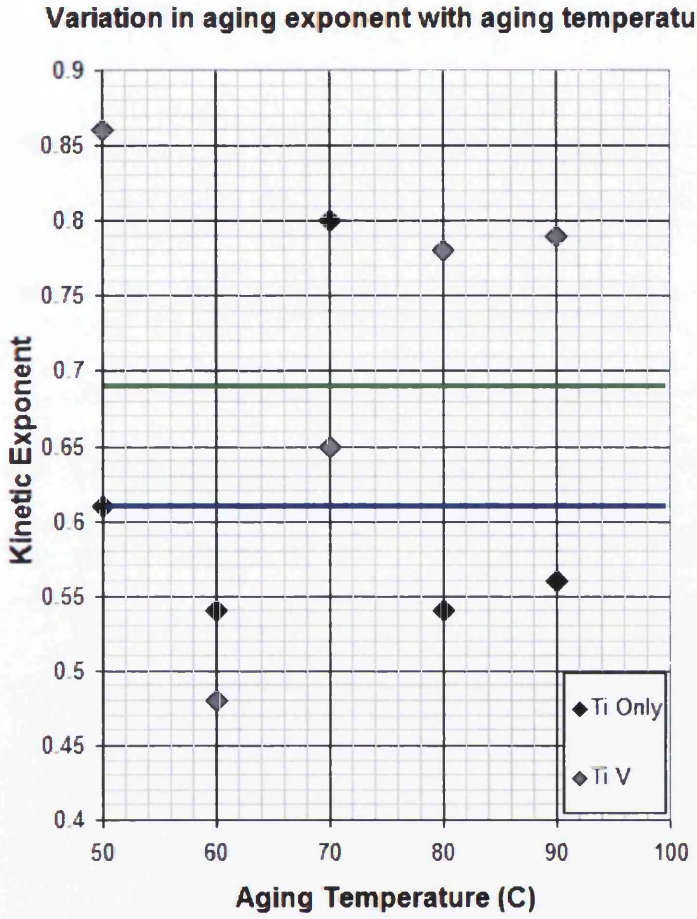

Figure 5.15 A comparison of the JMAK aging kinetics of steel one (Ti-Only) annealed at 880°C and Steel two (Ti-V dual stabilised) developed from the partial aging traces in Figure 5.9

5.3. Transmission Electron Microscopy

Transmission Electron Microscopy has been used for two purposes in this investigation – to support the proposed precipitation route for stabilisation of the steel, as predicted using MT-DATA, and to try and locate nano-scale vanadium carbide particles capable of acting as carbon sinks in the lattice through strain field interaction with free interstitial carbon atoms.

A sample of the titanium-vanadium dual stabilised steel was annealed using the cycle described in section 4.3.3, to induce recrystallization and release a population of free carbon atoms into solution. Following annealing 15mmx15mm samples were manually cut from the annealed panel using a Discotom disc cutter to avoid introducing deformation into the sample. The square samples were then ground down from 1mm nominal thickness to 25μm using static strips of 120, 240 and 500 grit silicon carbide paper, the sample being supported throughout within a stainless steel holder that prevented any bending of the sample. [100] 3mm diameter discs were machined from the sample, and chemically thinned to 200nm for examination.

5.3.1. Transmission Electron Microscopy Results

Three main types of precipitates were identified through transmission electron microscopy in the titanium-vanadium dual stabilised steel. EDX results uniformly contained high levels of copper that were not present in the steel chemistry, and these are considered to be artefacts due to the use of a brass sample holder TEM EDX analysis rather than the recommended beryllium sample holders.

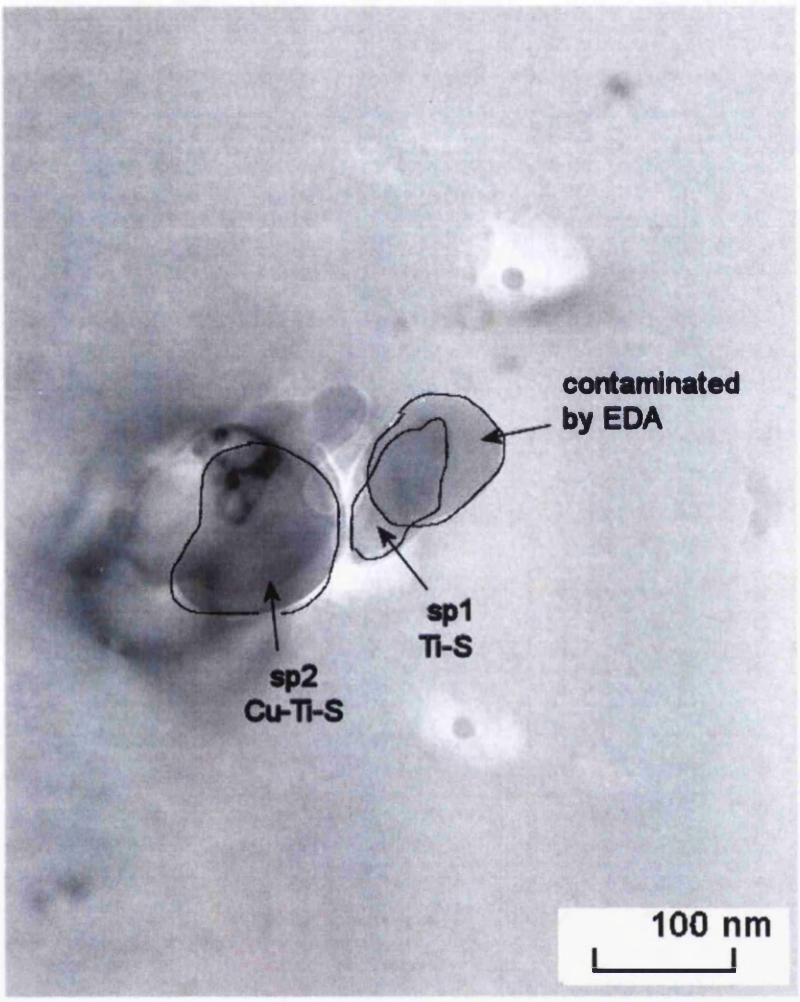

Figure 5.16 Bright field TEM micrograph taken from steel two (Ti-V dual stabilised) following annealing at 860°C. The micrograph shows two TiS precipitates, SP1 and SP2.

Figure 5.16 is a bright field image displaying two particles with a composition that matches closely that of TiS, identified through Energy Dispersive X-Ray spectrometry. SP1 has a composition containing 68.9wt.% Ti and 31.1wt.% S, somewhat in excess of the expected 3:2 stoichiometry for TiS. SP2 was found to contain 40.2wt.% Ti, 35.9 Wt% S with 23.9wt.% Cu displayed in the EDX results dues to scattering of X-Rays on the brass holder.. SP1 has a mean diameter of 86nm and SP2 a mean diameter of 118nm.

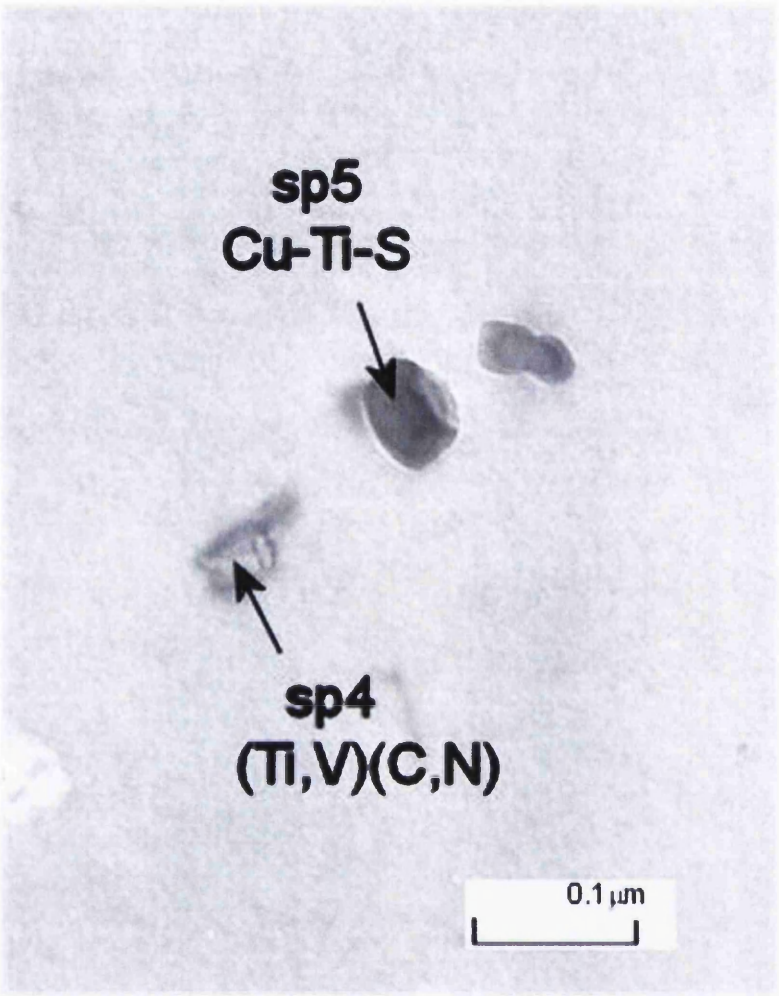

Figure 5.17 Bright field TEM micrograph taken from steel two (Ti-V dual stabilised) following annealing at 860°C. The micrograph shows a cubic precipitate (SP4) with EDX spectra displaying titanium, vanadium, carbon and nitrogen, and a larger precipitate with spectra displaying titanium, sulphur and copper.

Figure 5.17 is a bright field TEM image containing two identified precipitates; SP4 is a small cubic precipitate with EDX spectra containing Titanium and vanadium (87.3wt.% and 12.7wt.% respectively) and an edge length of 40nm. SP5 is a larger TiS precipitate for which the EDX trace contains 40wt.% each of titanium and sulphur with 20wt.% Cu displayed in the EDX results due to X-Ray scattering.

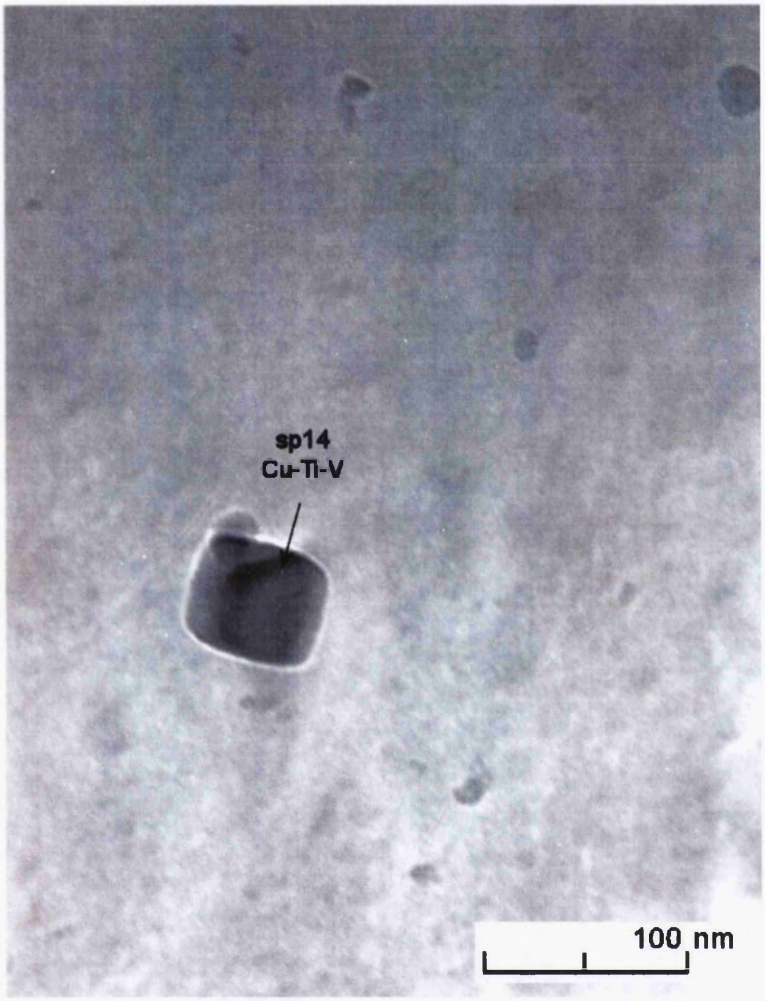

Figure 5.18 Bright field TEM micrograph taken from steel two (Ti-V dual stabilised) following annealing at 860°C. The micrograph shows two overlapping precipitates, a larger cubic precipitate, and smaller spherical precipitate.

Figure 5.18 is a bright field image showing the co-precipitation of a 60nm cubic precipitate and smaller 25nm spherical precipitate. EDX analysis shows the composition to be 62.3wt.% copper, 35wt.% titanium and 2.7wt.% vanadium.

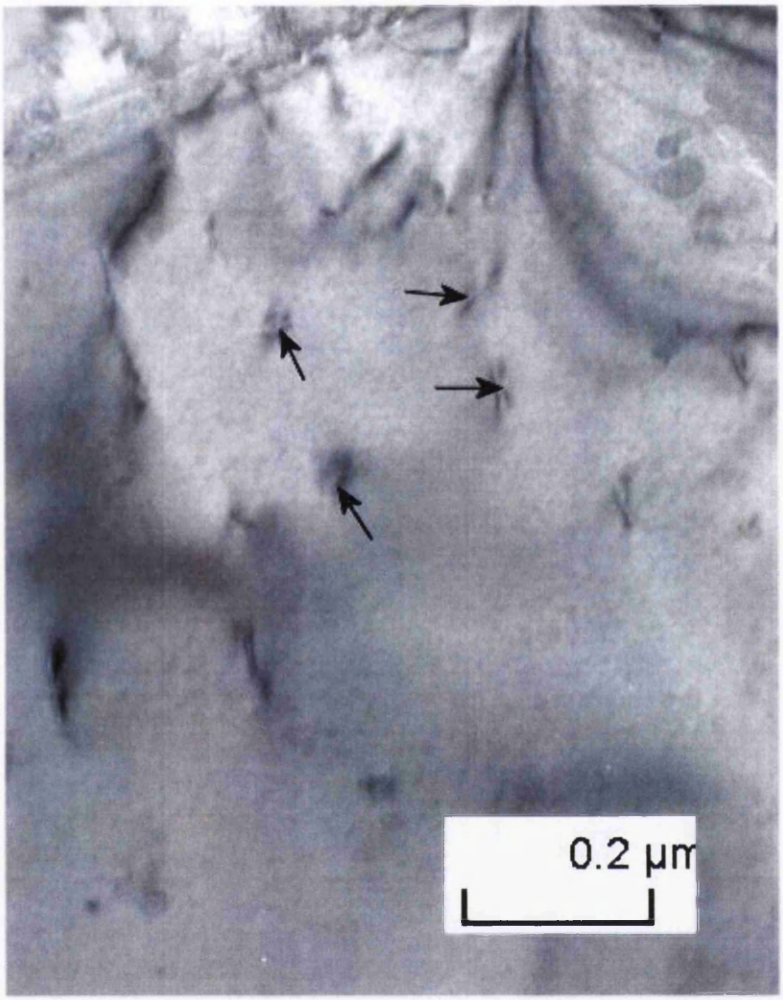

Figure 5.19 Bright field TEM micrograph taken from steel two (Ti-V dual stabilised) following annealing at 860°C. The micrograph shows strain field contrast caused by precipitates too small to analyse through EDX.

Figure 5.19 shows, via strain field contrast, the presence of a number of small coherent precipitates in the lattice. These precipitates were too small to identify using the EDX capability of the Phillips TEM, but two dark lobes separated by a region of no contrast are clearly visible.

CHAPTER 6

EXPERIMENTAL DISCUSSION

6. EXPERIMENTAL DISCUSSION

6.1. The retarding effect of vanadium on rates of strain aging

The Isochronal plots developed in section 5.1 show a definite retarding effect of vanadium on the rates of strain aging between the two steels. As stated in section 5.1.1, if vanadium had no effect on the rate of strain aging, it would be expected that a steel stabilised using only titanium, and a steel stabilised using titanium and vanadium would share a common aging curve as a function of carbon content, at a given time.

Examining Figure 5.6 to Figure 5.8 there is a clear reduction in the aging response of the Ti-V dual stabilised steels at lower carbon contents, with this effect dropping off as carbon content rises from 5 to 10wt.ppm. There has been some argument, historically, over the role that grain size plays in the magnitude of bake hardening response, with Messien and Leeroy and Okamoto [79, 101] providing evidence that, at smaller grain sizes bake hardening response would be expected to increase for an equivalent level of free carbon

Considering the low free carbon case (5wt.ppm) where the difference in aging response was greatest, the titanium-vanadium dual stabilised steel was found to have a smaller grain size of 9.4μm microns compared to 10.3 μm (figures 4.1 and 4.3). Accepting that, in the formation of Cottrell atmospheres, the increase in yield strength is proportional to the extent of atmosphere formation, a steel having a finer grain size would then be expected to show an increased aging response as a function of time when compared to one with a coarser grain structure; this is not the

case, with the finer grained Ti-V steel showing an aging response that is roughly 10% lower at all considered times.

With reference to the higher carbon case, where the Ti only and Ti-V isochronal plots intercept, it is the Ti-V steel that has the larger grain size of 13.5 microns compared to 10.5 microns for the Ti only.

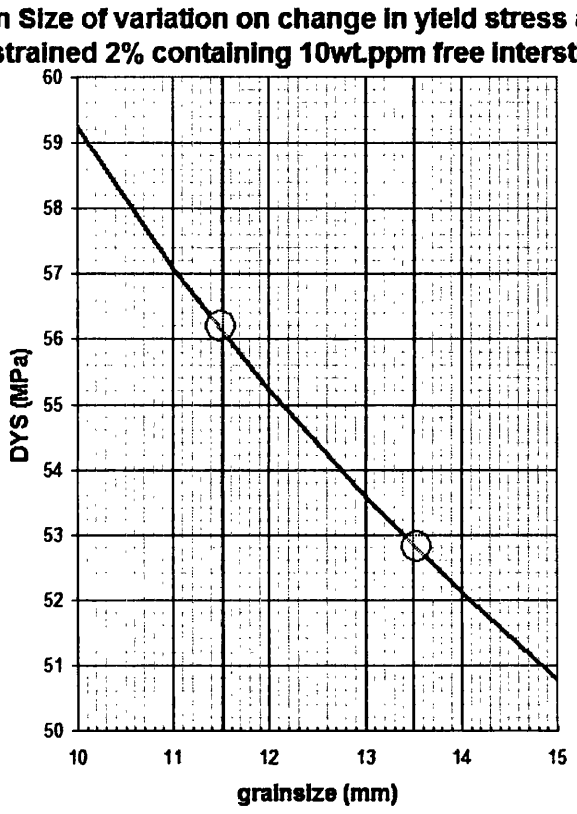

Figure 6.1 Variation in bake hardening response with grain size in microns plotted after [79]

Comparing these grain sizes to fits of Messien and Okomoto's data (Figure 6.1), one would expect a 6% increase in the aging response of the Ti only steel compared to the Ti-V. The data produced in this work, however, shows the Ti-V steel to age as rapidly as the Ti only steel at carbon contents above about 8wt.ppm free carbon.

This suggests that, at higher carbon contents, the vanadium addition has in fact accelerated the rate of aging in the steel.

A study of the effect of grain size on aging rates has not formed a part of this body of work, the focus here being more on modelling the atomistic process of dislocation locking over the macroscopic process of bake hardening in steels, however, conclusions can be drawn from the isochronal plots produced in combination with reported literature.

At low free interstitial carbon levels (ca.5wt.ppm) vanadium additions can be seen to have a clear retarding effect on rates of strain aging at 100°C, irrespective of grain size effects (which would have been expected to accelerate the rate of strength increase in the dual stabilised steel).

At higher free interstitial carbon levels the retarding effect of the vanadium additions is non-existent, and, if grain size effects do in fact play a part in the overall magnitude of the aging response, rates of strain aging may, when measured as a function of the increase of yield stress, in fact increase.

With regard to the two common hypotheses for retardation of strain aging in steels, these results would seem to support an interaction between free interstitial carbon atoms and coherent vanadium carbide precipitates over a direct dipole interaction between free interstitial carbon atoms and substitiutionally present vanadium. The alloy investigated contains a large quantity of vanadium relative to the free carbon

population, approximately twenty times the level required to fully stabilise the carbon population as $VC_{0.88}$.

The reduction of the retarding effect of vanadium at higher carbon levels suggests there is a saturation level, beyond which the vanadium addition is no longer able to tie up further carbon atoms; if the interaction were occurring directly between carbon and vanadium atoms this saturation level would be expected to be high (approaching stoichiometry) rather than the rapid drop off in retardation at relatively low free carbon levels. If, however, the retarding effect were caused by an interaction with the strain fields around coherent precipitates this effect is more readily explicable. From a kinetic and stand point, there is a limit to the amount of vanadium carbide that would be able to form on a quench from 860°C, and the ability of this population of precipitates to act as a carbon sink would be more limited than that of solute vanadium.

To summarise, the isochronal plots show vanadium to have a limited retarding effect on rates of strain aging, which may combine with grain size affecting the overall aging response of the steel. The drop off in retarding effect at higher carbon contents tends to support an interaction effect between free carbon atoms and vanadium precipitates over a direct interaction between free carbon and free vanadium atoms.

6.2. Variation in strain aging kinetics in the presence of vanadium

The method adopted in this body of work for the back derivation of the aging kinetics and activation energies has previously been used with reference to strain aging by Tanikawa, and Rashid [15, 102]. However, in previous works it has not been stated how the initial curve fits to the aging data have been performed. For the sake of transparency, and accuracy, a comparison was made between the quality of the fits produced to the raw aging data when using the logistic equation, a descriptive equation derived by Elsen and Hougardy, and the Johnson-Mehl-Avrami-Kolmogorov equation, frequently used to fit sigmoid processes like transformation kinetics and grain growth.

In Figure 5.1 to Figure 5.4 the three curves used to fit the data can all be seen to give a close match when fitted with no constraints; of the three equations the Logistic equation would be expected to give the best-fit through the presented data, but it's general shape is not guaranteed to pass through the 0,0 intercept. The Elsen and Hougardy equation and the JMAK equation are both guaranteed to pass through the 0,0 intercept and produce sigmoid type curves. As shown in

Table 5-1, the difference in the RMS error from the mean for the two fits is small (0.11MPa), with the JMAK equation giving the better result compared with Elsen and Hougardy's equation using an exponent of 0.9 as suggested in their paper [25].

The JMAK equation shows the greater tendency to level off at the later stages of aging, showing a distinct end to the formation of Cottrell atmospheres, while the Elsen and Hougardy equation still possesses a positive gradient at the highest measured aging responses. For this reason the JMAK equation has been adopted for the fitting of aging curves in this exercise

Activation energies have then been determined as a function of the time required to achieve an equivalent aging response with varying temperature, fitted for a linear function using least squares error. It is necessary at this point to state that the activation energies generated in this study are produced using a fitted curve, which has itself been fitted to data produced from fitted aging curves. It is accepted by the author that this method may result in some inaccuracies in the final numerical result, however, the aging response has been determined from discrete aging tests at times assumed equivalent using Hundy's equation. As such, the test data describes discrete points on the aging curve rather than the continuum of aging behaviour. It is not possible to perform this operation without making some assumptions, and performing some manner of curve fitting operation. As such it has been attempted in this work to perform the fits as accurately as possible, and in any event with complete transparency regarding the method, for future researchers. Tests have been performed in duplicate, at multiple conditions, and over a range of temperatures and, while the final numerical values might differ with a larger programme of testing, there is strong evidence within this body of work to support the observed trends.

The curve fits showing the greatest deviation from the experimental data are seen at 100°C in the case of both tested steels. This result is not unexpected, as following aging the tensile coupons were air-cooled and, as at 100°C the aging process is very rapid, aging is likely to have continued to some extent after the tensile coupons were removed from the aging furnace.

In previous investigations Tanikawa [102] and De et al [36] have both observed dogleg type curves containing an inflection point when deriving activation energies for strain aging. Tanikawa located this inflection point above 100°C (in which event it would not be expected to be evident within the data produced for this study) while De et al located an inflection point at 77°C, with the a JMAK kinetic exponent of roughly 0.7 below 77°C and 0.5 above. In addition the activation energy for the process was found to vary above and below 77°C, with the energy below being that expected for carbon diffusion in ferrite, and that above for the formation of pre-precipitate clusters in bainite formation.

No inflection point was evident in the derived activation energies for this study. However, it was the goal of De et al to look at precipitation effects in Ultra Low Carbon steels – as such their composition contained 21wt.ppm of free interstitial carbon. The aging studies performed in this programme of work have focussed on far lower levels of free interstitial carbon (<10.wt.ppm) and, while Elsen and Hougardy have observed two stage aging kinetics in steels containing carbon levels as low as 5wt.ppm [25] the second stage of aging (the formation of carbon atom clusters at dislocations and formation of cylindrical epsilon-carbides) may not have occurred in this study – the measured aging responses in the activation energy

study, over which the aging temperature was varied, were of the order of 20-30MPa, consist ant with the expected yield strength increase from Cottrell Locking alone.

Accepting the inherent errors in the manner in which the activation energies have been derived the difference in activation energy for the aging processes with and without vanadium present may not be significant. The titanium-vanadium dual stabilised steel was found to have an activation energy for strain-aging 5kJMol^{-1} lower than the titanium only steel, 90kJMol^{-1} compared to 95kJMol^{-1}. Both are significantly in excess of the activation energy for carbon diffusion in ferrite, taken in this work from Soenen et al. [57] as 82kJmol^{-1}.

The possibility of performing an EBSD study of the lattice parameter was discussed with an expert [103] to see whether vanadium additions at the studied level were sufficient to produce an overall increase in the lattice parameter of the BCC ferrite matrix, and thus a reduction in the energy barrier to carbon diffusion and associated decrease in activation energy. It was the opinion of the operator that the probability of observing any effect at the alloying levels used was negligible when compared to the accuracy of the process, without processing a number of samples that would have been prohibitively expensive. For this reason EBSD was not pursued.

The activation energy study also found the pre-exponential Arrhenius coefficient to be an order of magnitude lower for the Ti-V steel when compared to the Ti only steel which, accepting similar activation energies, would result in longer required times to evolve an equivalent strength increase in the Ti-V steel.

To summarise the activation energy study, there is insufficient evidence to state whether the activation energy for the process of strain aging differs between the two grades being studied when considered as a thermally activated Arrhenius type process. There is however a difference in the process kinetics highlighted in the pre-exponential Arrhenius coefficient and JMAK aging exponent showing that the two processes are not the same; this serves to support the evidence generated through the derived isochronal plots, that the retarding effect of vanadium and its effect on process kinetics is a measurable phenomenon.

6.3. TEM evidence of coherent vanadium carbide nucleation

Some aspects of the Transmission Electron Microscopy results are open to interpretation due to the erroneous copper trace displayed in the EDX results as a result of the use of a brass specimen holder.

Figure 5.16 and Figure 5.17 strongly suggest titanium sulphide to have formed in the matrix during pre-processing, as expected using traditional stabilisation considerations, rather than the manganese sulphide predicted by MT-DATA, based solely on equilibrium considerations of the composition. Particular credence can be given to Figure 5.16 in which SP1 did not display the copper trace resulting from the brass sample holder. This precipitate, however, has a titanium:sulphur ratio of 3:1 – stoichiometrically high for pure titanium sulphide. The particles under discussion, considered to be TiS, are of a similar size to those identified by Ooi and Fourlaris in a previous study of Ti-V dual stabilised ultra low carbon strip which, given the similarity between compositions and processing parameters, is not unexpected [68]

This highlights one of the limitations in the use of thermodynamic software like MT-DATA in planning experimental procedures. Hot rolling processes involve reasonably rapid cooling from the furnace temperature (1250°C) to the finishing temperature (920°C) then water quenching down to the coiling temperature of 700°C. Equilibrium microstructures may not result from such a cooling regime due to kinetic factors.

While carbon and nitrogen cannot be detected directly using EDX, the cubic precipitates containing a significant weight fraction of titanium are likely to be titanium nitride, as titanium nitride and titanium carbide can be distinguished by their shape, the nitrides tending to be coarser than carbides and cubic rather than spherical[104].

The traces of vanadium in the cubic precipitates may represent one of two effects. Ooi and Fourlaris found TiN to provide a favourable location for precipitation of vanadium carbide precipitates due to the semi coherent interface between the face centred cubic (FCC) TiN and VC [68]. Figure 5.18 shows the co precipitation of a small spherical precipitate and larger cubic precipitate with a high titanium and low vanadium composition, and this may be an example of this heterogeneous nucleation effect.

Alternatively, FCC titanium, niobium and vanadium carbides and nitrides are known to be soluble in one another and the EDX results for precipitates SP4 and SP14 may be a representation of this effect, with carbo-nitride complexes forming. The evidence produced within this TEM study is not sufficient to choose between the two hypotheses.

Finally, while the precipitates shown in Figure 5.19 were too small to image directly or obtain EDX spectra, they do show a strain field interaction with the lattice which could, potentially, act as a carbon sink removing free interstitial carbon atoms from solution in a similar fashion to the interaction zone around dislocation cores. Given the extended soak of the steels before hot rolling at 1250°C to dissolve existing

precipitates it seems unlikely that these precipitates would be residual from prior processing. The annealing treatment applied to Steel Two, with a soak of 860°C, should have been sufficient to dissolve any vanadium carbide present in the lattice. Given the quench rate of 60°C/s it seems likely that any precipitates reforming during cooling would be VC, rather than the more stable TiC which forms at higher temperatures.

Location of these coherent precipitates through TEM adds weight to the hypothesis that the retardation of strain aging phenomena in ultra low carbon steels may be due to a direct interaction between free interstitial carbon atoms in solution, and strain fields generated by the misfit of nano-scale precipitates in the ferritic lattice.

6.4. Experimental summary

For the purposes of generating validation data for a subsequent computer modelling exercise the experimental results generated cover a range of carbon contents and aging temperatures, both with, and without, the presence of vanadium as an interacting secondary element.

Strong identifiable trends are visible in these data sets with higher aging temperatures and higher carbon contents resulting in aging phenomena progressing more rapidly, and vanadium having a variable effect depending on the level of free carbon. These process variables provide a wide base for model validation, which will serve to support the effectiveness of the technique developed through this body of work.

In addition to this key conclusions can be drawn from the experimental results as they stand. Vanadium has a measurable retarding effect on the rate of strain aging in ultra low carbon steels. This effect is largest at low free interstitial carbon levels and decreases to become negligible as the free carbon content approaches 10wt.ppm. While there is insufficient data to state categorically whether the vanadium addition alters the activation energy for the aging process, it does result in an order of magnitude decrease in the pre-exponential coefficient when the aging data is considered as an Arrhenius type event. It is likely that this effect is caused by an interaction between free interstitial carbon atoms and the strain fields associated with coherent vanadium carbide precipitates in the lattice, these strain fields having been imaged using strain field contrast in bright field TEM imaging

CHAPTER SEVEN

COMPUTER MODELLING

7. MODELLING

This section describes the generation of three Kinetic Monte Carlo models for the purpose of simulating strain-aging phenomena. The first model discussed is a published technique produced by Soenen et al [57], and has been reproduced using in house code to determine its robustness technique. The second and third models discussed represent attempts to produce a Kinetic Monte Carlo model having shorter run times, without sacrificing accuracy, through the application of the Bortz-Kalos-Liebwitz algorithm in what the author believes to be a novel application. Additional modelling work is also presented showing the potential of the Kinetic Monte Carlo technique to reproduce retarding effects observed in the experimental data.

All computer code has been produced by the author using Compaq Visual FORTRAN 6, programmed using Fortran90 and compiled using the Compaq Developer Studio.

7.1. The requirement for modelling of strain aging

A bake hardening product can only be viable if guarantees can be given in terms of its aging behaviour, describing expected returns of yield point elongation and strength increase both in storage, and in service.

Numerous attempts, detailed in section 1.4, have been made to numerically predict rates of aging in terms of percentage completion of Cottrell atmosphere formation and the formation of dislocation precipitates. Attempts to produce computer models

of the process appear to be less common, with in roads having been made using phase field modelling and Kinetic Monte Carlo. As a technique phase field modelling is heavily dependant upon certain constants, such as interfacial boundary energies and bulk phase energies that are difficult to measure in terms of processes occurring on an atomic scale and. While intrinsically free of any scale, phase field simulations are typically implemented where bulk diffusional properties can be used as a driving energy for the simulation.

Kinetic Monte Carlo simulations offer several advantages in the model of strain aging; KMC is essentially an atomistic technique however, by relating atomic behaviour to bulk material properties, and only modelling structural defects, it is possible to model physical processes that occur over large volumes of time. The frequency of atomic vibrations is ignored, and an attempt frequency and jump frequency are inferred from the bulk properties.

Additionally, the nature of KMC is such that the act of modelling a process confirms or refutes our understanding of it. It is widely held that Cottrell atmospheres form by the bulk diffusional movement of carbon atoms to dislocation cores to minimise strain energy in the lattice; a model that proceeds on the basis that this is true will test this assumption. If it is possible to reproduce the aging response of materials with the appropriate observed kinetics and activation energies, it can be inferred that the understanding of the model is in fact correct.

Finally, computer models have significant capacity to evolve and encompass a range of other techniques, or more complicated scenarios. An existing model can be

modularised and ported into a larger frame, or expanded to include additional processes or interaction effects. Computer models can also grow to include existing numerical models, allowing for more rapid solution and incorporation into a chain of calculations that would prove laborious to pursue manually. In the case of the KMC modelling of strain aging, once the interaction behaviour between an interstitial and substitutional species has been reproduced, other species can be modelled by adapting existing parameters and applying the same algorithm – for instance the generic modelling of dipole interactions as a carbon sink.

The computer modelling of strain aging is an important step in confirming and improving our understanding of aging processes, and Kinetic Monte Carlo is a highly versatile technique with a history of use in studying atomic interactions in semiconductors. It also provides a technique capable of producing long-term simulations (months of simulated time) within a real time frame that is appropriate for a desktop tool with industrial relevance, and as such has been adopted for this investigation.

7.2. Locally activated Kinetic Metropolis Monte Carlo algorithm

A Kinetic Monte Carlo simulation of strain aging has been published by Soenen et al, accounting for both diffusion of carbon atoms to dislocations during aging, and grain boundary segregation during the annealing process, and the results of this group have shown a strong correlation with their experimental data [57].

The model developed in that paper has been reproduced during this study. The kinetics are controlled by a set of Arrhenius type equations controlling jump frequency, relating to jumps between positions of equivalent energy within the bulk material, and jumps to sites of higher or lower energy, within a critical radius around dislocations.

The frequency of jumps between equivalent sites, f_d, is controlled by an attempt frequency, v, and U_d, the energy barrier to diffusion, which was taken as 82000J/mol, approximately equal to the activation energy for carbon diffusion. [57]

$$f = f_d = v\exp\left(-\frac{U_d}{RT}\right) \qquad v = \frac{D_0}{a^2} \qquad \text{7-1}$$

Here R is the gas constant ($8.3145 JK^{-1}mol^{-1}$), T the absolute temperature(K), D_0 the coefficient of diffusivity for carbon in ferrite ($2x10^{-6}\ m^2s^{-1}$) and a the lattice parameter of a bcc ferrite unit cell (2.87Å).

Where a diffusive jump moves an atom between two sites, i and j, with respective energies U_i and U_j the jump frequency f_d is again observed if the energy of the target site is lower; if a jump takes an atom to a higher energy site the frequency is related exponentially to the energy difference between the two positions [57]

$$f(i \rightarrow j) = f_d \qquad U_i > U_j \qquad \text{7-2}$$

$$f(i \rightarrow j) = f_d \exp\left(-\frac{U_j - U_i}{RT}\right) \qquad U_i < U_j \qquad \text{7-3}$$

The program records the co-ordinates of all solute atoms and dislocations, and interaction energies are read from energy 'templates' if carbon atoms are within the

calculated radius of interaction (r_c). The critical radius of interaction allows for a minimum variation of 10% from the normal jump frequency and is calculated as [57]:

$$r_c = \sqrt{\frac{2Aa}{RT\ln(1.1)}} \qquad 7\text{-}4$$

The interaction energy of each site is calculated using:

$$U = \frac{A\sin\theta}{r} \qquad 7\text{-}5$$

Where (r, θ) is the polar co-ordinate of the solute atom with respect to the dislocation line and A is the solute dislocation interaction parameter (taken as $7.5\text{x}10^{-6}$), T is the absolute temperature of the system and R is the gas constant.

At the beginning of the program, carbon atoms are randomly placed throughout the mesh at the cell centres, and dislocations at the edges of unit cells. Each carbon atom has a local clock that keeps track of its location in time, this clock being updated every time the atom makes a diffusive jump. The algorithm proceeds as follows (**Figure 7.1**):

1) Select that carbon atom for which the least amount of time has passed.
2) Set the simulation time to the local time of the selected atom.
3) Using a random number generator determine in which of the four possible directions the carbon atom will jump, based on the relative jump frequencies.
4) Check whether the destination site is vacant; if so, perform the diffusive jump, if not, the selected atom remains stationary.
5) Calculate the jump frequencies for the atom in its new position.

6) Update the atoms' local clock by the amount of time that will be required for it to perform its next diffusive jump.

7) Re-sort atoms by their local clocks.

A periodic boundary condition has used in all cases.

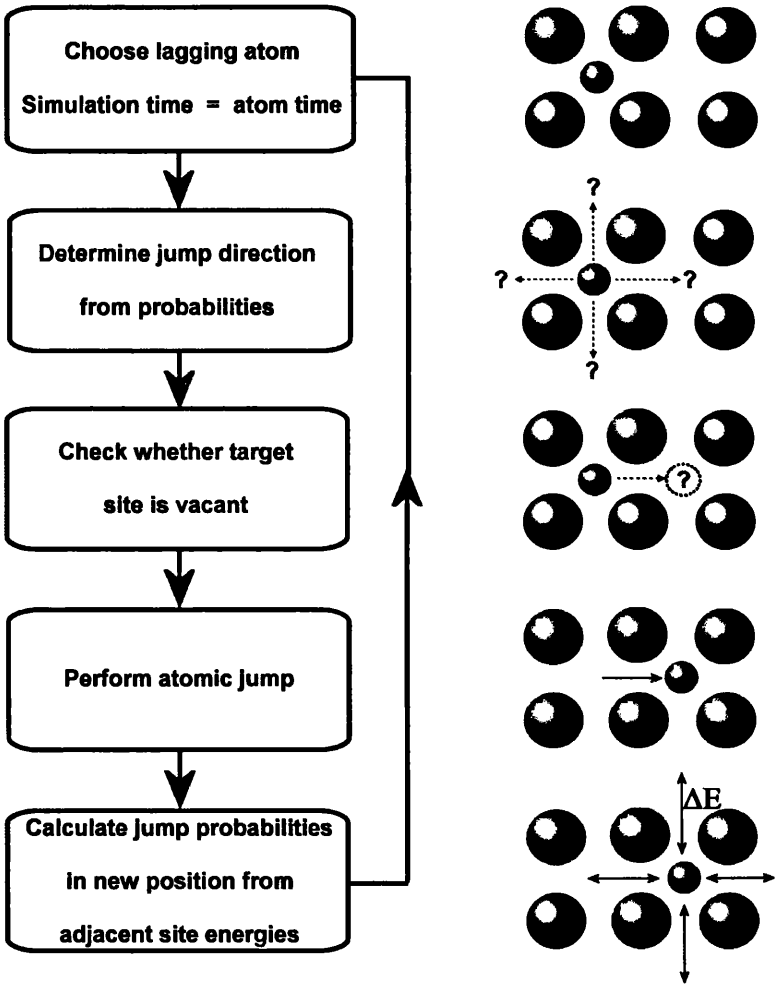

Figure 7.1 A graphical representation of the locally activated Kinetic Monte Carlo Algorithm

7.2.1. Sensitivity analysis

Trials of this model were aimed at assessing the effect of mesh size and shape on the accuracy of the Kinetic Monte Carlo technique, and on the ability of the model to assess a range of temperatures and carbon contents (

Table 7-1). To this end, experimental plots have been reproduced from papers by Elsen and Hougardy [25], De et al. [73]and Zhao et al. [40] to represent a range of experimental carbon contents and aging temperatures.

Table 7-1 Run details for the sensitivity analysis performed using the locally activated Kinetic Monte Carlo Model

Mesh dimensions ('000 elements)	Mesh Elements ('000,000 elements)	Temperature (K)	Carbon (wt.ppm)	Caride former (wt.ppm)
SIZE				
10 x 10	100	323	5	-
15 x 15	225	323	5	-
22 x 22	484	323	5	-
35 x 35	1225	323	5	-
SHAPE				
15 x 15	225	323	5	-
19 x 12	228	323	5	-
28 x 8	224	323	5	-
56 x 4	224	323	5	-
112 x 2	224	323	5	-
TEMPERATURE/CARBON				
15 x 15	225	323	5	-
15 x 15	225	323	6	-
15 x 15	225	323	6.4	-
15 x 15	225	373	5	-
15 x 15	225	373	6	-
15 x 15	225	373	6.4	-
Carbon Stabiliser				
15 x 15	225	323	5	225

Further runs were then performed to include the impact of a strongly carbide forming element in solid solution. In these simulations 225 wt.ppm of solute with an atomic weight of 51 (vanadium) were dispersed randomly over the area simulated on a 15,000 by 15,000 element grid, containing 5wt.ppm of carbon and aged at 323K. The substitutional atoms were placed in BCC ferrite lattice sites and an interaction was assumed with carbon atoms situated at the nearest neighbour octahedral sites, with a magnitude of 20kJ/Mol. Jumps to and from these sites were controlled by the jump equation as detailed previously for sites of non-equivalent energy. Where the placement of such a substitutional atom coincided with the interaction energy field resultant from a dislocation, the effects were considered to be cumulative.

7.2.2. Optimisation of the Locally Activated Kinetic Monte Carlo Algorithm

To reduce run times and improve the efficiency of the simulation a divide and conquer methodology was adopted. To calculate the jump frequencies for the atom of interest on each time step, it is necessary that its position be compared to the positions of all dislocations and atoms of substitutionally present species that could result in an interaction in terms of lattice site energy.

In the case of the secondary species simulation shown here, this amounts to 55600 vanadium atoms, and 277 dislocations. Initial simulations attempted under these conditions were found to have unfeasible run times, potentially running into weeks. To combat this the total modelled area was subdivided into a grid, each section of which measured 1000 x 1000 mesh elements. Each potentially interacting feature in the simulation was possessed of two sets of locating coordinates; absolute

coordinates, relative to the origin of the large mesh, and local coordinates, describing the grid sector in which the feature was located, and its coordinates relative to the origin of that sector Figure 7.2.

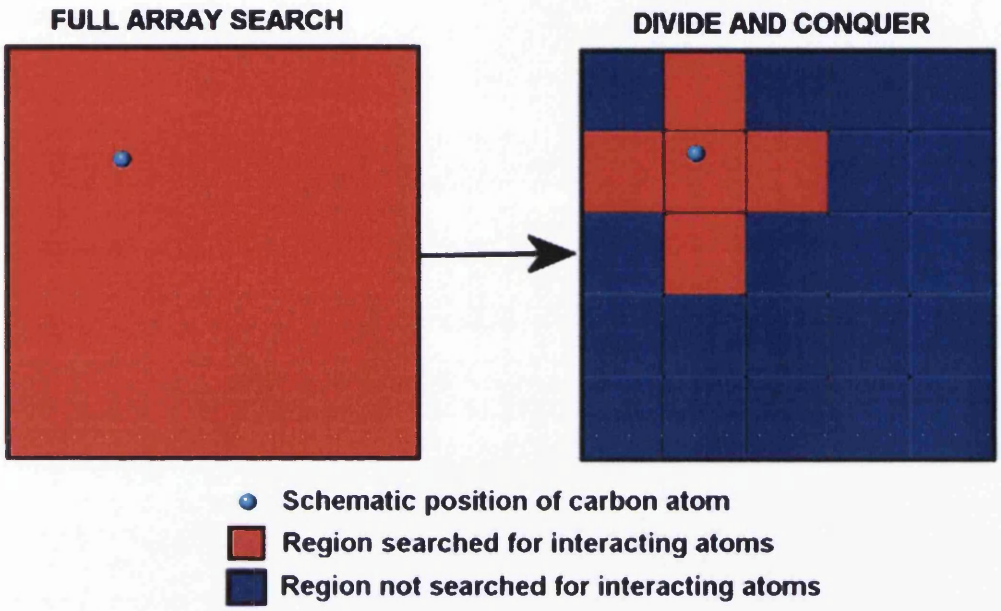

Figure 7.2 Schematic of the function of divide and conquer techniques in speed optimisation.

The carbon atom selected for a move would then be checked only against those features in the grid that it occupied and in those grids that were its four nearest neighbours, to account for any dislocations with an interaction zone that overlapped their containing grid. By comparison this represents a check against an average of 1235 vanadium atoms and 6 dislocations on each time step, or 2% of the initial number.

The relevant atomic move was then completed, and the global coordinate system updated to reflect changes that had occurred. While this represents a simplistic

application of divide and conquer techniques, when compared with other optimisation techniques such as the use multi-grid solvers for solution of partial differential equations, it does offer significant improvements in the run time of this programme and is relatively simple to implement.

The effect of dislocations in next nearest neighbour grid sectors was assumed to be negligible to preserve run times. At 50°C the radius of interaction for a dislocation core assumed by the model covers 28 mesh units, giving an interaction area of 7740 mesh elements in total. Assuming a dislocation core was placed at the corner of a sector, giving the maximum potential overlap, this would represent 1934 mesh elements, or a little under 0.2% of the sites in the sector of interest. Coupled with the fact that only 900 such corner sites exist in a total modelled volume of 225 million elements it seemed reasonable to discount them when searching for interaction effects.

7.2.3. Locally Activated Kinetic Monte Carlo Results

Figure 7.3 shows the effect of changing mesh size on the accuracy of the Monte Carlo simulation. The quality of the fit appears to improve from 100 million to 225 million elements, then degrades again as the mesh becomes larger. Figure 7.4 shows the effect of changing the mesh shape from a thin strip simulation (128,000 x 2,000 elements) through to a square simulation of equivalent area (15,000 x 15,000 elements). In these simulations the effect of changing mesh shape appears negligible.

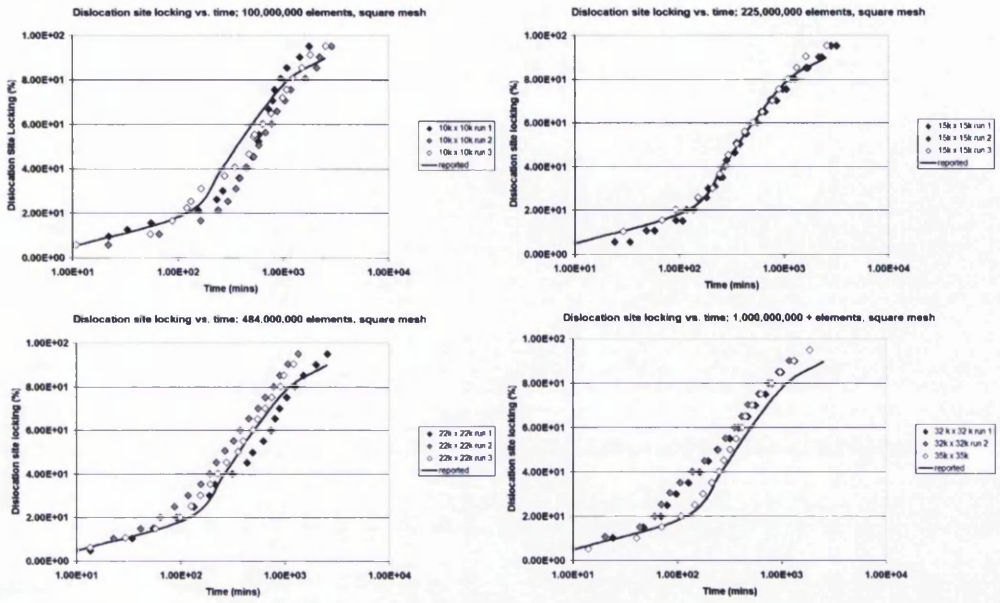

Figure 7.3 - Simulated strain aging for steel containing 5wt.ppm of carbon at 5% prestrain vs. experimental data taken from De et al. [15] on meshes of dimensions $10{,}000^2$, $15{,}000^2$, $22{,}000^2$, $32{,}000^2$

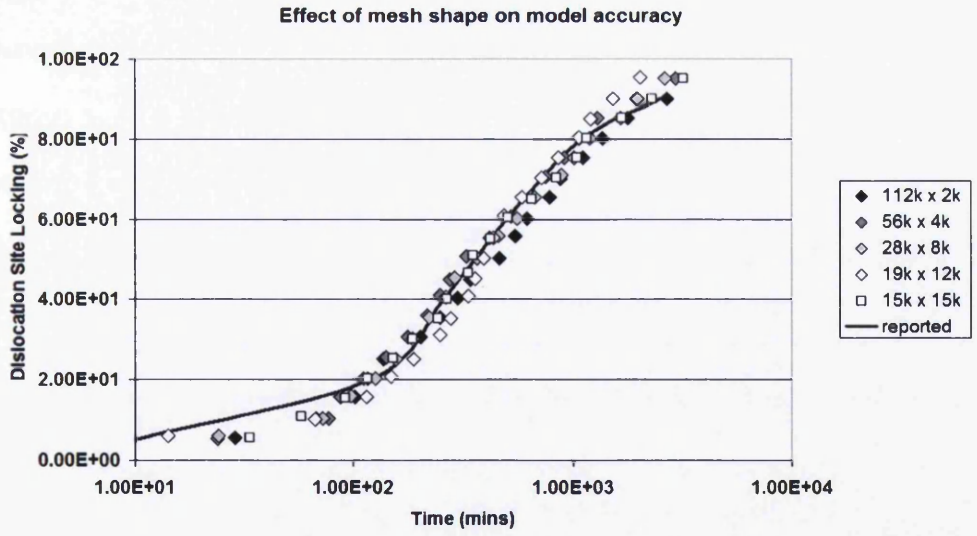

Figure 7.4 - The effect of mesh shape on simulated strain aging for a steel containing 5wt.ppm of carbon at 5% prestrain vs. experimental data taken from De et al. [15] on a $15{,}000^2$ mesh.

Figure 7.5 shows the ability of the technique to handle changing carbon content and temperature. The simulation runs are close to the reported data for experiments at 323K and follow the same trend, producing sigmoid curves that are displaced to shorter times as the carbon concentration increases.

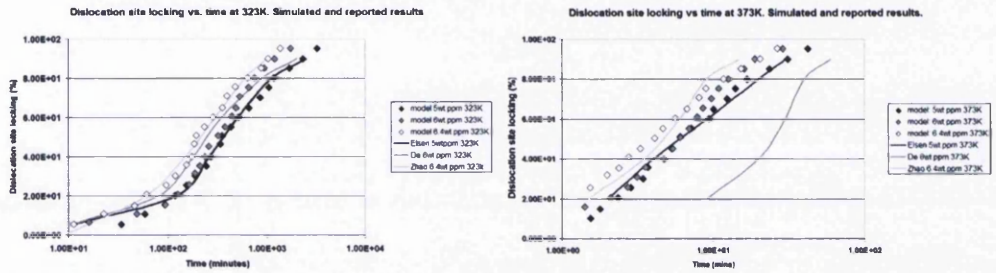

Figure 7.5 Simulated strain aging for steels containing 5wt.ppm, 6wt.ppm and 6.4wt.ppm of carbon at 5% prestrain at 323K and 373K vs. experimental data taken from De et al. [15], Zhao et al [16] and Elsen and Hougardy [6] on a 15,000^2 element mesh

Figure 7.5 shows poorer match to experimentally reported data for 373K, and the curves no longer have a sigmoid shape. The general trend of shorter aging times for higher carbon contents is repeated, but the overlap between simulated curves is greater than at 323K.

In Figure 7.6 the addition of a substitutional element that forms strong dipoles with carbon can be seen to reduce the rate at which aging occurs. The sigmoid curve is displaced to longer times, this effect being least pronounced at the start and end of the simulation

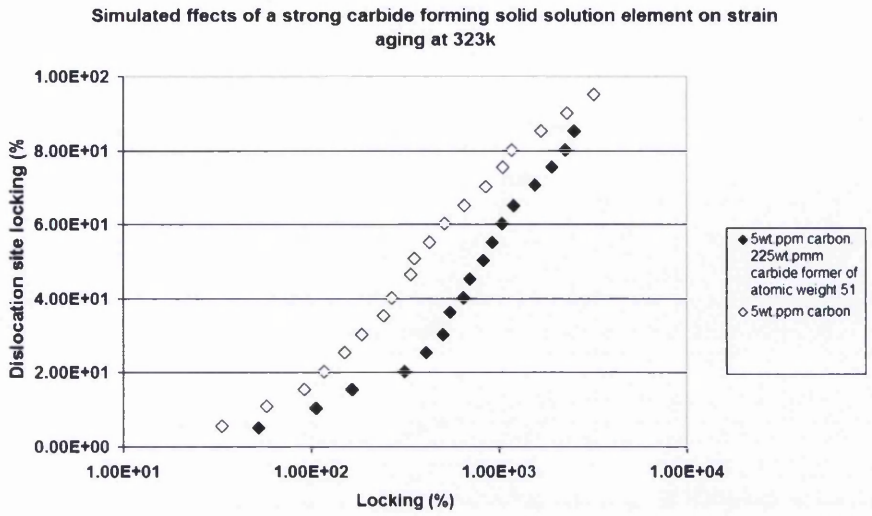

Figure 7.6 Simulated strain aging for a steels containing 5wt.ppm of carbon, and 5wt.ppm of carbon with 225wt.ppm of a strong carbide former with atomic weight 51 at 5% prestrain and 323K on a 15,000^2 element mesh.

7.3. Application of the Bortz-Kalos-Liebowitz Algorithm using Average Expected Conditions

Following on from the successful reproduction of aging behaviour using a locally activated Kinetic Monte Carlo algorithm, an attempt was made to produce a novel simulation of the aging process by applying the Bortz-Kalos-Liebowitz algorithm to the Kinetic Monte Carlo framework, and working on a smaller grid to reproduce bulk aging behaviour from the local state of the lattice.

The aging of the titanium stabilised experimental steel (steel one) has been modelled using a two dimensional application of the Bortz-Kalos-Lebowitz (BKL) algorithm [105], modified from the Kinetic Monte Carlo technique presented by Soenen et al [57].

The evolution of the system was modelled using a single dislocation at the centre of a grid having a variable edge length; the initial grid size was 900x900 elements of length 1.435×10^{-10}m, equivalent to the dislocation density of $6 \times 10^{13} m^{-2}$, or 5% prestrain[41]. This dislocation was then locked repeatedly to effectively model a region 20,000x20,000 mesh elements.

Accepting the initial dislocation spacing in the mesh of 900 mesh elements this region of material would be expected to contain 494 ($(20000/900)^2$) dislocations. The condition of the titanium stabilised steel being modelled was that following annealing at 880°C for a 60 second soak, this having been shown to liberate 9.8

wt.ppm of free carbon into solution. This gives an initial free interstitial carbon population of 37 carbon atoms.

Locking of a dislocation was considered to have occurred once a free interstitial carbon atom reached the site of maximum interaction energy directly adjacent to the dislocation core. The maximum aging response of the steel was considered to have been reached when 90% of available sites in the total modelled volume had been occupied in line with the expected locking ratio of 0.9 atoms per atom plane threaded by dislocation [29]

The atom arriving at the dislocation core was annihilated from the simulation between successive locking events as were all carbon atoms in the interacting volume (assumed to be that region around the dislocation core within which the variation in jump frequency is greater than 10% from the normal), leaving the dislocation free for repeated locking. The locations of all other carbon atoms were conserved relative to the dislocation core, and new atoms were introduced at random locations along the edges of the simulated volume.

This methodology was designed to allow the region surrounding the dislocation to continuously simulate the evolution of a local area of the microstructure. In the early locking events those carbon atoms that are close to the dislocation core would be rapidly consumed, leaving a larger population of carbon atoms at an intermediate distance from the dislocation.

Between locking events the grid size was increased incrementally to reproduce the change in the unlocked dislocation density, and the carbon population varied to account for increases due to the increasing modelled area, and decreases due to the reduction in the mean population of free carbon atoms (wt.ppm) as a result of locking events having occurred.

Assuming a total modelled volume of 20,000x20,000 mesh elements the number of unlocked dislocations on initialisation of the simulation would be 494; the total number of simulated carbon atoms would be 18,293. On locking of one dislocation this number would decrease to 493. Given a square volume, 493 dislocations would require a square of edge length equal to 22.2 times the equilibrium dislocation spacing. Maintaining the volume of 20,000x20,000 mesh units this gives a dislocation spacing of 901 mesh elements. In this way the grid size is incrementally increased over the length of the simulation to maintain the correct average dislocation density.

The number of modelled carbon atoms was then decreased with the fractional change in carbon content due to the annihilated atoms considered to be tied to the locked dislocation core. Simultaneously the number of modelled atoms is increased due to the increasing mesh area included in the run.

The BKL algorithm, as used to control the atomic jumps of free interstitial carbon atoms, proceeds as follows:

1) Sort all the possible diffusional events into four classes, describing the possible directions of an occurring atomic jump.
2) Calculate the frequency with which every possible diffusional event can occur.
3) Sum the jump frequencies, and normalise the resulting value to one, to give a relative frequency for each event.
4) Sum the normalised frequencies for each class of event giving the relative frequency for each event class.
5) Generate a random number in the interval 0<R<1, and use this to determine which class of diffusional event will occur.
6) Generate a random number in the interval 0<R<1, and use this to determine which event in the selected class will occur.
7) Perform the selected atomic move.
8) Update the simulation time.

The event frequencies and site interaction energies are determined as per the event frequencies in the locally activated simulation described in section 7.2. Δt has been calculated on each iteration of the program as

$$\Delta t = -\frac{\ln(Rand)}{\sum_{n=1}^{m_i} f} \qquad 7\text{-}6$$

where *Rand* is a random number generated in the interval 0<*Rand*<1 and *f* the frequency (Hz) of a given diffusional event in the set of diffusional events having class m.

The initial time at the start of each locking event was calculated as the locking ratio, in terms of atoms per atom plane threaded by dislocation, multiplied by the maximum

time achieved in the simulation; at the end of each locking event, the maximum time for the simulation is updated if it has been exceeded. At the end of the simulation all locking events are sorted by ascending numerical value in terms of time, and the time required for percentages of the total aging response to be achieved outputted.

7.3.1. Accelerated Aging Results for the Bortz-Kalos-Liebwitz Algorithm Using Expected Average Conditions

The modelled accelerated aging data () matches the mid-portion of the actual aging data produced through the aging of the experimental Ti only steel, annealed at 880°C to contain a FICA population of 9.8wt.ppm. The match between the modelled and experimental data is poorer during the early and late stages of aging, over predicting the required time for a given level of aging in the initial stages, and under-predicting toward completion.

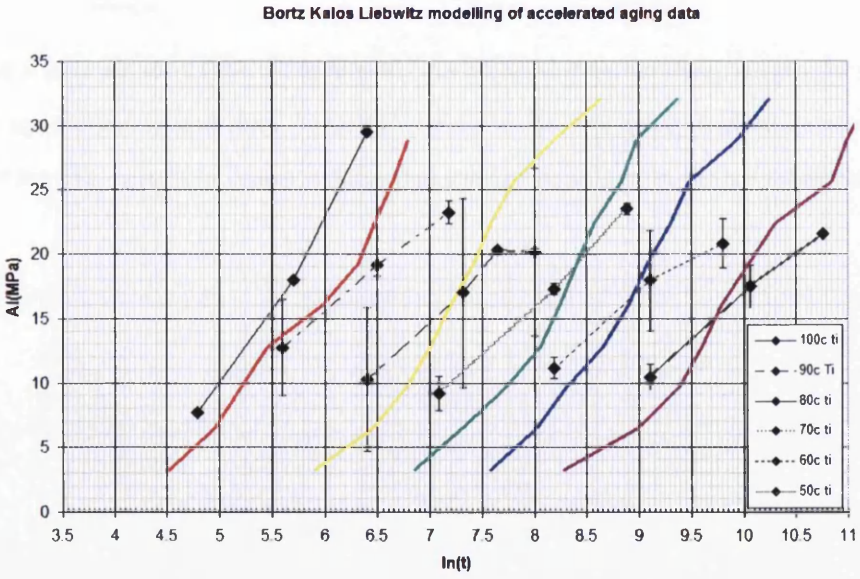

Figure 7.7. Modelled accelerated aging data compared with partial aging traces produced for steel one (Ti only) over the temperature range 50°C to 100°C generated by a variant of the BKL-KMC algorithm based on average expected behaviour in the modelled volume.

7.3.2. Aging Kinetics developed by the BKL algorithm

The aging kinetics displayed by the BKL model (Figure 7.8), based on predicted average behaviour, are significantly higher than those for the observed behaviour at all temperatures save 100°C, and are internally consistent.

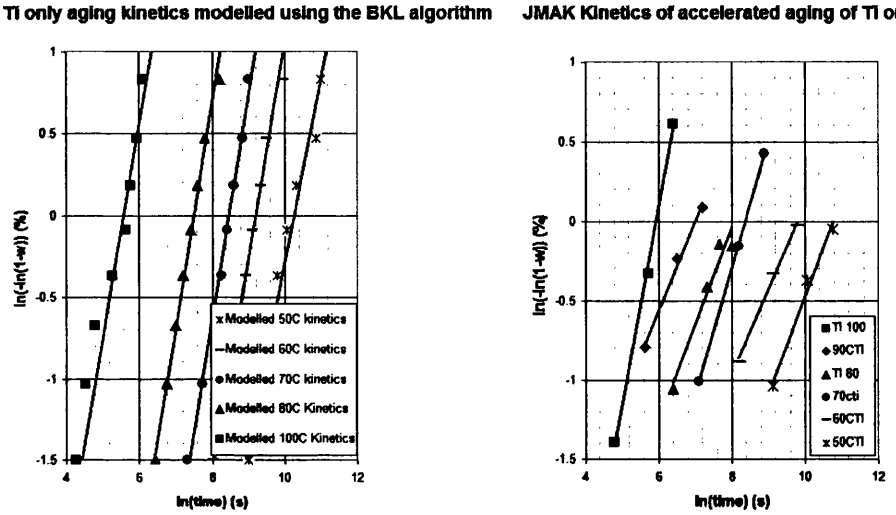

Figure 7.8 A comparison of the aging kinetics developed during accelerated aging of steel one (Ti-Only) aged in the temperature range 50°C to 100°C and the aging kinetics developed by a variant of the BKL algorithm based on expected average behaviour in the modelled volume.

7.4. Application of The Bortz-Kalos-Liebowtiz Algorithm Using The Initial Material Configuration

A further attempt has been made to apply the BKL algorithm on a small grid to the simulation of strain aging effects in Ultra Low Carbon steels. This model used the simulation developed in section 7.3 as an initial framework, with altered assumptions regarding the initial state of the model locally with respect to each dislocation

The evolution of the system was again modelled using a single dislocation at the centre of a grid having a variable edge length; this dislocation being locked repeatedly to model a region 20,000x20,000 mesh elements of unit length 1.435×10^{-10}m, or half the BCC unit cell in ferrite. Rather than calculate and apply the assumed average condition of the lattice on each successive locking event to produce a continuum, this attempt at simulation assumed that all locking events occur concurrently, starting simultaneously at a point of zero time (essentially the moment directly following the application of a prestrain, or temper rolling).

Variations in the pre-strain prior to aging were modelled using an equation back derived from a fit of data taken from Amiot and Despujols [106] with an iterative solver. On initiation of the simulation a 20,000 x 20,000 mesh element grid was set up and populated with five dislocations. The average spacing between each dislocation and its nearest neighbour was then calculated, and compared to the spacing required by the relationship.

If the mean dislocation spacing was returned as greater than the spacing required, the number of dislocations in the 20,000 x 20,000 element grid was increased by five and the calculation repeated; in this way it was ensured that the initial configuration of dislocations in each run of the simulation gave a dislocation spacing appropriate to the desired level of prestrain [41]. The lattice was then populated with carbon atoms up to a maximum population determined as a function of the desired wt.ppm free carbon population.

For each dislocation the distance between itself and each of its four nearest neighbouring dislocations was then calculated, and a mean spacing determined from these. The number of carbon atoms falling within the locus of this distance was then counted and stored with the grid spacing in a reference array. As the simulation progressed each of the dislocations in the model was locked in sequence, on a grid having an edge length equivalent to the mean spacing for that dislocation, and randomly populated with the counted number of atoms. In this way the variation in the initial positions of features in the lattice was retained, without the necessity of modelling the whole mesh as a single unit, which is both slow and processor intensive.

The BKL algorithm, as used to control the atomic jumps of free interstitial carbon atoms, proceeds as follows:

1) Sort all the possible diffusional events that can occur events into four classes, these describing the possible directions of an occurring atomic jump.
2) Calculate the frequency with which every possible diffusional event can occur.

3) Sum the calculated jump frequencies, and normalise the resulting value to one, to give a relative frequency for each event.
4) Sum the normalised frequencies for each class of event giving the relative frequency for each event class.
5) Generate a random number in the interval 0<R<1, and use this to determine which class of diffusional event will occur.
6) Generate a random number in the interval 0<R<1, and use this to determine which event in the selected class will occur.
7) Perform the selected atomic move.
8) Update the simulation time.

The event frequencies were again determined from a 'normal' jump frequency, modified for interactions, as described in section 7.1, and the time step determined as in section 7.3.

7.4.1. Secondary interacting species

The presence of a secondary interacting species has been added into the model assuming a nearest neighbour interaction effect to occur. As with the carbon atoms, for each dislocation the distance between itself and each of its four nearest neighbouring dislocations was calculated, and a mean spacing determined. The number of atoms of the substitutional secondary species falling within the locus of this distance was then counted and stored with the grid spacing in a reference array.

The interaction effect was included in the algorithm by, on each iteration, checking the position of each carbon atom in the simulated volume relative to each of the

substitutional atoms being modelled. If the distance between any carbon atom and a substitutional atom in the lattice was less than 1.5 mesh units (eg 1.414 mesh units, or root two) then the absolute coordinates of the two were compared, and atomic jumps that would result in the carbon atom moving away from the vanadium atom penalised with an increment to the activation energy of $10kJmol^{-1}$; this does not bind the carbon atoms permanently to the simulated secondary species, but significantly increase the likelihood that a carbon atom, having reached an atom of a the secondary species, will remain in the locus of its nearest neighbour points rather than resuming a random walk diffusional path.

This has the net effect of lowering the free carbon population by some fraction, as well as reducing carbon mobility within the bulk lattice. Interaction energies of $2.5kJmol^{-1}$, $5kJmol^{-1}$, $7.5kJmol^{-1}$ and $10kJmol^{-1}$ have been simulated to see how this affects the behaviour of the aging model. In these runs, at 5wt.ppm the maximum the achievable yield stress has been normalised to 32MPa, and in the runs at 10wt.ppm free carbon the maximum achievable yield stress has been normalised to 35MPa to isolate the retarding effect to the secondary species rather than differences in the bake hardening response of the grade. The interaction energy giving the most similar match in behaviour to the observed effect of the secondary interacting species has then been re-plotted with the maximum achievable yield stress equal to the bake hardening response of steel two in the appropriate annealed condition.

7.4.2. Accelerated Aging Results for the Bortz-Kalos-Liebwitz Algorithm Using the Initial Material Configuration

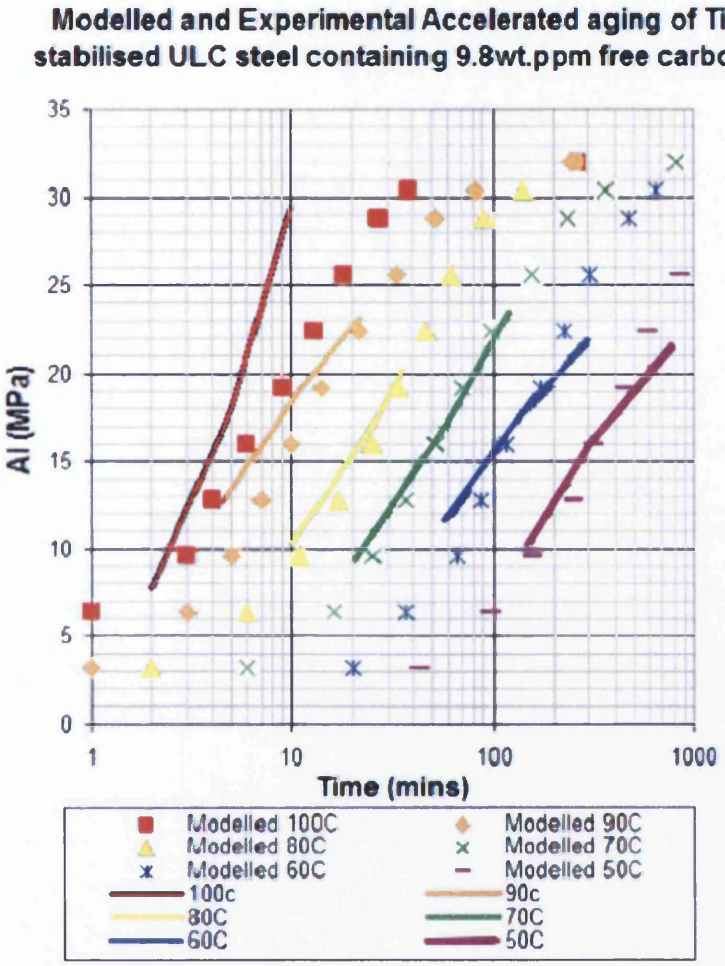

Figure 7.9 Modelled accelerated aging data compared with partial aging traces produced for steel one (Ti only) over the temperature range 50°C to 100°C generated by a variant of the BKL-KMC algorithm based on the initial configuration of significant features in the modelled volume.

Figure 7.9 shows a good match between the predicted and measured aging response of the steel grade between the temperatures 50°C and 80°C, with the simulation accuracy dropping off at higher temperatures.

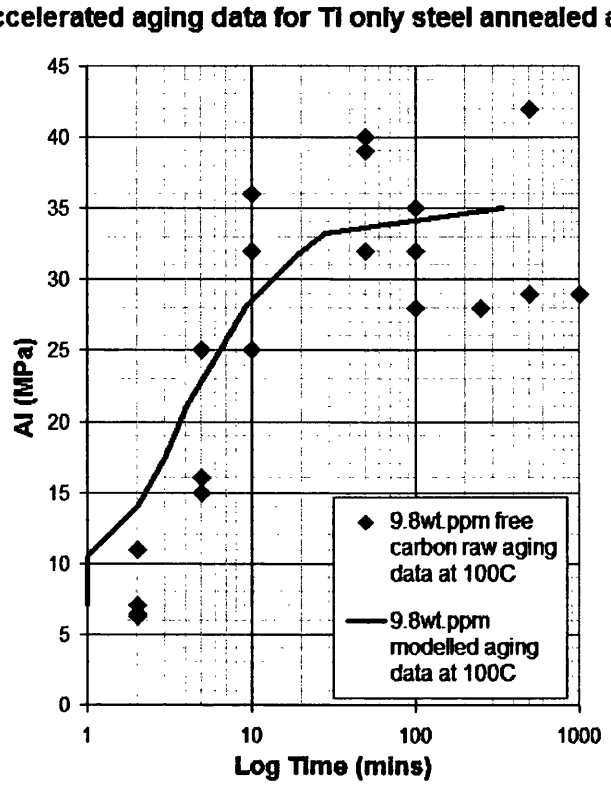

Figure 7.10 A comparison of raw accelerated aging data for steel one (Ti-Only) annealed at 880°C to contain 9.8wt.ppm free interstitial carbon, aged at 100°C, and modelled data for the same aging condition generated by a variant of the BKL-KMC algorithm based on the initial configuration of significant features in the modelled volume.

Figure 7.10and Figure 7.11 show the quality of the fit of the predicted aging curves at 100°C to the raw data produced by performing accelerated aging tests on steel one (Ti-Only) following annealing cycles liberating 5.5wt.ppm and 9.8wt.ppm of free interstitial carbon.

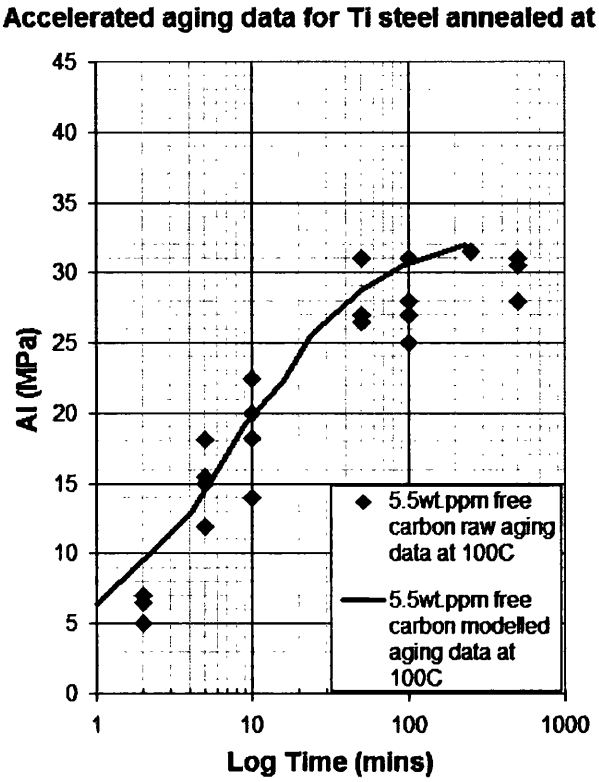

Figure 7.11 A comparison of raw accelerated aging data for steel one (Ti-Only) annealed at 880°C to contain 5.5wt.ppm free interstitial carbon, aged at 100°C, and modelled data for the same aging condition generated by a variant of the BKL-KMC algorithm based on the initial configuration of significant features in the modelled volume.

Figure 7.12 to Figure 7.14 show the match between the isochronal aging behaviour of Steel one as measured during accelerated aging at 100°C and as modelled using the novel BKL program. The difference between the predicted and modelled result is of the order of 10%, with the modelled result being consistently higher

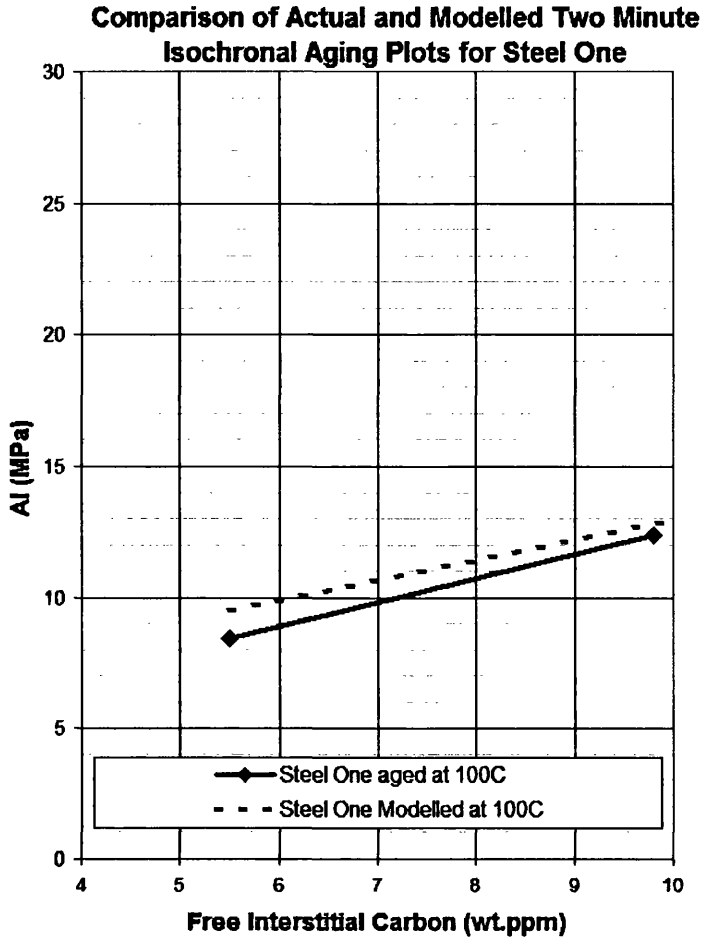

Figure 7.12 A comparison of the two minute isochronal aging behaviour of steel one (Ti-only) aged at 100°C and the modelled behaviour generated using a variant of the BKL-KMC algorithm based on the initial configuration of significant features in the modelled volume.

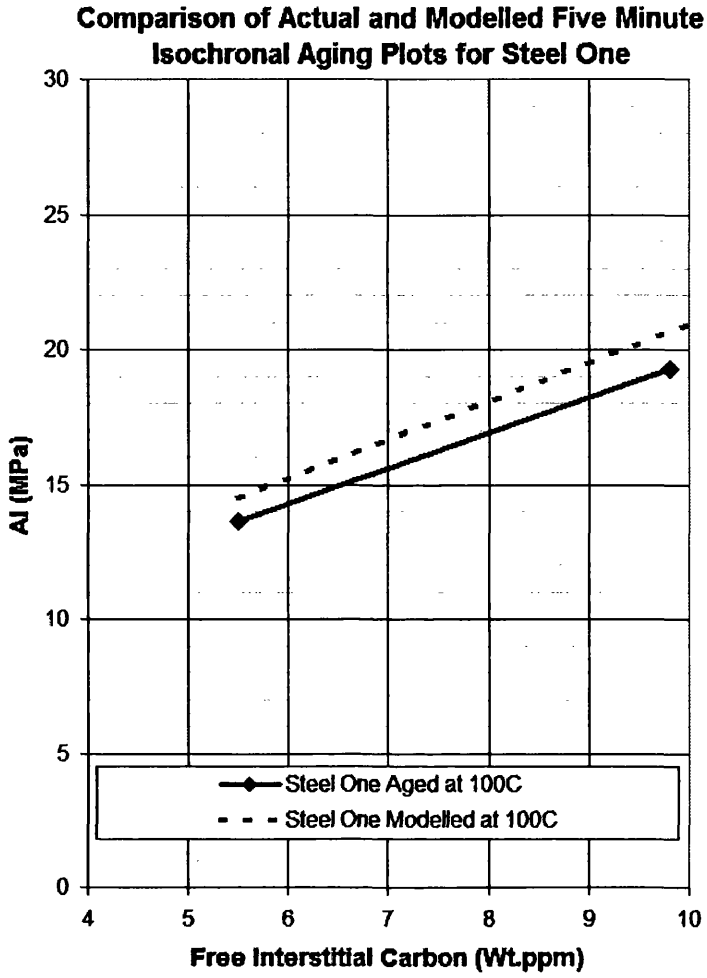

Figure 7.13 A comparison of the five minute isochronal aging behaviour of steel one (Ti-only) aged at 100°C and the modelled behaviour generated using a variant of the BKL-KMC algorithm based on the initial configuration of significant features in the modelled volume.

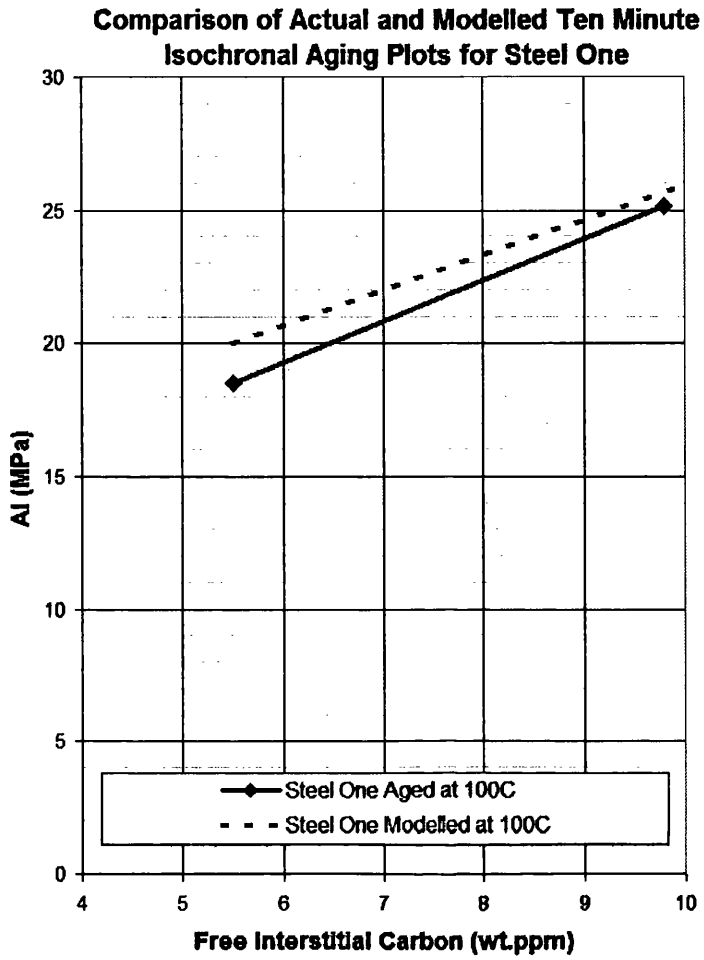

Figure 7.14 A comparison of the ten minute isochronal aging behaviour of steel one (Ti-only) aged at 100°C and the modelled behaviour of the same condition generated using a variant of the BKL-KMC algorithm based on the initial configuration of significant features in the modelled volume.

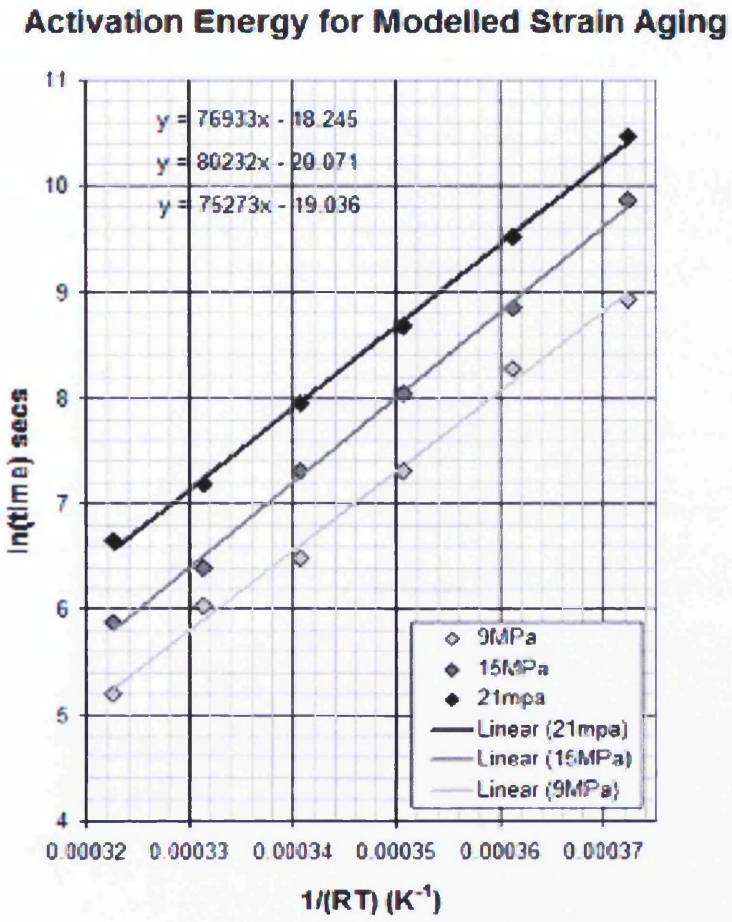

Figure 7.15 Determination of the modelled Arrhenious activation energy for a variant of the BKL-KMC algorithm based on the initial configuration of significant features in the modelled volume, using data taken from Figure 7.9

Figure 7.15 shows the calculated activation energy for the strain aging process, as predicted by the computer model, to be in the region of 75-80kJ/mol, and to follow a straight line relationship described by an Arrhenius type equations.

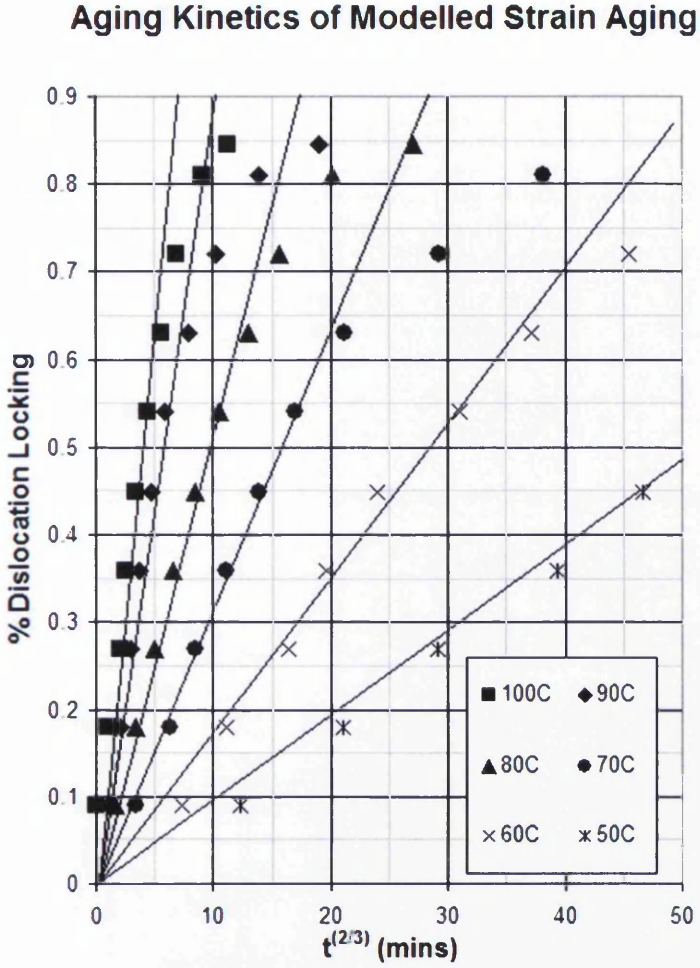

Figure 7.16 A demonstration of the aging kinetics of BKL-KMC algorithm simulating strain aging in the temperature range 50°C to 100°C.

Figure 7.16 shows the model to obey $t^{2/3}$ aging kinetics at all aging temperatures in the range 50°C to 100°C up to 60% dislocation locking.

Figs to 7.17-7.19 .show the effect of the secondary retarding species on the aging kinetics of the modelled steel using 850wt.ppm of secondary interacting species at an aging temperature of 100°C. There is a clear reduction in the isochronal aging

response of the modelled material as a result of the addition of the secondary species when using a 10kJmol^{-1} interaction energy

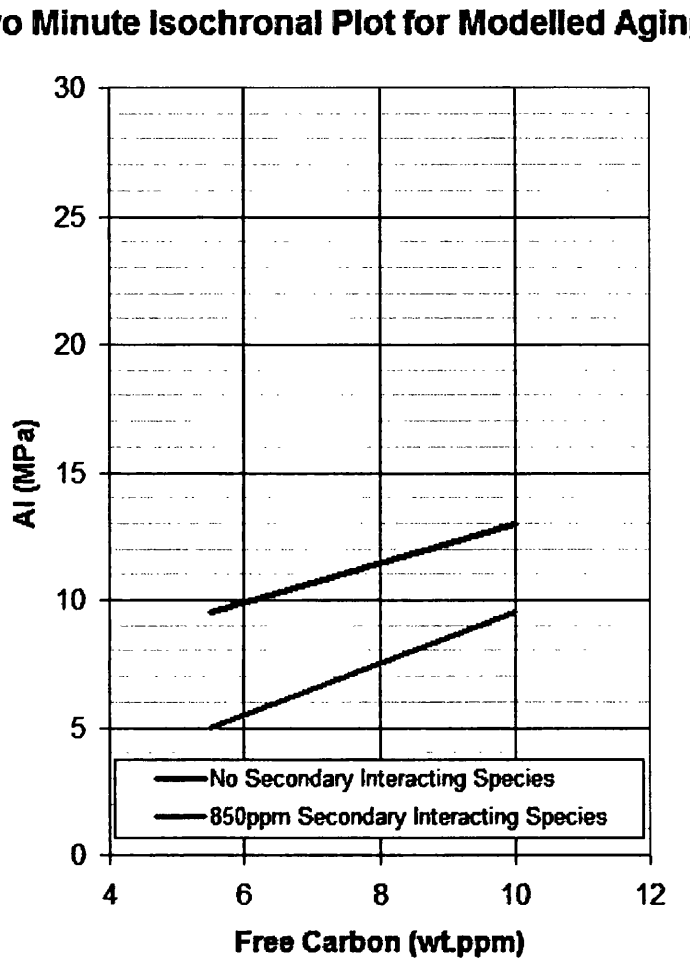

Figure 7.17 A comparison of the modelled isochronal aging behaviour of Steel one (Ti-only) and steel two (Ti-V dual stabilised) after two minutes, assuming stabilisation occurs by a direct nearest neighbour interaction of magnitude 10kJmol^{-1}

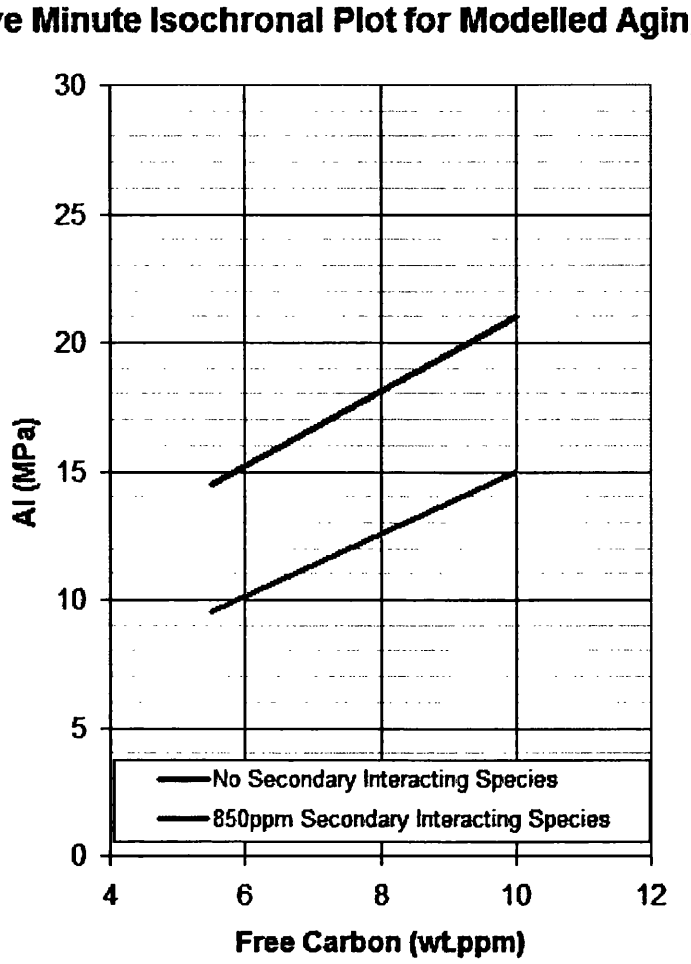

Figure 7.18 A comparison of the modelled isochronal aging behaviour of Steel one (Ti-only) and steel two (Ti-V dual stabilised) after five minutes, assuming stabilisation occurs by a direct nearest neighbour interaction of magnitude 10kJmol^{-1}

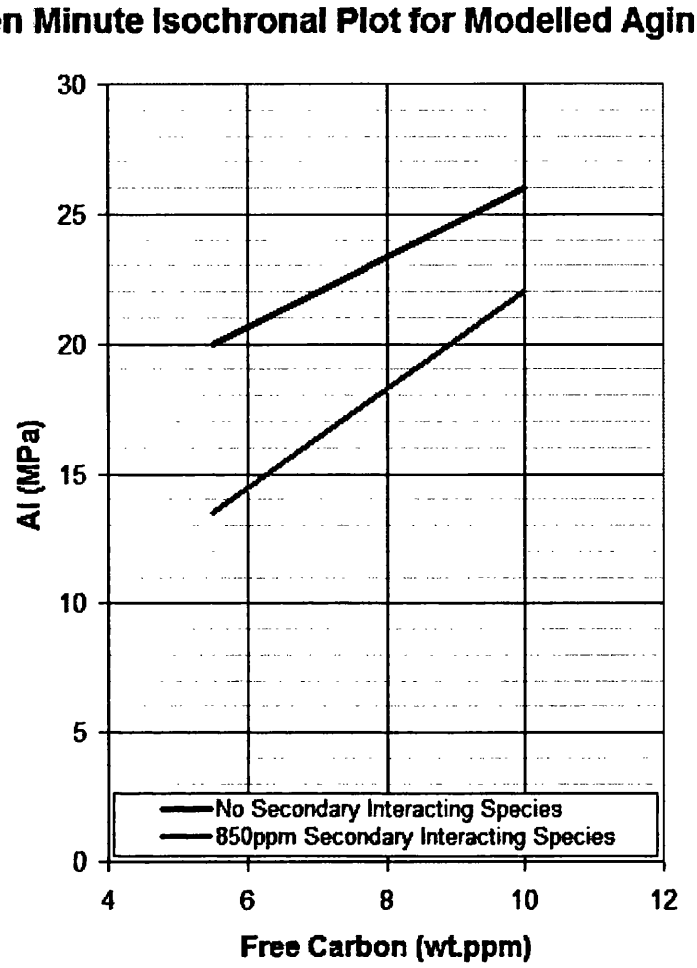

Figure 7.19 A comparison of the modelled isochronal aging behaviour of Steel one (Ti-only) and steel two (Ti-V dual stabilised) after ten minutes, assuming stabilisation occurs by a direct nearest neighbour interaction of magnitude 10kJmol^{-1}

For the two minute and ten minute isochronal aging data the aging responses of the two modelled steels appear convergent with increasing levels of free carbon. The aging responses of the steel modelled with and without 850wt.ppm of a secondary interacting species vary by 52% at 5wt.ppm free carbon, and by only 27% at 10wt.ppm free carbon. After five minutes of simulated aging the difference in response is 33% at 5wt.%free carbon and 26% at 10wt.% free carbon. Similarly, at

ten minutes the aging responses vary by 30% at 5wt.ppm free carbon, and by only 15% at 10wt.ppm free carbon.

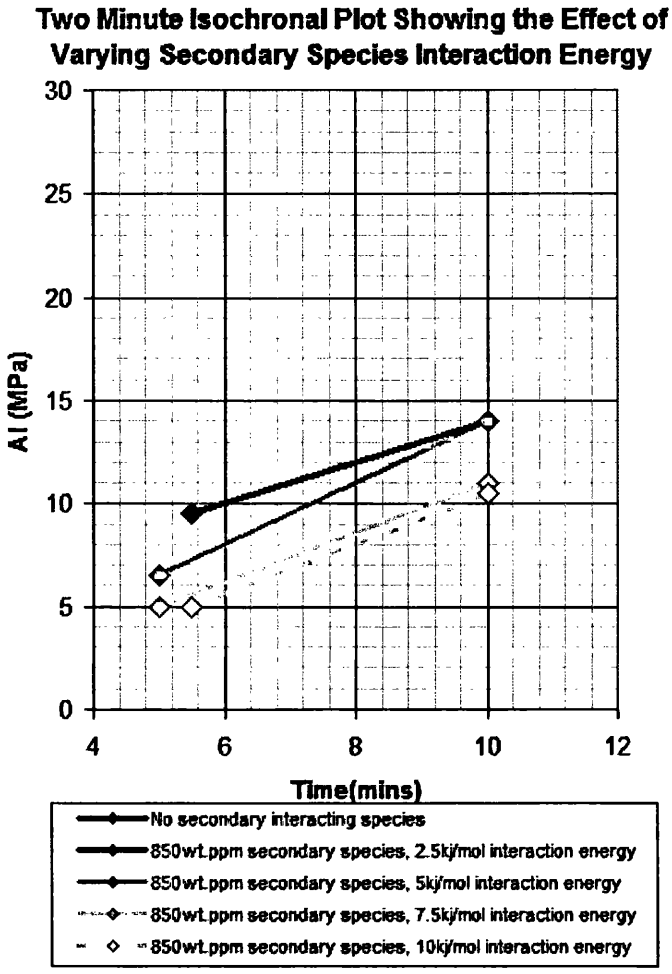

Figure 7.20 A comparison of the modelled isochronal aging behaviour of Steel one (Ti-only) and steel two (Ti-V dual stabilised) after two minutes, assuming stabilisation occurs by a direct nearest neighbour interaction of magnitude 2.5kJmol^{-1}, 5kJmol^{-1}, 7.5kJmol^{-1} and 10kJmol^{-1}

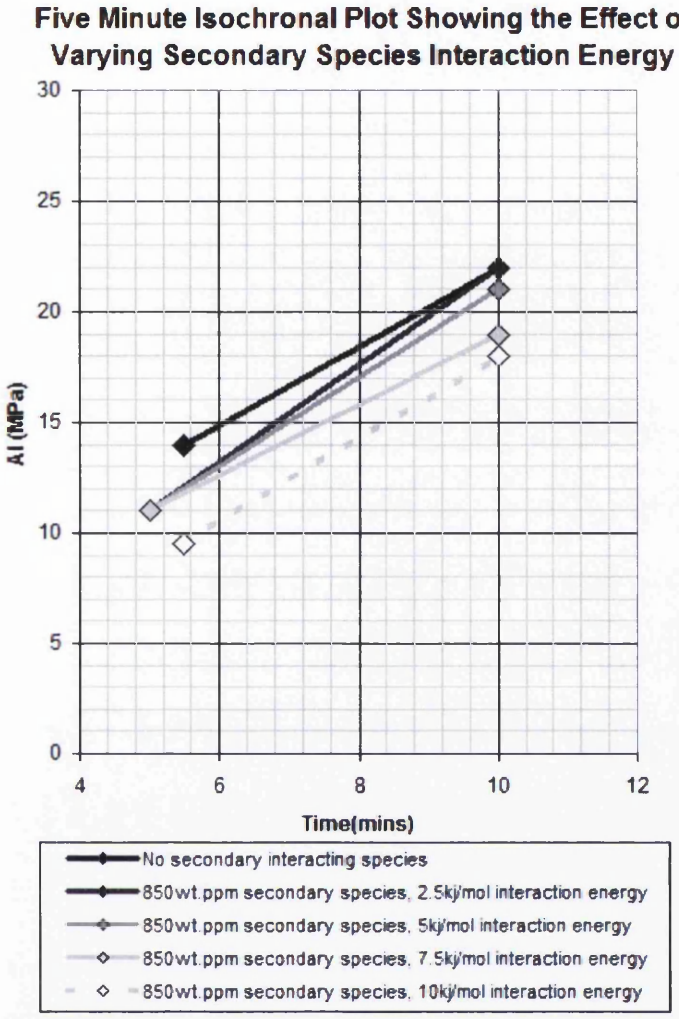

Figure 7.21 A comparison of the modelled isochronal aging behaviour of Steel one (Ti-only) and steel two (Ti-V dual stabilised) after five minutes, assuming stabilisation occurs by a direct nearest neighbour interaction of magnitude 2.5kJmol^{-1}, 5kJmol^{-1}, 7.5kJmol^{-1} and 10kJmol^{-1}

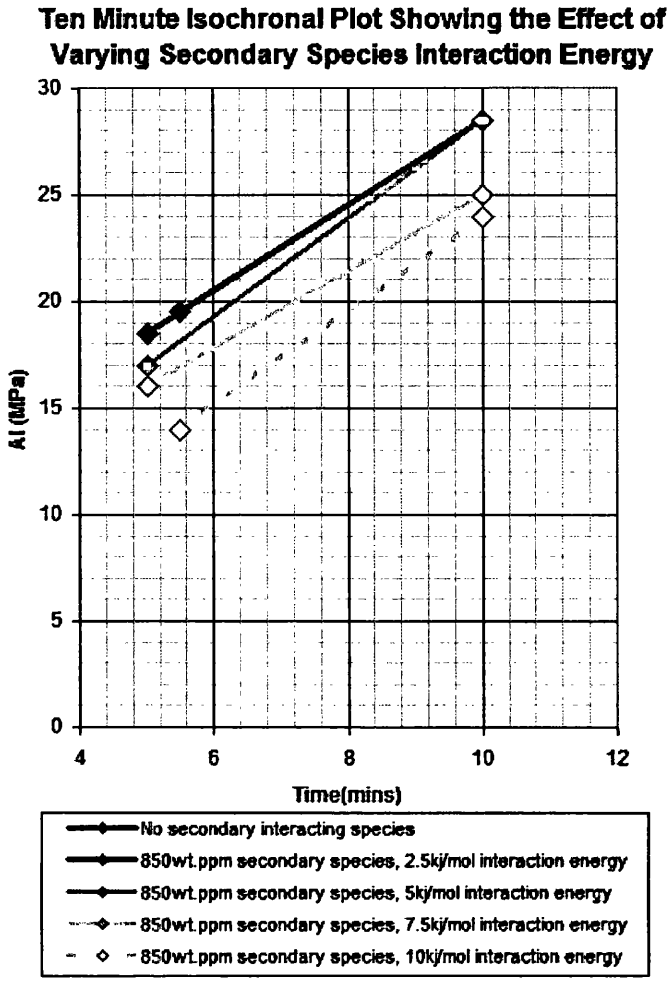

Figure 7.22 A comparison of the modelled isochronal aging behaviour of Steel one (Ti-only) and steel two (Ti-V dual stabilised) after ten minutes, assuming stabilisation occurs by a direct nearest neighbour interaction of magnitude 2.5kJmol^{-1}, 5kJmol^{-1}, 7.5kJmol^{-1} and 10kJmol^{-1}

Figure 7.20-Figure 7.22 show the effect of variation of the nearest neighbour interaction energy assumed by the model. As the interaction energy falls from 10kJmol^{-1} to 2.5kJmol^{-1} the level of the retarding effect shown in the isochronal plots is reduced. At all interaction energies the retarding effect is more pronounced for runs performed modelling 5wt.ppm free carbon and decreases, in percentage terms, with increasing carbon levels.

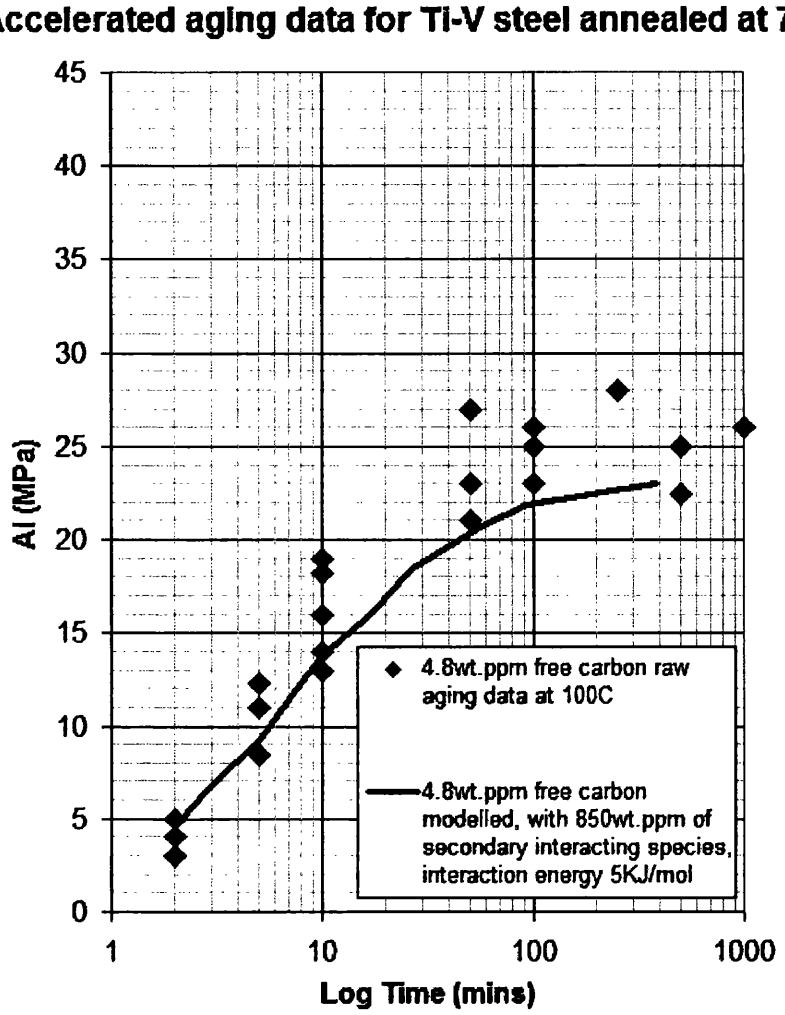

Figure 7.23 A comparison of raw accelerated aging data for steel two (Ti-V-Only) annealed at 740°C to contain 4.8wt.ppm free interstitial carbon, aged at 100°C, and modelled data for the same aging condition generated by a variant of the BKL-KMC algorithm based on the initial configuration of significant features in the modelled volume, with 850wt.pmm secondary interacting species and an assumed interaction energy of 5kJmol^{-1}, normalised to the bake hardening response of the steel

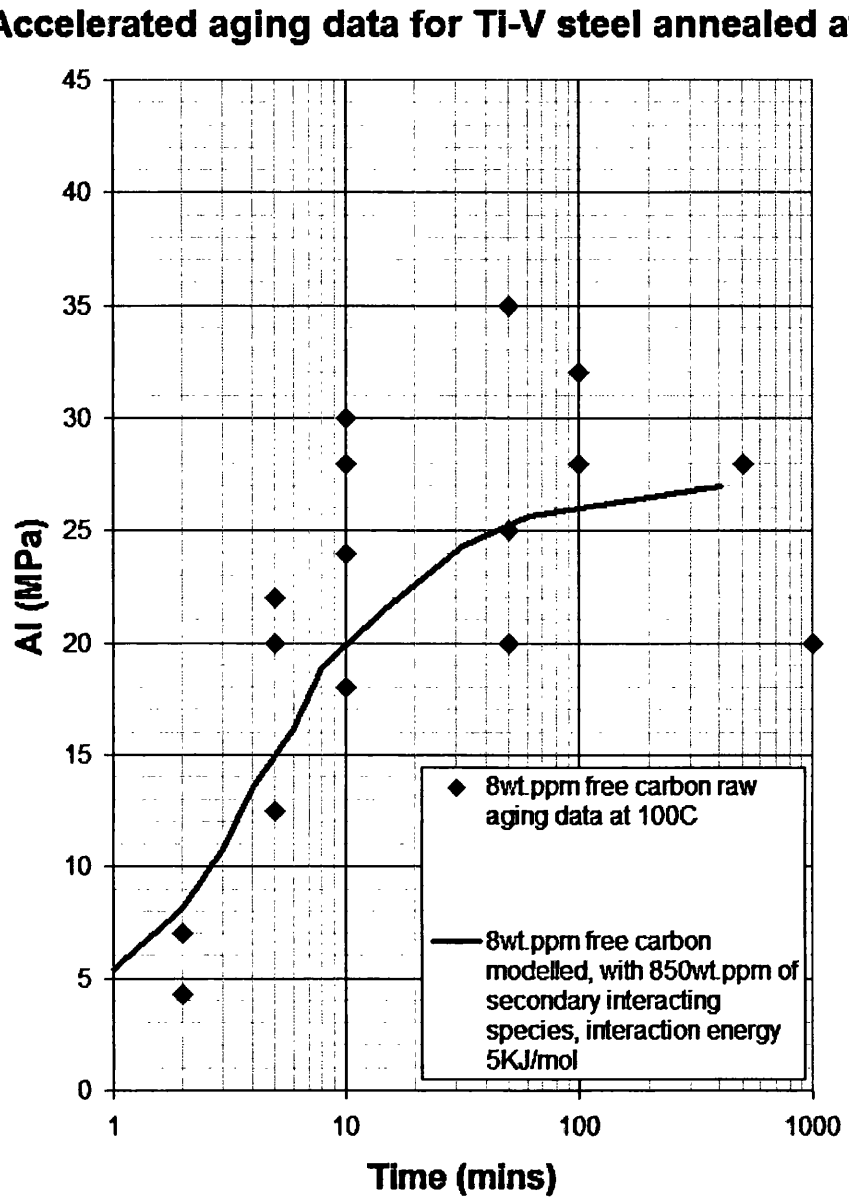

Figure 7.24A comparison of raw accelerated aging data for steel two (Ti-V-Only) annealed at 860°C to contain 8wt.ppm free interstitial carbon, aged at 100°C, and modelled data for the same aging condition generated by a variant of the BKL-KMC algorithm based on the initial configuration of significant features in the modelled volume, with 850wt.pmm secondary interacting species and an assumed interaction energy of 5kJmol^{-1}, normalised to the bake hardening response of the steel

Figure 7.23 and Figure 7.24 show a comparison between raw aging data produced by aging steel two at 100°C following annealing to liberate 4.8wt.ppm and 8wt.ppm of free interstitial carbon respectively, and modelled data that has been normalised to the bake hardening response of the grade thus encompassing both retarding effects of secondary alloying species and the reduction observed in the maximum achievable yield stress increase in section 4.4. Figure 7.23 and Figure 7.24 show a agree with the raw aging data up to 80% of completion, falling entirely within the scatter band of the raw data, but in both instances the maximum aging response produced through bake hardening under predicts the maximum aging response attained in the 100°C accelerated aging experiments.

7.5. Variable Strain Fields

There are two phenomena regarding strain aging that potentially require the use of a variable strain field around key features for accurate modelling. Firstly there is the formation of pre-precipitate clusters prior to the nucleation of small coherent precipitates following Cottrell locking. The current mechanism for dislocation locking, in the BKL and LAKMC models, makes use of a fixed template for dislocation interaction energy. In the BKL algorithm this does not represent a significant problem as, upon arrival of the first carbon atom at the core of the simulated dislocation it is considered to be 'locked' and the next dislocation in the simulation initiated. In the LAKMC model, however, the use of this fixed template essentially makes the dislocation interaction fields an unlimited carbon sink – if several hundred dislocations are being modelled simultaneously there will naturally be a significant body of simulated time between the locking of the first and last. During this time the

only limit to the number of carbon atoms the strain field around the dislocation can take up is the inability of the atoms to co-inhabit sites, and the limited number of sites in which the variation in interaction energy is significant.

Secondly, the evidence provided through this programme of work is not sufficient to state categorically whether the retardation of strain aging is caused by direct dipole interactions with a secondary substitutional species, or through an interaction with coherent precipitates in the lattice. Evidence has been generated supporting both standpoints in the form of TEM data and modelled results. In order to model the retarding effect as a function of the strain fields around coherent precipitates it is necessary that these precipitates act as limited carbon sinks.

Carbon atoms have a diameter of approx 80pm. Given the cell parameter for BCC ferrite (287pm), the size of the octahedral site can be calculated. The most closely packed direction in the BCC unit cell lies along the body diagonal; using Pythagoras theorem (that the square of the length of the hypotenuse of a right angled triangle is equal to the sum of the squares of its other two sides) it can be easily determined that the body diagonal of a cubic unit cell has a length of $\sqrt{3}$ times the cell parameter, or 497pm. This can be used to calculate the atomic radius of ferrite as the close packed direction {1,1,1} contains two complete iron atoms. This gives an atomic diameter of 2.485Å,. Returning to the cell parameter of 2.87Å, this gives an octahedral site diameter of 0.38Å, or a misfit of around 50%.

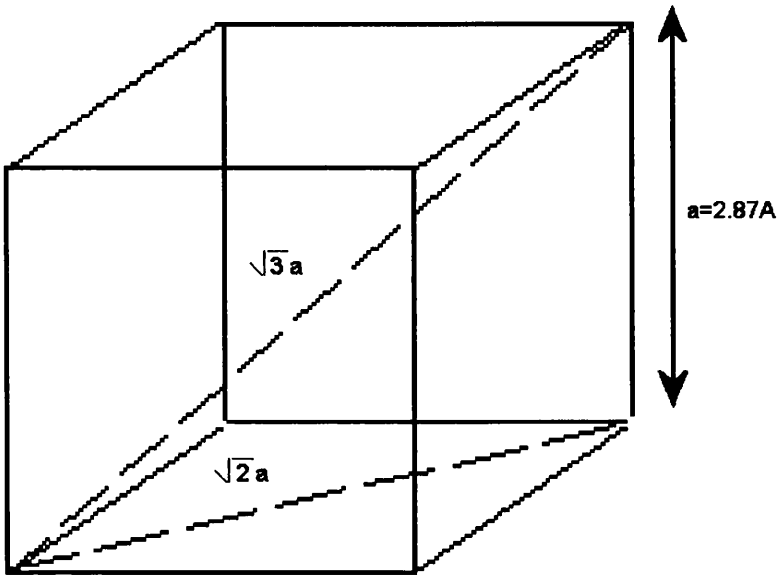

Figure 7.25 - Construction for octahedral site size in BCC ferrite

It is this misfit that results in an interaction between free interstitial carbon atoms and dislocations, and potentially coherent precipitates – the atoms fit into those sites having lower misfit strain energy than elsewhere in the BCC lattice, as these sites are enlarged. However, due to their lattice misfit, the presence of carbon atoms can be expected to change shape of the potential field around a dislocation. The aim of this stage in the modelling was to account for those interactions, and establish whether, in the simulation, they would result in regular ordering of carbon atoms around the dislocation core, and the eventual negation of the field.

An attempt has been made to model a dynamic dislocation using a Laplace equation to describe the potential field. The BKL simulation described in section 7.3 was

applied, but the kinetics of locking ignored, the model output describing only the shape of the potential field throughout the dislocation locking event.

$$\frac{\delta^2\phi}{dx^2}+\frac{\delta^2\phi}{dy^2}=f(x,y) \qquad 7\text{-}7$$

The precise rate of energy drop differs between the KMC dislocation model and a Laplace or Poisson equation potential field. However, the general shape of the interaction field is the same. The BKL KMC model was allowed to progress, but on each iteration a comparison was made between the location of all carbon atoms in the simulation and the position of the core of the strain field, limited by Soenen et al's criteria (equation 7-4) [57] allowing a minimum 10% variation in jump frequency.from the normal jump frequency.

Carbon atoms were given a misfit strain energy of 10kJmol^{-1} with reference to the strain field. If the location check determined that a carbon atom fell within the interaction region a subroutine was launched using an iterative finite difference solver to find the equilibrium energy values in the field, taking into account the additive term for the carbon atom. The finite difference solver used central difference theorem including the effect of nearest and next nearest neighbour cells, and the iterative solver was driven by reducing the maximum change in value occurring at any location in the lattice between successive sweeps of the central difference solution.

On any iteration of the BKL algorithm on which a carbon atom changed its location within the strain field the shape of the field was recalculated, and a text file output that could be processed by a post processor to generate a graphical representation of its shape was produced.

7.5.1. Variable strain field results

Figure 7.26 shows the correlation between the between the strain field produced using the static model applied in the KMC algorithm. While the Poisson potential field does not exactly match the rate of drop off in interaction energy around the dislocation from the KMC model the shape of the strain fields around the dislocation cores match in terms of shape.

Figure 7.27 shows the effect of interacting carbon atoms with the variable strain field around the Poisson dislocation. In the top left of the figure the effect of two carbon atoms interacting with the strain field in the tensile region below the interaction feature can clearly be seen. As the locking model progresses there is a significant reduction in the magnitude of the variable strain field as the first carbon atom is drawn into the site of maximum interaction energy directly below the strain field core (centre right). At the bottom of the figure the arrival of a second carbon atom below the core can be observed, this atom lying directly beneath the first. The strain field is, at this point, essentially negated and no further carbon atoms were drawn to the core of the interaction field.

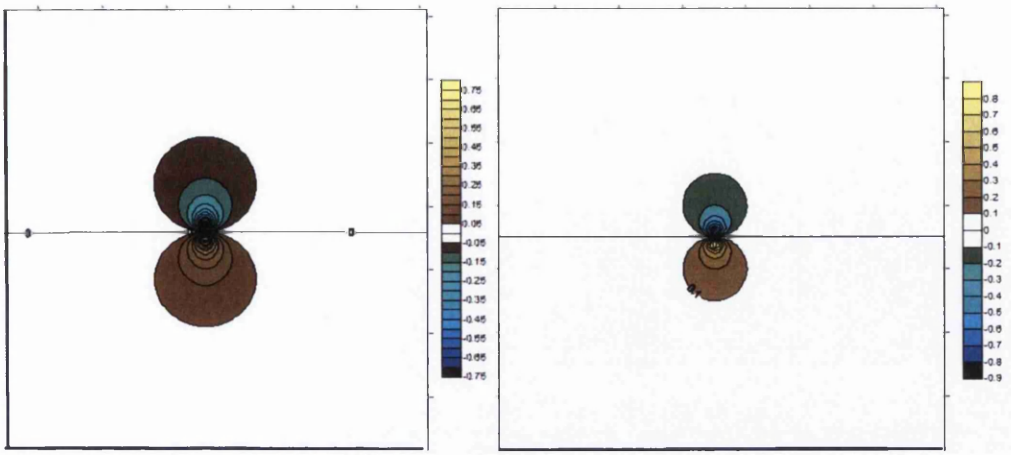

Figure 7.26 - Laplace Potential Field (left) against existing KMC model (right)

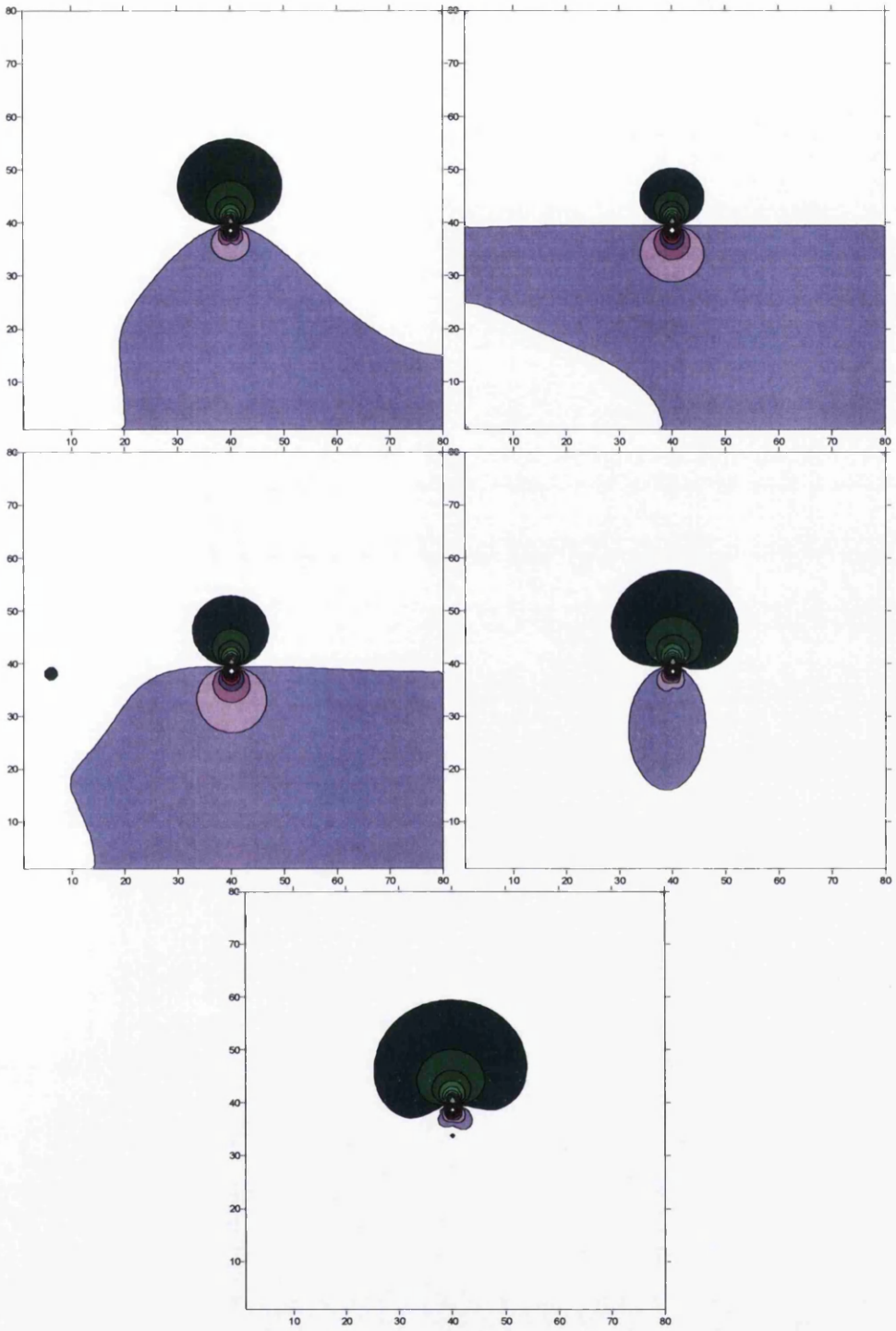

figure 7.27 a qualitative demonstration of the use of poisson fields to simulate a variable strain field, with free carbon atoms during kmc simulation

CHAPTER EIGHT

MODELLING DISCUSSION

8. MODEL DISCUSSION

8.1. Locally activated Kinetic Monte Carlo Algorithm discussion

Figure 7.3 shows the simulated aging curves to fall within 10%, in terms of total aging response as a function of time, of those generated in the experimental work of other authors [25, 40, 73], and suggests that mesh size has an observable effect on the performance of the simulation technique. However, because the carbon atoms are placed randomly at the start of the simulation run it may be that averaging the predicted aging behaviour over a large number of runs at one condition may reduce or eliminate this effect; on a larger grid there is more scope for rogue results where large areas of the simulation are relatively over, or under, populated. This type of effect may also account for the increased scatter observed on the $22{,}000^2$ element result when compared to the $15{,}000^2$ element result.

Figure 7.4 shows mesh shape to have no discernable effect on the technique in the range over which simulations were run. The minimum mesh width used was 2,000 elements, with an average dislocation spacing of around 1000 mesh elements in all trials; as a periodic boundary condition was used it is unsurprising that the mesh shape had little effect on the simulation result, and it seems likely that the effect will be negligible provided the mesh width is larger than the average dislocation spacing; if this condition is not met, the dislocation density would be artificially increased as the distance between each dislocation and itself would be shorter than the average dislocation spacing. In the region of 1% to 5% prestrain it has been shown that

dislocation density, ρ, varies between roughly $1x10^{13}$ and $6x10^{13}m^{-2}$ (Fig. 9) [106]; accepting that average dislocation spacing can be taken as $\rho^{-0.5}$ [57] this corresponds to a range from 1100 to 500 unit cells. It is therefore suggested that thin strip simulations should be performed with a mesh width in excess of this upper value (2200 mesh elements in the current model).

From Figure 7.5, the technique seems suited for the simulation of changing carbon content, though the range covered in this investigation was limited. The accuracy of the model seems sensitive to temperature, performing significantly less well at 373K than in trials at 323K. This effect, and model alterations with which it can be prevented, are the subject of ongoing simulations.

The demonstration shown in Figure 7.6, while highly simplified, illustrates that this technique may have potential for modelling the effects of carbide formers such as Vanadium in solution, which have been suggested as having a delaying effect on low temperature strain aging when added in sufficiently large quantities [107].

Locally activated Kinetic Monte Carlo seems to be a tool well suited to the modelling of aging processes; however, the necessity of modelling the entire of the area of interest simultaneously to capture the extremes of behaviour leads to very large meshes and long simulation times. The increase in run time does not vary linearly with mesh size, as each additional carbon atom introduced to the simulation must be checked against each dislocation present.

At 10,000 elements squared this equates to 278 dislocations (assuming 5% prestrain) and 1167 carbon atoms at 10wt.ppm concentration, or 325,000 location checks at each time step of the simulation. At 20,000 elements squared this equates to 493 dislocations and 4667 carbon atoms, or 2,300,000 location checks, seven times as many. While this effect is mitigated through the use of the divide and conquer method described in section 7.2.2, a more efficient algorithm is clearly beneficial, especially considering the poor performance of the algorithm with regard to variations in temperature

8.2. Average Condition BKL Discussion

The Bortz Kalos Liebowitz simulation presented in section 8.2 was intended to get around the time constraints presented by the Locally Activated Kinetic Monte Carlo model in section 8.1. An attempt was made to reduce run times by modelling a significantly smaller grid, whilst taking into account those factors that would affect the aging response, essentially the dislocation density and population of free carbon atoms remaining in solution.

The aging response in this simulation was derived entirely from the average properties of the material following a given period of time; once one dislocation had been locked the average dislocation density was assumed to have changed, and this was applied as an incremental change to the size of the grid for all subsequent locking events. Similarly, annihilated carbon atoms were reintroduced at the simulation boundary between locking events to retain the average population of free carbon atoms as expected, accepting that those carbon atoms that had been drawn into the dislocation interaction zone were essentially tightly bonded as pre-precipitate clusters.

Figure 7.7 shows a match between the observed and modelled behaviour during the middle stages of aging. A much poorer fit between the two data sets is found at the beginning and end of aging, where extremes of behaviour are observed; the model does not allow for extreme variations in carbon population or in the initial placement of carbon atoms, as the locations of carbon atoms are conserved between simulation

runs. As such the model tends to over predict the time required to achieve a given level of aging in the initial stages (below 50% completion) and under predict the required time in the latter stages.

The JMAK aging kinetics, shown in Figure 7.8, clearly show that the process being modelled in this simulation is not the observed process. However, the JMAK kinetic response at 50% completion of aging is very similar between the simulated and measured aging data (the point at which the value of ln(-ln(1-W) is approximately –0.37). This can also been seen in the accelerated aging data through a comparison of the times required to achieve an aging response of roughly 16MPa.

Following this work a further simulation trial was warranted. A model based on the average expected behaviour of the model well reproduced the behaviour during the middle stages of aging, but tended to over predict early aging times, and under predict the time required for the full formation of Cottrell atmospheres to occur.

The nature of the time step, with the zero time point being redefined at the onset of locking of each dislocation as a fraction of the number of locking events occurring, should have served to push early iterations of the algorithm toward very short times as the zero time was near to the zero time of the overall simulation, Later iterations should similarly have been pushed toward the extreme end of the full aging time, as the initial time at the onset of the algorithm would have been near to the maximum time achieved for all the locking events to that point. For the bulk of results to fall within a narrow time frame, focussed around the middle of atmosphere formation, it would be necessary for all locking events to have taken essentially the same length

of time – maintaining the locations of the carbon atoms relative to the dislocation core while varying the mesh size and carbon population does not generate extremes of condition, but rather serves to maintain the average condition for the duration of the simulation.

8.3. Initial Condition BKL Discussion

From Figure 7.9, the model appears to predict rates of strain aging in Ti stabilised Ultra Low Carbon steel with a high level of accuracy. This accuracy drops off with increasing temperature. However, as samples were not quenched on removal from the aging furnace it is likely that aging will have continued to some extent following their removal, this effect being more marked at higher temperatures where diffusional processes are considerably faster.

Accepting the tendency of the model to under predict the aging response at higher temperatures where there is no quench in place, the trend of increasing time to achieve a given aging response with decreasing carbon content is well reproduced in Figure 7.10 and Figure 7.11. In the case of the 9.8wt.ppm free carbon steel the extent to which the aging response is under predicted is more severe (≈7MPa). The maximum yield stress increase typically attributed to the formation of Cottrell atmospheres alone is in the region of 30MPa. The raw aging data for the steel containing 9.8wt.ppm of free carbon shows individual points with aging responses as high as 40MPa suggesting a secondary aging process, precipitate formation, is also taking place. As the model only accounts for the formation, by diffusion, of Cottrell atmospheres, any additional strength increase due to a secondary process will not be represented.

Figure 7.12 to Figure 7.14 show a strong correlation between the isochronal aging plots produced using the accelerated aging data generated through the experimental

programme and the modelled data at the same conditions; additionally in the initial stages of aging, up to around 50% completion, $t^{2/3}$ kinetics are produced by the model as described by Cottrell and Bilby [34](Figure 7.16). Additionally, the aging behaviour can be described using an Arrhenius type relationship producing a straight line plot, with an activation energy in the range 75kJ/mol – 80kJ/mol (Figure 7.15). The process is thermally activated, as strain aging has been shown to be by Rashid [15] and Tanikawa et al [102], though the activation energy displayed by the model is lower than that predicted for low temperature aging by Tanikawa et al (83kJ/mol) and significantly lower than the $90kJmol^{-1}$ found in the kinetic study performed in the generation of validation data.

With regard to the validation data generated the model can be seen to match the experimental data for aging conditions ranging in free carbon composition from 5-10wt.ppm free interstitial carbon, and over the temperature range 50°C to 100°C. Without the addition of a secondary interacting species typical run times were of the order of thirty minutes.

The difference in behaviour on the addition of a secondary interaction species at a high level of concentration is clear, with a significant retarding effect visible in the two, five and ten minute isochronal aging plots (Figure 7.17 to Figure 7.19). With increasing free carbon the ability of the secondary species to act as an efficient carbon sink is reduced, and the percentage difference in the isochronal aging response with and without the secondary interacting species drops off as the carbon level increases from 5-10wt.ppm, similar to the behaviour of the experimental grade.

The retarding effect of the secondary interaction is in fact two fold. Firstly, the reduced probability of atomic jumps that result in a free carbon atom jumping away from a secondary atom effectively reduces the effective free carbon population that is available to move to the dislocation core. Secondly, as the BKL time step is tied to the sum of the frequencies of all events occurring within a given subset of possibilities, the presence of these low frequency results within the subset of probabilities relating to a given set of moves will increase the overall time step of the simulation, having an additional retarding effect alongside the reduction in the carbon population; there are fewer carbon atoms able to move freely following a random walk diffusional path, and the average time required for a diffusional event to occur is increased.

Varying the interaction energy has had a distinct effect on the simulated aging results; as the interaction energy for nearest neighbour interactions with the secondary species drops from $10kJmol^{-1}$ to $2.5kJmol^{-1}$ the retarding effect of the secondary species can been seen to drop off, and the retarding effect at higher free interstitial carbon contents becomes negligible (Figure 7.20 to Figure 7.22) As the interaction energy drops the likelihood that carbon atoms will remain tightly bound as dipoles decreases; at $10kJmol^{-1}$ the frequency of atomic jumps moving a carbon atoms away from a secondary interacting atom is 4% of the normal jump frequency. At $2.5kJmol^{-1}$ this value has risen to 45% of the normal jump frequency. As the likelihood of a particular event occurring within the BKL algorithm is proportional to its frequency, it is obvious that at higher interaction energies the efficiency of the secondary species in tying up the carbon population is greatly reduced.

Comparing Figure 7.20 to Figure 7.22 the results produced for the secondary interaction potential of 5kJmol^{-1} closely match the trends displayed in the validation data for the actual behaviour of steel two (Ti-V dual stabilised) upon which the condition of 850wt.ppm of secondary interacting species with an atomic weight of 52 was based. Carrying these results through to the accelerated aging traces for steel two Figure 7.23 and Figure 7.24, the predicted curves show a close match with the actual aging data up to 80% of dislocation locking.

The BKL model based on initial conditions in the steel follows the expected $t^{2/3}$ kinetics for strain aging of carbon steels. Simulations reproducing the condition of the titanium only steel samples following annealing show a very strong correlation with actual test data produced for the purposes of validation, when the model is initialise using the actual diffusional coefficients and lattice parameter for the iron carbon system and dislocation pressure field.

From this stand point the model serves as a validation of the current understanding of dislocation locking phenomena and provides a useful tool for predicting strain aging of ultra low carbon steel with an equivalent level of accuracy to existent techniques.

The extension of the model to include a secondary species of substitutional atoms in solution shows a novel use of the KMC technique. While the experimental programme has not identified with certainty the mechanism by which the retardation of strain aging occurs, the demonstration in figures 7.17 to 7.24 shows that a system relying on direct dipole interactions between free interstitial carbon atoms and

substitutional atomic species can be simulated using the Bortz-Kalos-Liebwitz algorithm as described in section 7.4.1

8.4. Modelling results summary

The modelling work performed has shown the existing KMC technique, previously published by Soenen et al [57] to be effective in predicting rates of strain aging in ultra low carbon steels, and robust to changes in carbon content and grid size. The existing KMC model displayed a much lower level of accuracy in predicting accelerated aging curves at 100°C than at 50°C, and was found to be very processor intensive with run times running from several hours, to several days, on a computer having a 3GHz processer and 1Gigabyte of RAM, running no other applications simultaneously aside from the operating system (Microsoft Windows XP).

A further attempt to model the initial stages of strain aging, culminating in the formation of Cottrell atmospheres, was produced using the Bortz Kalos Liebwitz algorithm, and focussing on both the average expected features of the structure as aging progressed, and as a result of the initial configuration of these features. It is the understanding of the author that this approach to modelling of strain aging phenomena is novel.

It was found that a BKL KMC algorithm, modelling subsections of a large global array, these subsections being defined by the initial configuration of the material, was able to reproduce aging behaviour of ultra low carbon steels in the free interstitial carbon range 4 to 10wt.ppm free carbon at all temperatures between 50°C and 100°C with solution times of the order of twenty minutes (compared to several hours for the locally activated algorithm).

Furthermore, by the retarding effect of vanadium on rates of strain aging was successfully integrated into the model through the assumption of a nearest neighbour interaction potential

CHAPTER NINE

SUMMARY OF FINDINGS

9. SUMMARY

An experimental programme has been presented displaying the retarding effect of vanadium on rates of strain aging in ultra low carbon steels. With reference to the two current theories regarding such retarding effects, there is evidence within this thesis to defend either proposition – a direct interaction between atomic carbon and vanadium, or an interaction with the strain fields around coherent precipitates.

It has been possible to image strain fields within a heavily vanadium microalloyed steel (0.08wt.% vanadium) produced by nano-scale precipitates following a high temperature anneal and quench. There is also a body of modelled data, produced through a novel application of the Bortz-Kalos-Liebwitz algorithm for Kinetic Monte Carlo simulation, which shows it is possible to reproduce the effect of the vanadium in the validation data through the modelling of a direct atomic interaction.

The model has been presented that seems to reproduce the process of strain aging with a useful level of accuracy as a predictive tool. The kinetics of the model suggest that, functionally, the processes of Cottrell atmosphere formation are being reproduced within current understanding of the processes, and the ability to qualitatively reproducing carbon atom clustering behaviour shows that the model has potential to be extended to include precipitate nucleation effects.

Importantly, simulation times for a complete run of the model take only around twenty minutes with no secondary interacting species, compared to run times of over

six hours in the Locally Activated Kinetic Monte Carlo simulation previously presented [108], and only hours for simulations with secondary interacting species compared to days for the previous model. These times are sufficiently low for the model to have industrial value in the assessment of existing cast chemistries or development of future steel grades; additionally, given the ease with which secondary species can be introduced there is the potential to build up a volume of data on the interaction effects of a number of elements and model the combined effects of more complex alloy systems, and, while the results produced in section 7.5 are purely qualitative, they show the potential of the Poisson equation to be used to model variable strain fields around interacting features such as dislocations or coherent precipitates, as imaged in **Figure 5.19**, which, coupled to a model of precipitate nucleation and growth could allow the technique to be extended to cover the full process of strain aging.

CHAPTER TEN

CONCLUSIONS

10. CONCLUSIONS AND RECOMMENDATIONS

This body of work has resulted in a number of significant conclusions, detailed below.

- Vanadium has been found to have a measurable retarding effect on rates of strain aging in ultra low carbon steels, with free interstitial carbon in the range 4wt.ppm to 10wt.ppm. Combined with the low stability of vanadium carbide relative to titanium and niobium carbides, this finding allows for the development of a family of titanium-vanadium dual stabilised bake hardening steels, in which carbon is liberated through the dissolution of vanadium carbide during annealing. The lower temperatures required for vanadium-carbide dissolution, compared to existing carbides in existing titanium-niobium products, would allow colder annealing cycles, requiring less energy, and hence offering a cost saving. In addition, retarding of aging at ambient temperatures offers a product with an improved shelf life without sacrificing the bake hardening response.

- Evidence has been provided of the existence of coherent vanadium carbide precipitates in titanium-vanadium dual stabilised steel following an anneal and quench. The extent of retardation of strain aging by vanadium appears consistent with an interaction between free interstitial carbon atoms and the strain fields around these coherent precipitates, due to a saturation effect occurring at higher free carbon contents, that would not be expected given a

vanadium-carbon S-I interaction, where the secondary species is present in a heavily super stoichiometric ratio.

- It has been found that Kinetic Monte Carlo, and particularly a novel application of the Bortz-Kalos-Liebowitz algorithm, can be used to simulate the processes occurring during the early stages of strain aging, up to the complete formation of Cottrell atmospheres. The technique developed is able to predict the times required for partial and complete aging, proven over a temperature range from 50°C to 100°C in steels containing from 4wt.ppm free carbon to 10wt.ppm free carbon, with simulation times that are consistent with usage as a desktop tool (tens of minutes).

- It has been shown that the retarding effect of vanadium can be modelled assuming a direct substitutional-interstitial interaction between vanadium and carbon by tailoring the interaction energy, and it is put forward that the retarding effect observed may be produced by a combination of two effects – strain field interaction and dipole formation. Additionally a mechanism is provided by which variable strain fields can be modelled within the KMC framework allowing for future exploitation of this model in reproducing both the retarding phenomenon observed herein, and carbon atom clustering and precipitate nucleation events.

Four experimental compositions were cast and processed for this programme of work, the two discussed herein and a further two, having 0.04wt.%V and 0.12wt.%V respectively, based upon the findings in this thesis. Due to time constraints, it was

not possible to progress the experimental programme on the final two casts, and it is the recommendation of this author that further trials be performed on these to accurately establish the interaction energy values that simulate real behaviour across all feasible compositions. Additionally further work using other substitutional species known to interact with free carbon, such as manganese, could produce a framework in which more complex and industrially relevant steel compositions could be simulated and developed.

Limited trials of a titanium-vanadium steel with a commercial chemistry may be warranted, using annealing cycles that mirror those employed on the Llanwern ZODIAC line and Port Talbot CAPL facility to determine the commercial viability of such a bake hardening product, and its performance in terms of room temperature strain aging when additional complexities are introduced to the chemistry.

Finally, the KMC framework presented has the potential to be extended to cover precipitate nucleation and growth events, that would expand its relevance both to bake hardening, and as a tool for predicting rates of carbon stabilisation in the overaging sections of modern annealing lines. The further development of KMC as a modelling technique to improve the prediction and understanding of kinetic processes reliant on diffusion is recommended to aid in the development of new steel compositions, and suitable processing parameters for these.

CHAPTER TWELVE

REFERENCES

12. References

1. Carle, D. and G. Blount, *The suitability of aluminium as an alternative material for car bodies.* Materials and Design, 1999. **20**(5): p. 267-272.
2. Wallentowitz, H., *Business Briefing: Global Automotive Manufacturing and Technology 2003.* 2003.
3. Cole, G.S. and S.A. M, Materials Characterization, 1995. **35**: p. 3-9.
4. Mordike, B.L.E.T., Materials Science and Engineering A, 2001. **302**: p. 37-45.
5. Henning, F.E., H; Brussel, R; Geiger, O; Krause, W, Reinforced Plastics, 2001(February): p. 24.
6. Mills, A., et al., Reinforced Plastics, 2001(June): p. 46.
7. AISI, *ULSAB-AVC Overview Report*, AISI.
8. Asensio, J., et al., *Ferritic steels.* Materials Characterization, 2001. **47**(2): p. 119-127.
9. Takahashi, M., *Nippon Steel Technical Report No 88.* 2003, Nippon Steel.
10. POSCO, *POSCO cold rolled products catalogue*, POSCO.
11. Silcock, M., et al., *Finite element modelling of metallic tubular crash structures with an explicit code.* Int. J. Vehicle Safety, 2006. **1**(4): p. 292-303.
12. Brown, S.G.R. and N.C. Barnard, *3D computer simulation of microstructure on the cut edge corrosion behaviour of zinc aluminium alloy galvanised steel.* Corrosion Science, 2005. **48**(8): p. 2291-2303.
13. Jones, D.M., J. Watton, and K.J. Brown, *Prediction and validation of through coil final mechanical properties of high strength hot rolled coil using artificial nueral networks.* Journal of Ironmaking and Steelmaking, 2006. **33**(4): p. 315-322.
14. Rashid, M.S., *Strain Aging of Vanadium, Niobium or Titanium-Strengthened High-Strength Low-Alloy Steels.* Metallurgical Transactions A, 1975. **6A**: p. 1265-1268.
15. Rashid, M.S., *Strain Aging Kinetics of Vanadium or Titanium Strengthened High-Strength Low-Alloy Steels.* Metallurgical Transactions A, 1976. **7A**: p. 497-503.
16. Taylor, K.A. and J.G. Speer. *Development of Vanadium-Alloyed, Bake-Hardenable Sheet Steels for Hot-Dip Coated Applications.* in *Mechanical working and steel processing conference.* 1997. Indianapolis; IN: Indianapolis.
17. Taylor, K.A. and J.G. Speer, *Bake hardenable vanadium containing steel and method therof.* 1997, Bethlehem Steel Corporation: USA.
18. Baird, J.D., *Strain Aging of Steel a Critical Review; part I: Practical Aspects (continued).* Iron and Steel, 1963. **1963**(May): p. 326-333.
19. Kurasawa, M., et al., *Age-Hardening Behaviour and Dent Resistance of Bake-Hardenable and Extra Deep-Drawable Steel.* Kawasaki Steel Giho, 1987. **19**(2): p. 119-123.
20. Hirose, Y., et al. *The comparison in dent-resistance between high strength steel with excellent formability and bake-hardenable steel.* in *International Deep Drawing Research Group: Sheet metal forming beyond 2000.* 1998. Genval; Belgium: Helston.
21. Christen, J.L., J. Rubianes, and A. Col. *Bake-Hardening Steels For Automotive Outer Body Panels: Correlation Between The BH Measurement And The Dent Resistance.* in *Advanced body concept & development.* 1997. Stuttgart; Germany: Automotive Technology Group Inc.
22. McCormick, M.A., et al. *Effect of Steel Strengthening Mechanisms on Dent Resistance of Automotive Body Panels.* in *Steel sheet and steel bar products and processing for automotive applications.* 1998. Detroit; MI: Sae.
23. Gehm, R., *GM Goes global with materials*, in *Automotive Engineering International Magazine.* May 2007. p. 37-39.

24. Massardier, V., et al., *Comparison of the evaluation of the carbon content in solid solution in extra-mild steels by thermoelectric power and by internal friction.* Scripta Materialia, 2004. **50**(12): p. 1435-1439.
25. Elsen, P. and H.P. Hougardy, *On the mechanism of bake-hardening.* Steel Research, 1993. **64**(8/9): p. 431.
26. Fekete, J.R., D.C. Strugala, and Z. Yao, *Advanced Sheet Steels for Automotive Applications.* Journal of Materials, 1992. **Jan 1992**: p. 17-21.
27. Butler, J.F., *Inhomogenous Deformation and its relationship to strain markings on annealed and temper-rolled sheets.* Flat Rolled Products III.
28. *The Volatile Organic compounds in paints, varnishes and vehicle refinishing products regulations 2005*, in *2005 No. 2773*. 2005, Environmental Protection Agency.
29. Wilson, D.V. and B. Russell, *The Contribution of Precipitation to Strain Aging in Low carbon Steels.* Acta Metallurgica, 1960. **8**(July): p. 468-479.
30. Wilson, D.V. and B. Russell, *The Contribution of Atmosphere Locking to the Strain-Aging.* Acta Metallurgica, 1960. **8**(Jan): p. 36-45.
31. Snoek, J.L., *Effect of Small Quantities of Carbon and Nitrogen on teh Elastic and Plastic Properties of Iron.* Physica, 1941. **7**: p. 711-733.
32. Wilson, D.V. and B. Russell, *Stress Induced Ordering and Strain-Ageing in Low Carbon Steels.* Acta Metallurgica, 1959. **7**(Sept): p. 629-631.
33. Nakada, Y. and A.S. Keh, *Kinetics of Snoek Ordering and Cottrell Atmosphere Formation in Fe-N Single Crystals.* Acta Metallurgica, 1967. **15**(May): p. 879-883.
34. Cottrell, A.H. and B.A. Bilby, *Dislocation Theory of Yielding and Strain Aging of Iron.* Proc. Phys. Soc, 1949. **62**(a): p. 49-62.
35. Baker, L.J., S.R. Daniel, and J.D. Parker, *Metallurgy and processing of ultralow carbon bake hardening steels.* Materials Science and Technology, 2002. **18**(4): p. 355-368.
36. De, A.K., S. Vandeputte, and B.C. De Cooman, *Kinetics of low temperature precipitation in a ULC-bake hardening steel.* Scripta Materialia, 2001. **44**(4): p. 695-700.
37. Sherman, A.M., G.T. Eldis, and M. Cohen, *The Aging and Tempering of Iron-Nickel-Carbon Martensites.* Metallurgical Transactions A, 1983. **14A**: p. 995-1005.
38. Harper, S., Physical Review, 1951. **83**: p. 709.
39. Bullough, R. and R.C. Newman, *The Flow of Impurites to an Edge Dislocation.* Proc. R. Soc., 1959. **A249**: p. 427-440.
40. Zhao, J.Z., A.K. De, and B.C. De Cooman, *Kinetics of Cottrell atmosphere formation during strain aging of ultra-low carbon steels.* Materials Letters, 2000. **44**(6): p. 374-378.
41. Berbenni, S., et al., *A micromechanical approach to model the bake hardening effect for low carbon steels.* Scripta Materialia, 2004. **51**(4): p. 303-308.
42. Cahn, J.W., *Nucleation On Dislocations.* Acta Metallurgica, 1957. **5**: p. 160-172.
43. Christian, J.W., *Theory of thermally activated growth*, in *The Theory of Transformations in Metals and Alloys*, G.V. Raynor, Editor. 1965, Pergamon Press: Oxford. p. 433-470.
44. Dollins, C.C., *Nucleation on Dislocations.* Acta Metallurgica, 1970. **18**: p. 1209-1215.
45. Barnett, D.M., *On Nucleation of Coherent Precipitates Near Edge Dislocations.* Scripta Metallurgica, 1971. **5**: p. 261-266.
46. Xiao, S.Q. and H. P, *A Model for the Nucleation of a Spherical Coherent Precipitate Near an Edge Dislocation.* Scripta Metallurgica, 1989. **23**: p. 365-370.
47. Zener, C.J., Journal of Applied Physics, 1949. **20**: p. 950.

48. Love, G.R., *Dislocation Pipe Diffusion.* Acta Metallurgica, 1964. **12**(June 1964): p. 731-737.
49. Miller, K.M., K.W. Ingle, and A.G. Crocker, *A Computer Simualtion Study of Pipe Diffusion in Body Centered Cubic MEtals.* Acta Metallurgica, 1981. **29**: p. 1599-1606.
50. Kozeschnik, E. and B. Buchmayr, *A contribution to the increase in yield strength during the bake hardening process.* Steel Research, 1997. **68**(5): p. 224-230.
51. Zhao, J.Z., A.K. De, and B.C. De Cooman, *A model for the Cottrell atmosphere formation during aging of ultra low carbon bake hardening steels.* Isij International, 2000. **40**(7): p. 725-730.
52. Raabe, D., *Computational Materials Science.* 1998, Weinheim: Whiley VCH.
53. Metropolis, N., et al., *Equation of State Calculations by Fast Computing Machines.* The Journal of Chemical Physics, 1953. **21**(6): p. 1087-1092.
54. Kang, H.C. and W.H. Weinburg, *Dynmaic Monte Carlo with a Proper energy Barrier: Surface Diffusion and two-Dimensional Ordering.* J. Chem. Phys., 1989. **90**(5): p. 2824-2830.
55. Cao, P.L., *Computer Experiments for Surface Diffusion: The Real Time in Monte Carlo Simulation.* Physical Review Letters, 1994. **73**(19): p. 2595.
56. Jaraiz, M., et al., *Kinetic Monte Carlo simulations: An accurate bridge between ab initio calculations and standard process experimental data.* Materials Science in Semiconductor Processing, 2000. **3**(1): p. 59-63.
57. Soenen, B., et al., *Competition between grain boundary segregation and Cottrell atmosphere formation during static strain aging in ultra low carbon bake hardening steels.* Acta Materialia, 2004. **52**(12): p. 3483-3492.
58. Hu, S.Y. and L.Q. Chen, *Solute segregation and coherent nucleation and growth near a dislocation-a phase-field model integrating defect and phase microstructures.* Acta Materialia, 2001. **49**(3): p. 463-472.
59. Tither, G., et al. *Precipitation Behavior and Solute Effects in Interstitial-Free Steels.* in *Physical metallurgy of IF steels.* 1994. Tokyo: Tokyo.
60. Hua, M., C.I. Garcia, and A.J. DeArdo. *New Understanding of Stabilization and the Properties of Ultra-Low Carbon Steels.* in *Steel sheet and steel bar products and processing for automotive applications.* 1998. Detroit; MI: Sae.
61. Hua, M., C.I. Garcia, and A.J. DeArdo, *Precipitation Behavior in Ultra-Low-Carbon Steels Containing Titanium and Niobium.* Metallurgical and Materials Transactions A, 1997. **28**(9): p. 1769-1780.
62. Mendoza, R., et al., *Structure of a low carbon Al-killed/Ti-added steel.* Isij International, 1997. **37**(2): p. 176-180.
63. Hubert, R.A., G. Dupuis, and R. Taillard. in *International Forum for the Properties and Applications of IF Steels.* 2000. Warrendale: PA.
64. Gupta, I. and D. Bhattachrya. *Metallurgy of Formable Vacuum Degassed Interstitial-Free Steels.* in *International Symposium on Metallurgy of Vacuum-Degassed Steel Products.* 1990. Indianapolis Indiana: TMS.
65. Tanioku T, H.Y., Okamato A, Mizu N. 1991, Society of Automotive Engineers.
66. Lips, K., et al., *The effect of coiling temperature and continuous annealing on the properties of bake hardenable IF steel.* Steel Research, 1996. **67**(9): p. 357-363.
67. Hook, R.E., A.J. Heckler, and J.A. Elias, *Texture in Deep Drawn Columbium (Nb) Treated Interstitial-Free Steels.* Metallurgical Transactions A, 1975. **6A**: p. 1683-1692.
68. Ooi, S.W. and F. G, *A comparitive study of precipitation efffects in ti only and Ti V Ultra Low Carbon (ULC) strip steels.* Materials Characterization, 2006. **56**: p. 214-226.

69. Girina, O. and D. Bhattacharya, *Effect of Vanadium on Mechanical Properties and Bake Hardenability in ULC Steels.* Mechanical Working and Steel Processing Conference Proceedings, 1999(37): p. 435-444.
70. Baker, L.T., J.D. Parker, and S.R. Daniel, *Mechanism of bake hardening in ultralow carbon steel containing niobium and titanium additions.* Materials Science and Technology, 2002. **18**(5): p. 541-547.
71. Gladman, T. and P.S. Mitchell, *Vanadium in Interstitial Free Steels.*
72. De, A.K., et al. *Effect of dislocation density on the low temperature aging behavior of an ultra low carbon bake hardening steel.* in *Internal friction and ultrasonic attenuation in solids*. 1999. Buenos Aires: Elsevier.
73. De, A.K., S. Vandeputte, and B.C. De Cooman, *Static strain aging behavior of ultra low carbon bake hardening steel.* Scripta Materialia, 1999. **41**(8): p. 831-837.
74. Rubianes, J. and P. Zimmer, Revue De Metallurgie, 1996(January): p. 99-109.
75. Rubianes, J.M. and P. Zimmer. *Development of Bake-Hardenable Steels for Automotive Applications at Sollac.* in *High-Strength Steels for Automotive Symposium*. 1994.
76. Van Snick, A., et al. *Effect of carbon content, dislocation density and carbon mobility on bake hardening.* in *Modern LC and ULC Sheet Steels for forming: processing and properties*. 1998. Aachen.
77. Hanai, S., et al., *Effect of Grain Size and Solid Solution Strengthening Elements on the Bake Hardenability of Low Carbon Aluminium-killed Steel.* Transactions ISIJ, 1984. **24**: p. 17-23.
78. Yamazaki, K., et al. *Manufactuing Condition and Automotive Use of Bake Hardenable Steel Sheets.* in *Microalloyed HSLA Steels*. 1988.
79. Messien, P. and V. Leroy, *Scavenging Additions of Boron in Low C Low Al Steels.* Steel Research, 1989. **60**(7): p. 320-328.
80. Pradhan, R. *Dent Resistant Bake-Hardening Steels for Automotive Outer Body Applications.* in *International Conference on Steel in Motor Vehicle Manufacture.* 1990. Dusseldorf, Germany.
81. Obara, T., et al., *Effects of Heat Cyle and Carbon Content on the Mechanical Properties of Continuous-Annealed Low Carbon Steel Sheets.* Kawasaki Technical Report, 1985. **12**(July 1985): p. 25-35.
82. Hundy, B.B., *Accelerated Strain Ageing of Mild Steel.* Journal of The Iron and Steel Institute, 1954. **Sept 1954**: p. 34-38.
83. Baird, J.D., *Strain aging of steel - a critical review; part I: Practical Aspects.* Iron and Steel, 1963(May): p. 186-192.
84. *Operational Procedure for the Iwatani-Rhesca Hot Dip Simulator*, CSPUK.
85. bsi-global, *BSEN 10002.*
86. Baker, L.J., *Operational Procedure for use of the VIBRAN torsional pendulum*, Corus RD&T: Port Talbot.
87. bsi-global, *BSEN 10002*, bsi-global.
88. *American Society for Testing and Material; ASTM E112-96(2004)e2 Standard Test Methods for Determining Average Grain Size.* 2004.
89. (developed at the University of Texas Health Science Center at San Antonio, T.a.a.f.t.I.b.a.F.f.f.m.u.e., *UTHSCSA ImageTool program.*
90. James, W., *Principles of Electron Optics*, in *Electron Microscopy and Microanalysis of Crystalline Materials*, J.A. Belk, Editor. 1979, Applied Science Publishers ltd: London.

91. Lorimer, G.W., *Precipitation Studies*, in *Electron Microscopy and Microanalysis of Crystalline Materials*, J.A. Belk, Editor. 1979, Applied Science Publisher Ltd.: London. p. 29-55.
92. Baker, L.J., in *Materials Research Centre, School of Engineering*, University of Wales Swansea: Swansea.
93. Mitchell, P.S. and T. Gladman, *Vanadium in Interstitial Free Steels.* Mechanical Working and Steel Processing Conference Proceedings, 1997: p. 37-48.
94. Ooi, S.W. and F. G. in *Materials Science and Technology 2004.* 2004. New Orleans, Louisiana.
95. De, A.K., et al., Journal of Allloys and Compounds, 2000. **310**: p. 405-410.
96. Avrami, M., Journal of Chemical Physics, 1939. **7**: p. 1103-1112.
97. Johnson, W.A. and R.F. Mehl, Trans. AIME, 1939. **135**: p. 416-458.
98. Matsuda, H. and H.K.D.H. Bhadeshia, *Avrami theory for transformations from non-uniform austenite grain structure.* Materials Science and Technology, 2003. **19**: p. 1330-1335.
99. Bradley, D.M., *Verhulst's Logistic Curve.* College Mathematics Journal, 2000(Dec 2000): p. 94-98.
100. Fourlaris, G., *Verbal communication - Instruction on preperation of TEM samples.* 2007.
101. Okamoto, A., K. Takeuchi, and M. Takagi, *A Mechanism of paint Bake-Hardening.* The Sumitomo Search, 1989. **39**: p. 183-194.
102. Tanikawa, K., Y. Hosoya, and T. Koike, *Strain Aging Properties of Extra-Low Carbon Bake Hardenable Cold Rolled Steel Sheets.* NKK Technical Review, 1995(72): p. 10-19.
103. Davies, D., *ECM2, Heol Cefn Gwrgan, Port Talbot.* 2007.
104. Choi, J.Y., et al., *Precipitation and recrystallisation behaviour in extra low carbon steel.* Isij International, 2002. **42**: p. 889-893.
105. Bortz, A.B., M.H. Kalos, and J.L. Lebowitz, Journal of Computational Physics, 1975. **17**: p. 10.
106. Amiot, B. and J. Despujols, *Strains in extra-low-carbon steel sheets after weak (skin-pass) rolling.* Metals Technology, 1983. **10**: p. 161-166.
107. Taylor, K.A. and J.G. Speer. in *39th MWSP conf. Proc.* 1998.
108. Gater, A.J. and S.G. Brown, *An analysis of kinetic Monte Carlo simulation as a tool for modelling strain ageing.* Scripta Materialia, 2005. **53**(6): p. 625-630.